Lab-on-a Chip platforms for manipulation and sensing of biological entities

A dissertation submitted by

Kyoungchul Park

In partial fulfillment of the requirements

for the degree of

Doctor of Philosophy

in

Electrical Engineering

TUFTS UNIVERSITY

August, 2015

Advisor:

Dr. Sameer Sonkusale

Abstract

The advent and continuous scaling of micro-fabrication technology has offered new capabilities in realization of Lab-on-a-Chip (LoC) platforms. More specifically, they offer the potential to perform spatial control and manipulation of biological targets with embedded transducers to sense and process them. If such platforms can be integrated transistors and readout circuitry, it has the potential to offer truly miniaturized solution. From a standpoint of LoC platform design, we present two platforms for biosensing and manipulation of cells.

First, I present a CMOS LoC platform for DEP trapping and repositioning of cells and microorganisms. Given the need to perform the operation in real-time, in-situ impedance monitoring of the trapping function is demonstrated. We present EM simulation results for DEP force and reorientation by novel three-dimensional (3D) octapole electrode geometry, all realized in a commercial 0.5μm CMOS process. This CMOS LoC platform integrates an analog front end for impedance monitoring of biological targets as they are repositioned on electrodes due to DEP in real-time. Experimental results with yeast cells validate the design.

Second, I present a compact AC susceptometer for biosensing based on Brownian relaxation of magnetic nanoparticle (MNP). A novel multiplexed sensing scheme based on the measurement of the magnetic susceptibility of the affinity captured target molecules on magnetic nanoparticles in liquid suspension is proposed. The AC magnetic susceptibility provides a measurement of Brownian relaxation behavior of biomolecules bound to MNPs that is related to its hydrodynamic size. The miniaturized AC susceptometer exhibits high sensitivity in magnetic fields as low as 10 μT for 1 mg ml−1 concentration and 5 μl volume, and is fully software programmable. The capability of biological sensing using the proposed scheme has been demonstrated in proof of principle using the binding

of biotinylated horseradish peroxidase (HRP) to streptavidin-coated MNPs. The technique and instrument are readily compatible with lab-on-chip applications for point-of-care medical applications.

Acknowledgements

First of all, I would like to express my sincerest gratitude to my advisor, Professor. Sameer Sonkusale, who gave me the opportunity to work in exciting projects in his Nanoscale Integrated Sensors and Circuits Laboratory at Tufts University and provided me an exceptional research environment. His vision, guidance, and support made me to pursue a multidisciplinary research without losing my focus. He always encouraged me to try new ideas and motivated me to keep my research work and complete my Ph.D program.

Many thanks to the members of the thesis committee, Prof. Anil Saigal from Mechanical engineering at Tufts University, Prof. Usman Khan from Electrical Engineering at Tufts University, and Dr. Youngho Suh from MIT Lincoln Lab, for evaluating the thesis and providing valuable comments and feedback.

I am particularly grateful to Dr. Shideh Kabiri who provided me a lot of support and help to prepare test samples and experimental set-up for research work on dielectrophoresis.

Dr. Samuel MacNaughton, my fellow researcher, provided a great deal of technical aid for different research works of low power FDSOI amplifier and dielectrophoresis.

I would like to express my sincere appreciation to Prof. Eddie Goldberg from Biomedical Engineering at Tufts University and Prof. Robert Guertin from Physics department at Tufts University, who supported my AC magnetic susceptometer project with valuable advice and financial support. I wish May their souls rest in perfect peace.

Also, I am thankful to Dr. Tim Harrah from Biomedical Engineering at Tufts University for his valuable support on AC magnetic susceptometer research work.

I am especially grateful to Dr. Sungkil Hwang, my sincere friend, for all the fruitful and creative discussions we had regarding circuit design and encouragement to finish my thesis.

Ptotr Olejarz from Analog Devices Inc., was a great co-worker to me for low power FDSOI amplifier work.

I would also like to thank to all the colleagues in Nano lab, especially Dr. Jian Guo, Dr. Wangren Xu, Saroj Rout, Krenar Komoni, Dr. Pooria Mostafalu, Zhenying Luo and Dr. Michael Trakimas for sharing their visionary ideas and all the fun in Tufts.

I should give special thanks to my Korean friends, Dr. Byungju Jung and Dr. Kanghyun Ji who provided me moral support during my PhD. I will always miss the social gathering and the joyful conversations with them. I also wish to extend my thanks to Namho Kang, Jungha Gil, Kookhee Han, Hyunjung Lee, Suchan Moon, Eunsoo Lim and Wonjae Kim for encouraging me to graduate.

I owe particular thanks to fellow employees at Qorvo Inc., Steve Richards, Carl Schaffer, Scott Monro, Hien Bui and Ginny Lacquio not only for their valuable support but also for their encouragement for 5 years.

I would like to thank my mother, Sukhee Cho and my sisters, Jiyoung, Hye-young, who have always supported my studies with limitless patience, encouragement and love.

First and foremost, I am truly thankful to my wife, my best friend, Seounghee Byun for her patience, support, and love. Thanks for walking alongside with me in this long and difficult path. Also, I would like to express an enormous amount of love to my son, Hyungkyu and my daughter, Hye-won.

Table of Contents

List of Tables

List of Figures

Chapter 1

Introduction

With an augmenting need for low cost point-of-care diagnostic devices, Lab-on-a-chip (LoC) systems have been introduced as a promising candidate from point of view that they enable development of low cost, miniaturized analytical devices that integrate microfluidics, electronics and various sensors [1,2]. Such systems offer great potential for biotechnology applications such as genome research, drug discovery, point-of-care (PoC) diagnostics, cell manipulation and sensing [3,4,5,6,7].

LoC devices promise numerous advantages for design and implementation of biomedical devices such as: (i) much lower consumption of reagents and sample;

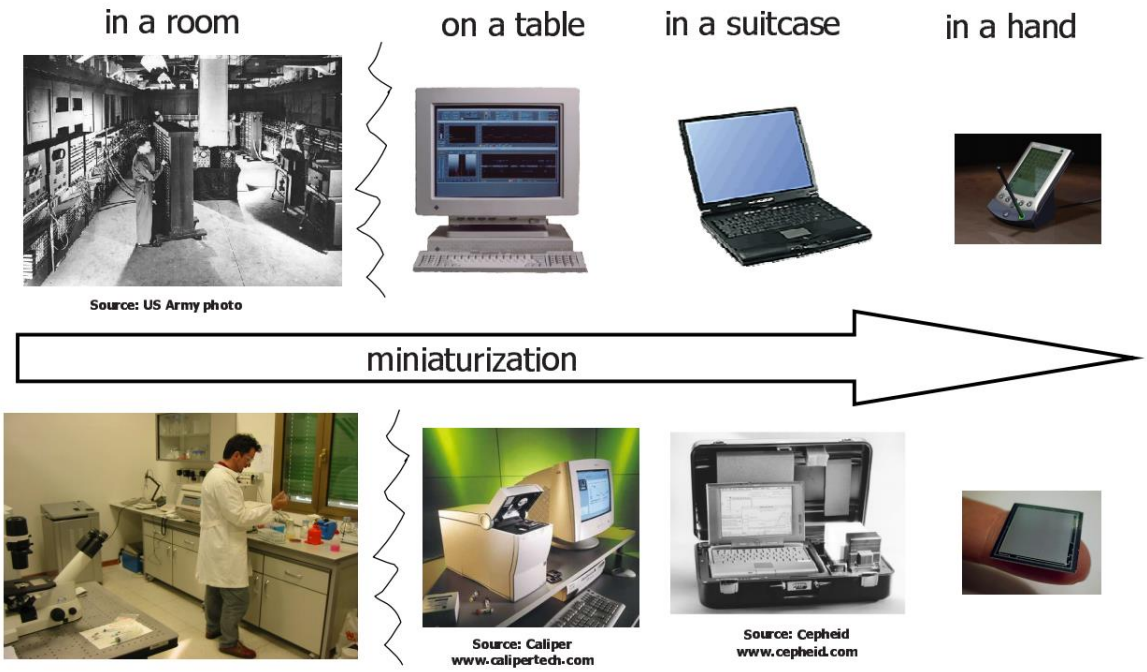

Figure 1.1. Lab-on-a-chip development shown parallel with computer systems evolution

(ii) faster response due to fast liquid handling by microfluidic channels, short diffusion times, and high surface-to-volume ratio; (iii) lower power consumption and lower weight; (iv) high throughput analysis thanks to parallelism; and (iv) lower fabrication cost through batch fabrication [8]. In particular, since conventional devices in bioclinical applications consist of fluidic systems and bulky detectors, miniaturization using LoC technology is of essential importance to implement portable and compact devices as well as to adapt the characteristic dimensions of the devices to the cells, microorganisms and nanoparticles. Furthermore, integration of LoC devices with the semiconductor fabrication technology gives capability to build not only the microfluidic systems but also the

integrated transducers and readout circuitry in same platform, which offers promising solutions to realize autonomous and multi-functional systems [9,10].

With significant improvement in the semiconductor technology, advanced micromachining technology named Micro-Electro-Mechanical Systems (MEMS)

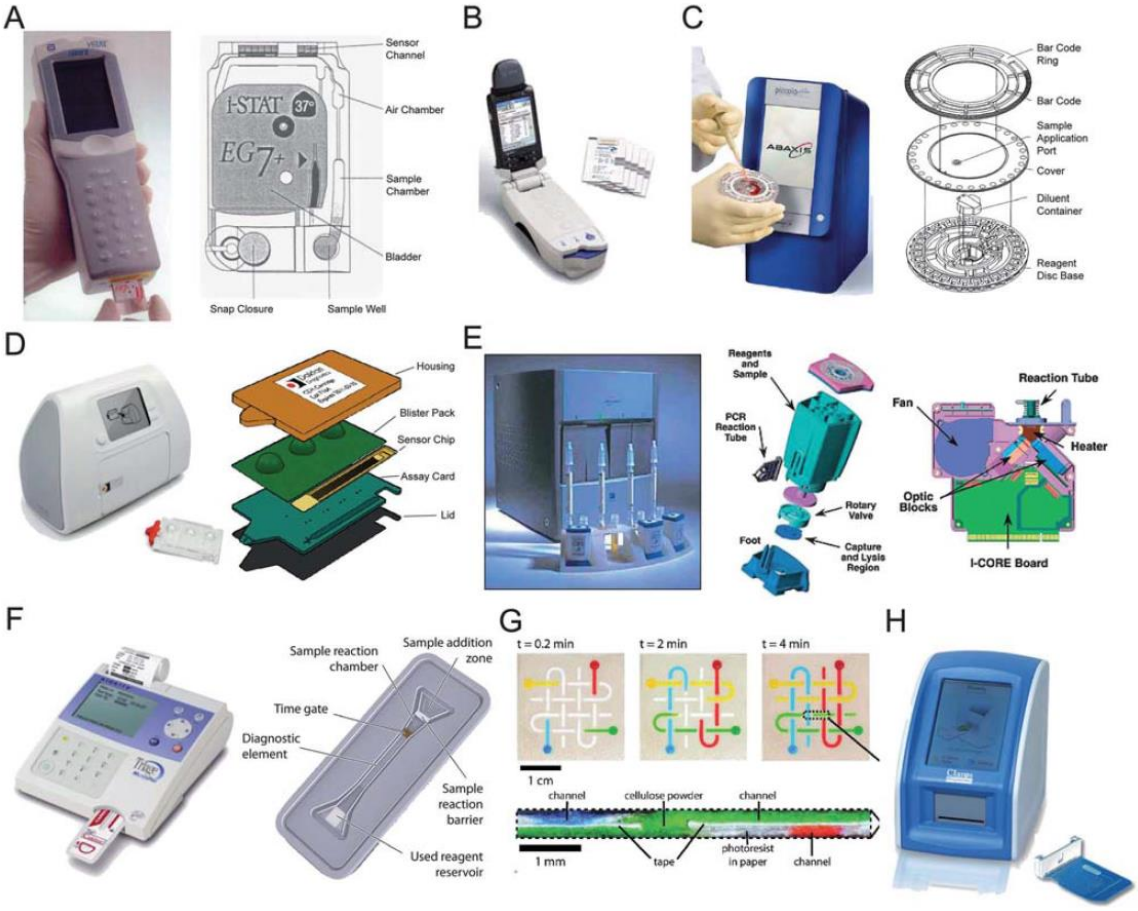

Figure 1.2 Images and schematics of various LoC-based Point-of-care devices: (A) i-STAT (Abbott): blood analysis system (B) Epocal: blood analysis, From www.epocal.com (C) Abaxis: analysis of blood, serum or plasma, From www.abaxis.com (D) Dakari Diagnostics: HIV staging and monitoring, From www.daktaridx.com (E) Cepheid: single module on-demand molecular diagnostic system, From Sensors Magazine. (F) Biosite: comprehensive testing platform for cardiovascular, renal, toxicology, and women's health assays, From www.alere.com (G) 3D microfluidic devices in layered paper and tape. [11] (H) Claros Diagnostics: immunoassay solution for blood. From www.clarosdx.com

has emerged. The standard MEMS fabrication process made it possible for the integration of micromechanics with microelectronics [12]. Moreover, it enabled to develop effective lab-on-a-chip systems for chemical and biological analysis with the addition of new materials and techniques [13]. However, it turned out that MEMS based biosensing devices have a couple of prominent limitations. One is the technical challenges of manufacturing embedded transducers using custom surface and bulk MEMS procedures [14], and the other is complexity and cost justification of heterogeneous integration of all components including microfluidic channels, detectors and readout circuits. It will be more cost effective if commercial complementary metal–oxide semiconductor (CMOS) technology can be employed without any process modifications for implementation of sensors and actuators in biomedical and biotechnological applications. CMOS process is superior to custom MEMS processes for matters of unmatched yield, integration capabilities and cost-efficiency [15,16,17]. CMOS based devices are, however, not always suitable for biological interfaces due to the issues of biocompatibility for materials in the process and its stability in electrolyte solution [18,19]. However, design flexibility and system-level integration of CMOS process offer unique advantages for many biological applications requiring highly parallel measurements. Hence, the interface design called 'post-CMOS processing' is necessary to prepare a CMOS based device for bio-assays to facilitate biocompatibility in manipulating/sensing biomolecular targets. Many post-processing techniques for interface design have been studied and developed [20,21,22].

A lot of research on CMOS based LoC systems have been carried out for biological sensing and manipulation, focusing on how to integrate a specific type of transducer into CMOS chip. LoC devices based on CMOS can be classified by identifying types of transducer structure. First, electrochemical transducers are considered as most compatible transducer structure with CMOS processes [23]. Electrochemical transducers consist of two components, set of electrodes and an electrolyte, where electrons are charge carriers in electrodes and ions are charge carriers in electrolyte, respectively. These transducers generally extract information from the electrical characteristics of the electrode-electrolyte systems, which are represented by potential, current, impedance, *I*–*V* curves and so on. The major challenge to implement CMOS electrochemical biosensors is that the aluminum electrodes in top metal layer is not very bio-compatible to potential electrolytes as gold, platinum, titanium, or silver. This problem can be overcome by covering more robust and versatile electrodes on top of the aluminum electrodes to avoid direct exposure of electrolyte to the electrode. For some electroanalytical systems (e.g., electrophoresis), low operating voltage of CMOS process is a problematic because electroanalytical systems usually require hundreds to thousands of volts for proper operation but commercial CMOS processes can only handle at maximum tens of volts in today's technology and a more dedicated high voltage CMOS process may be needed.

Optical transducers are another popular application for CMOS process. Some studies on CMOS and CCD image sensors using Si photodiodes and Si photogates

showed progress of the silicon-based optical sensors [24,25,26]. Silicon (Si) is an appropriate material for high-performance visible-range (400~800nm wavelength range) detectors, so CMOS processes can be a good biosensing platform for optical transducers with their silicon substrate. Photons in the infrared (IR) and ultra violet (UV) range cannot be effectively detected using CMOS because Si is transparent in IR wavelengths while having a very small penetration depth in the UV range. Consequently, CMOS could be very applicable to optical biosensing devices for visible range photons. However, many of optical biosensor systems require optical excitation as well as fluorescent reporters, which have emission spectra in the visible range [24,27], but silicon is not a outstanding light source due to the characteristic of indirect bandgap. Also, CMOS based optical transducers do not have the wavelength selectivity required for fluorescence spectroscopy, in particular, the stringent requirement of the excitation blocking filter [24,28] and external optical components such as filters may be needed as shown in Figure 1.3 [29,30,31].

It is known that magnetic biosensing schemes are better suited than the bulky and expensive optical systems based on imaging or fluorescence. Magnetic biosensors have several advantages such as simplicity of sample preparation, ease of processing and inherent biocompatibility with the use of micro/nano sized magnetic particles as detectable labels. Since most magnetic biosensors require external bias to generate sufficient magnetic field strength (e.g. standalone magnets, high Q coils) and complicated post-processing, limiting their form factor

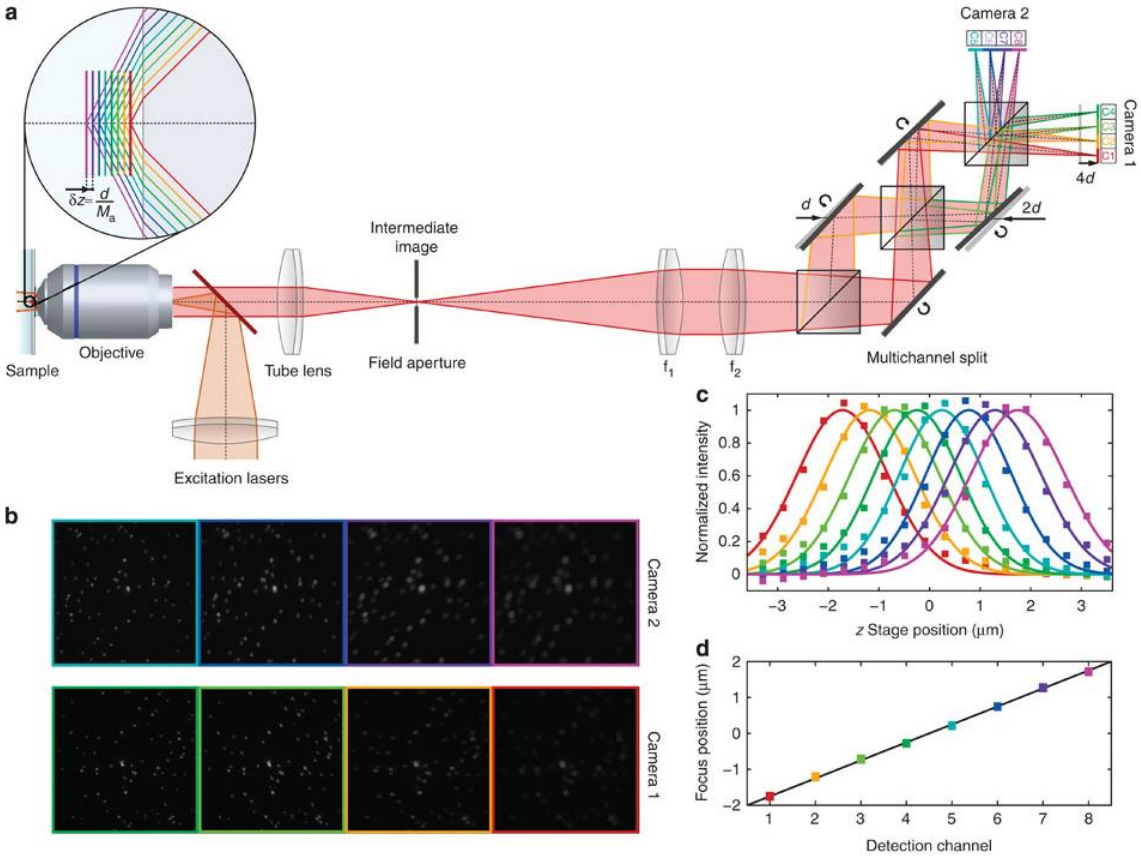

Figure 1.3 Multiplane widefield fluorescence sensing (a) Test-set-up of fluorescence microscope (b) Image frames taken with a fluorescent bead sample. (c) Peak brightness in the image frames in b upon scanning the sample plane through the focal channels. (d) Calibration of the focal plane separation by the positions of the brightness maxima in c. [29]

and cost, it is not straightforward to fully integrate whole system of magnetic biosensor into single chip [32,33]. It is for this reason many magnetic biosensing devices are fabricated in hybrid type of LoC system, where magnetic field sources are externally connected to internal readout and control electronics. Some kind of Hall-effect sensors can be implemented in silicon substrates of CMOS to detect both dc and time-varying magnetic fields [34]. Also, low Q spiral inductors can be

integrated in standard CMOS to create and detect time-varying magnetic fields. We will discuss more details of various magnetic biosensing scheme in chapter 4.

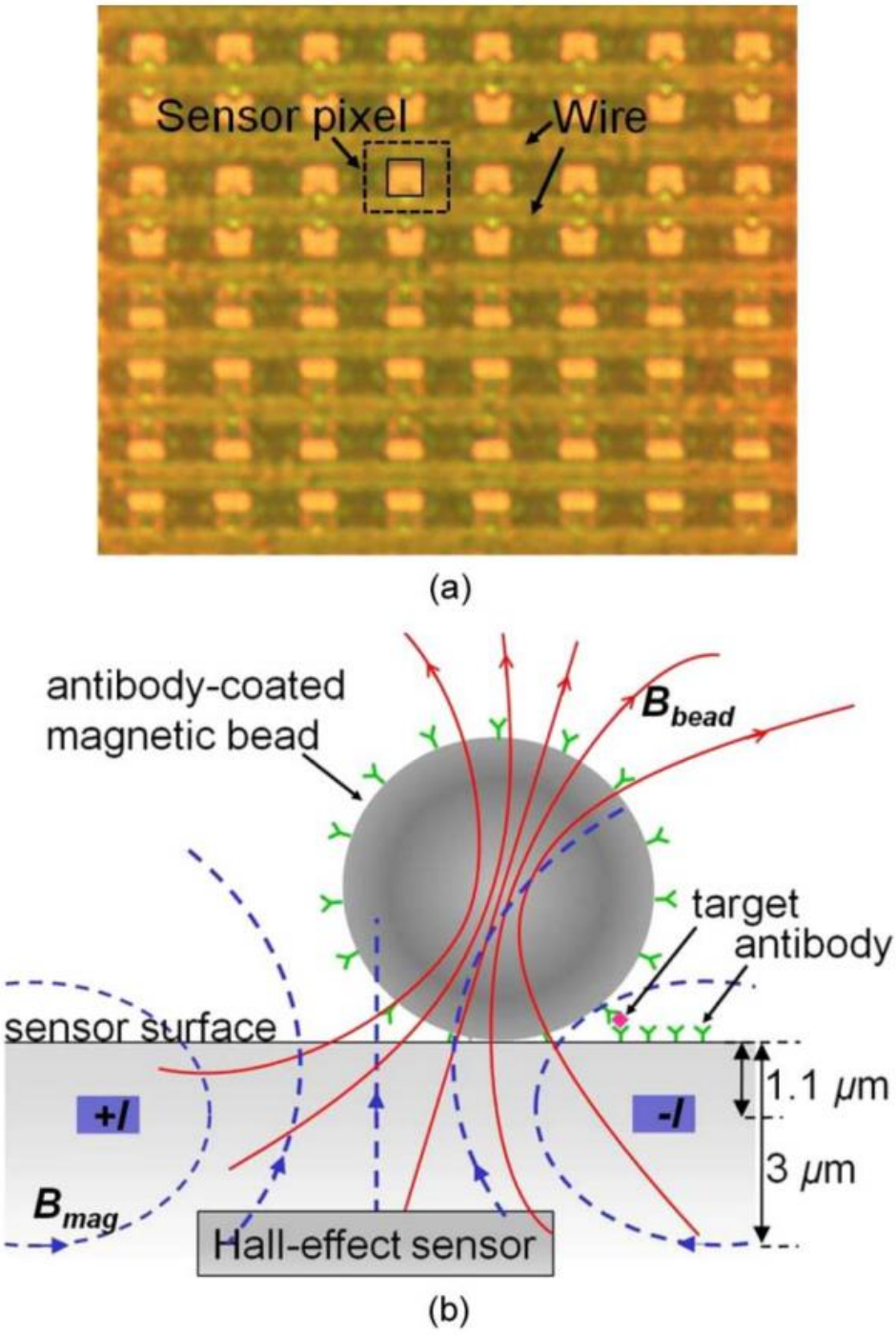

Figure 1.4 (a) 8X8 array of CMOS Hall-effect sensors. Each sensor pixel consists of a Hall plate and two access transistors. (b) Magnetic immunoassays. [34]

Other physical sensors as temperature sensors are also available in CMOS processes. Most of these active and passive devices have temperature-dependence characteristics which can be exploited to measure temperature [35,36].

The dissertation will focus on two different methods based on LoC platform for biological manipulation and sensing. One is a CMOS LoC platform for cell manipulation and monitoring using dielectrophoresis (DEP). The application for such platform ranges from cell detection to cell sorting for eventual processing of cells such as electroporation or lysis. The other LoC system is an AC susceptometer based on Brownian relaxation of magnetic nanoparticle. In chapter 2, the fundamentals and various methods of cell manipulation is presented. The principle and details of dielectrophoretic cell trapping and electro-rotation is following in the chapter 3. Chapter 4 describes proposed dielectrophoretic Lab-on-Chip Platform fabricated on CMOS, where yeast cell used to verify cell trapping and detection ability of the DEP system. Theory and classification of magnetic particle based biosensing are introduced at chapter 5. In chapter 6, AC susceptometer based on Brownian relaxation for biosensing is presented. Finally conclusion and future direction is addressed in chapter 7.

Chapter 2

Cell manipulation in Lab-on-a-Chip

2.1. Background of cell manipulation

Before the advent of microfluidic and lab-on-a-chip technologies in the 1980s [37], several techniques for manipulation of biological entities at the microscale had been invented and developed. In the early 1900s, ultraviolet microscope and phase-contrast microscope were developed and commercialized to observe transparent biological particles. During the following several decades, the rapid development of microscopy techniques brought forth new approaches

to observe and analyze cellular and intracellular interactions. For visualizing and localizing antigens in cells and tissues, a fluorescent antibody technique using the Stoke shift, which represents a fluorescence difference between excitation and emission spectra, was developed by Albert Coons in the mid-1900s, who became a leader in the field of immunofluorescence by firstly labeling antibodies with fluorescein isothiocyanate (FITC) [38,39]. The technique utilizes a fluorescence microscope and allows visualization of the distribution or amount of target molecules within cells.

From the mid-1900s, scientists and engineers started to have strong interest in techniques to manipulate biological particles, not just in observation of stationary microscopic particles. Arthur Ashkin at Bell Labs in 1970, for the first time, proposed a concept of an optical trapping technique, which has ability to manipulate micrometer-sized particles at the single particles level [40]. Afterward, he continued to develop advanced technique which can stably captured microscopic particles in three dimensions by using a tightly focused laser beam and also demonstrated the optical manipulation technique allowing viruses and bacteria successfully trapped in aqueous solution [41]. On the other hand, a photo-electric device to count continuously flowing cells was reported by Andrew Moldovan in 1934 [42]. This technique has a significance for the first description of a flow cytometry, which is a laser-based, biophysical technology to enable cell counting, sorting and biomarker detection by suspending cells in a stream of fluid and passing them by an electronic detection apparatus. Then, a concept of

hydrodynamic focusing for focusing cells into a single-file flow was introduced by Crossland-Taylor in the mid-1950s [43]. This technique has made it possible to accurately manipulate and delivery cells suspended in a fluid within narrow capillaries. This hydrodynamic manipulation technique was, consequentially, a beginning of 'fluorescence activated cell sorter (FACS)', which was invented by Leonard A Herzenberg in 1976 [44]. Electrical based cell manipulation techniques also come into the spotlight recently. Dielectrophoresis (DEP), an electrical force induced by a non-uniform electric field, was first described and defined by Herbert A Pohl in 1951 [45]. Nowadays, usefulness of DEP has been highlighted due to its potential in the selective spatial manipulation of viruses, bacteria, cells and sub-micron biological particles [46,47,48]. We will discuss more details of DEP based cell manipulation technique in chapter 3.

The emergence of microfluidics in late 1980s provided lots of opportunities for cell biology by combining cell manipulation techniques with microfluidics, which can deal with flow behavior and precise control of fluid that is geometrically constrained to a sub-millimeter scale. The early microfluidics techniques have been used in the field of molecular analysis, bio-defense, molecular biology and microelectronics, but not cell biology [37]. With improvement of cell manipulation technology, microfluidics was able to offer new tools and capabilities for cell biologists. The combination of cell manipulation techniques and microfluidic technology, nowadays, plays a critical role in various applications in cell biology, clinical research and biomedical engineering due to the ability to precisely control

the cellular environment, to easily make heterogeneous cellular environment with multiplexing assay, and to analyze cellular information at the single-cell level. Various cell manipulation techniques based off different forces, including optical, magnetic, electrical and mechanical force, have been developed for applications in specific objectives, such as cell focusing, trapping, sorting and separating target cells from heterogeneous cell solution (Figure 2.1). Table 1 summarizes the latest achievements of cell manipulation techniques. In the next section, details regarding various techniques of cell manipulation will follow on.

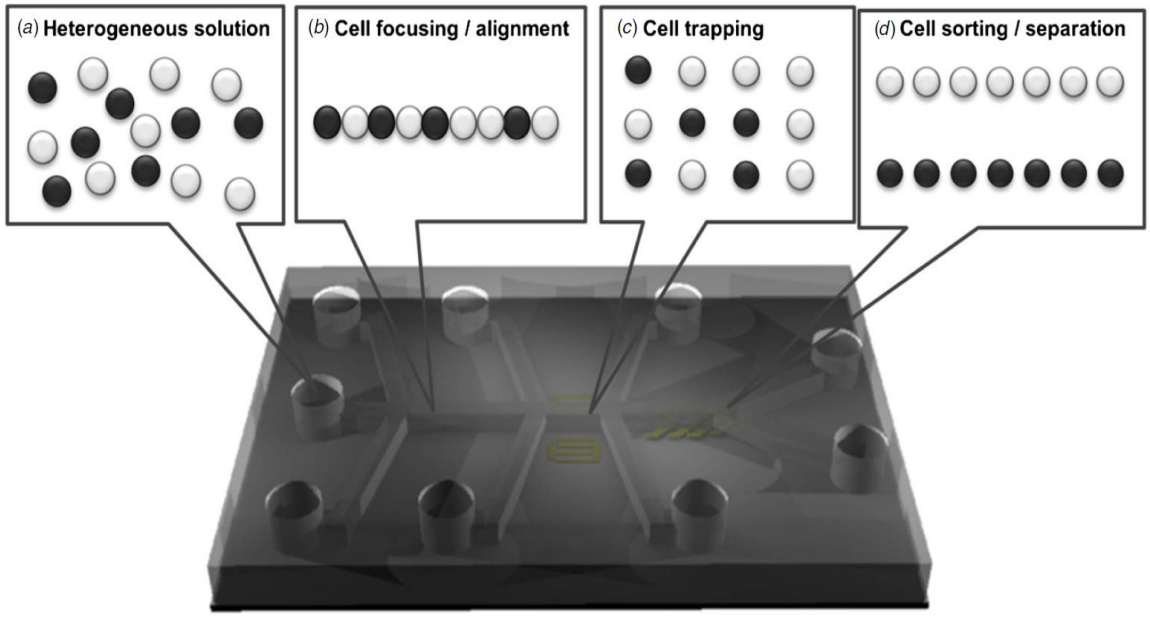

Figure 2.1. Schematics of various applications of cell manipulation techniques in microfluidics. In order to focus, align, trap and separate target cells from heterogeneous cell solution, various cell manipulation techniques, including optical, magnetic, electrical, mechanical and combination manipulation techniques, have been developed. [49]

Table 1. Latest achievements of cell manipulation techniques [49]

Manipulation types	Applications (purposes)	Methods	Mechanisms (principles)	Throughput	Single cell capability	Targets	Discriminating parameters
Optical	Cell sorting	Optical fractionation	Optical lattice induced lateral fractionation	High	Difficult	Microscopic particles	Particle size and refractive index
	Cell sorting	Optical switching	Target cells can be sorted by optical force switching based on their detected fluorescence	High	Easy	Mammalian cells	Fluorescence markers
	Cell sorting	Size and fluorescence dependent methods	Target cells can be moved precisely by optical tweezers	Low	Easy	Yeast cells and hESC	Cell size and fluorescence
	Cell sorting	Optical trapping	Utilizing properties of cells affecting their optical trapping force	Low	Easy	HeLa cells	Cell size and refractive index
	Cell separation	Optical scattering force	The scattering force push particles to be displaced own path	High	Difficult	Polystyrene microspheres	Particles size
	Cell trapping/ single cell analysis	Optical tweezers	Positioning target cells in the detection area	Low	Easy	Human blood	Cell size
	Cell trapping/ single cell analysis	Optical tweezers	Positioning in the measurement region by optical tweezers	Low	Easy	Yeast	Cell size and refractive index
	Cell trapping/ single cell analysis	Optical tweezers	Target excited fluorescence spectrum was detected by wavelength detector	High	Difficult	Pathogens	Fluorescence spectrum
	Diagnosis	Optical pressure	Measurement of deformability of cells under optical pressure	High	Difficult	Erythrocytes	Viscoelastic properties of cells
	Molecule injection	Microfluidic photoporation	Focused laser beam to create a sub-micron hole in the plasma membrane of a cell (photoporation)	Low	Difficult	Mammalian cells	None
	Electroporation	Optical tweezers	Positioning in a microchannel connected to a nanochannel	Low	Easy	Cancer cells (K562)	Cell size
Magnetic	Cell separation	Magnetophoretic separation	High gradient magnetic field	High	Difficult	Human blood	Native magnetic properties of cells
	Cell separation	Magnetophoretic separation	High gradient magnetic field	High	Difficult	Bacterial cells	Magnetic beads labeling of cells
	Cell capturing	Magnetophoretic isolation	Magnetic single cell micro array	High	Easy	Jurkat cells	Magnetic beads labeling of cells
	Cell separation	Magnetophoretic separation	Sorting of monocytes which internalize nanoparticles by high gradient magnetic field	High	Difficult	Human blood	Endocytotic activity
	Cell trapping / isolation	Magnetophoretic isolation	Cells attached magnetic beads magnetically collected within camber	High	Difficult	Rare cells	Magnetic beads labeling of cells
	Cell analysis	Self-assembled magnetic bead patterns	Immunospecific cell capture and the latter being used for cell adhesion and growth	High	Difficult	Cancer cells	Magnetic beads labeling of cells
Electric	Cell separation	Dielectrophoresis	Transverse flow by localized nonuniform electric field	Low	Difficult	Cancer cells	Electric properties
	Cell separation	Dielectrophoresis	Electrical conductivity gradient	High	Difficult	Yeast	Electric properties
	Cell separation	Dielectrophoresis	Marker-specific separation of rare target cells using DEP	High	Difficult	Bacteria	Cell surface marker
Electric	Cell separation	Dielectrophoresis	DEP force according to cells' size	High	Difficult	Human blood	Cell size
	Cell separation	Multi-orifice flow fractionation and Dielectrophoresis	Using hydrodynamic inertial forces by a multi-orifice structure and dielectrophoresis that the translational motion of charge neutral matter	High	Difficult	Rare cells	Size and electric properties
	Cell focusing	Dielectrophoresis	Using microfabricated flow cytometer combined with on-chip DEP manipulator	High	Difficult	Polystyrene microspheres	None
	Cell trapping/ isolation	Dielectrophoresis	By exploiting cell morphological characteristics	High	Difficult	Tumor cells	Electric properties
	Cell fusion	Dielectrophoresis	Cells can be trapped in electrofusion cage by DEP, and then fused and released sequentially	High	Difficult	Jurkat cells	None
Mechanical	Cell separation	Hydrophoretic filtration	Microstructure-induced pressure field gradient	High	Difficult	Human blood	Size and deformability
	Cell separation	Hydrodynamics in inertial flows	Inertial lift forces in microfluidics	High	Difficult	Human blood	Cell size and deformability
	Cell focusing	Hydrodynamics in inertial flows	Inertial lift forces and in microfluidics	High	Difficult	Human blood	Cell size
	Cell trapping/ isolation	Microvortices separation	Laminar microvortices	Low	Difficult	Human blood	Cell size
	Diagnosis	Image analysis	Using mechanical properties of infected blood cells	Low	Difficult	Erythrocytes	Deformability
	Cell analysis	Micropipette aspiration	Deformation of pressure by aspiration	Low	Easy	Cancer cells	Deformability
Other	Cell separation	Standing surface acoustic waves (SSAW)	Axial acoustic forces repositioning cells closer to the wave pressure node	High	Difficult	Microspheres	Size, density and compressibility
	Cell separation	Surface affinity	Interaction of target cells (CTCs) with antibody-coated microposts	High	Difficult	Rare cells (CTCs)	Surface biomarkers
	Cell separation	Surface affinity	Specific binding to surface markers	High	Difficult	Human blood (HL-60)	Surface biomarkers
	Cell separation	Biomimetic	Hydrodynamic force/Fahraeus effect	High	Difficult	Human blood	Size, deformability
	Cell trapping/ isolation	Standing acoustic waves	Acoustic trapping by tolerance to flow fluctuations	High	Difficult	Human blood	Size, density and compressibility

2.2. Techniques of cell and particle manipulation

2.2.1 Optical manipulation

The optical techniques have attracted great attention of cell biologists due to capability of single cell manipulation in addition to optical monitoring, however they need bulky diffractive optical components and instruments, which make it difficult to implement a highly functional, compact system and integrate into LoC platform (Figure 2.2). However the approach offers high resolution. After optical trapping using the gradient force of focused laser beams has been introduced by Arthur Ashkin in 1970, this technique was soon used to trap and manipulate biological molecules and cells, such as viruses, bacteria and live mammalian cells in the mid-1980 [41,50], and became a standard tool in biophysics. Besides optical trapping technique, other manipulation techniques such as optical sorting and switching with proper microfluidic techniques have been reported (Figure 2.3) [51,52]. In general, the highly focused laser beam in the optical manipulation techniques can cause potential damages to the biological samples. Although the photo damage can be reduced by using light of certain wavelength ranges, the potential of the damages has been a matter of concern in the field of cell biology,

particularly *in vivo* cell studies [53]. Nevertheless, the technique has become a promising tool for single molecule or cell studies due to the ability to apply pico Newton-level forces; measure nanometer-level displacement; enable contactless manipulation [54,55].

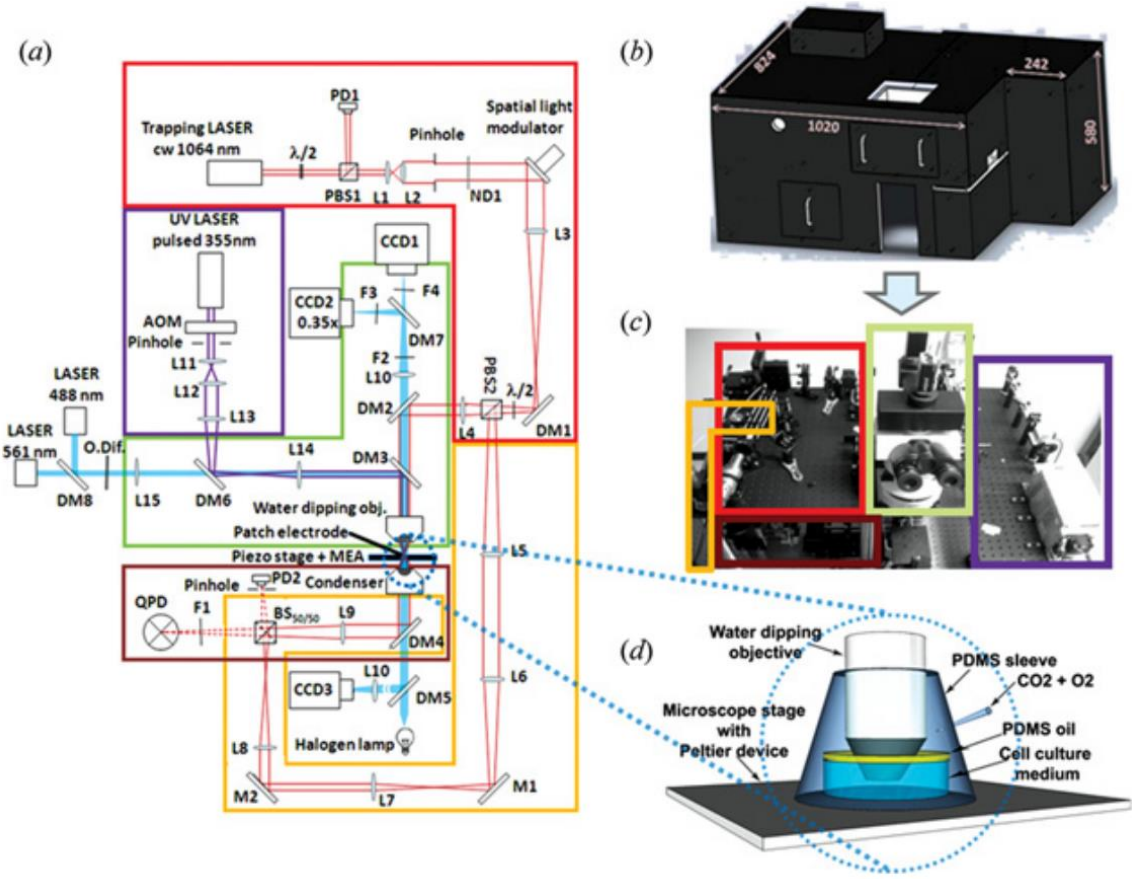

Figure 2.2 Example of physical test set-up for optical manipulation [56]

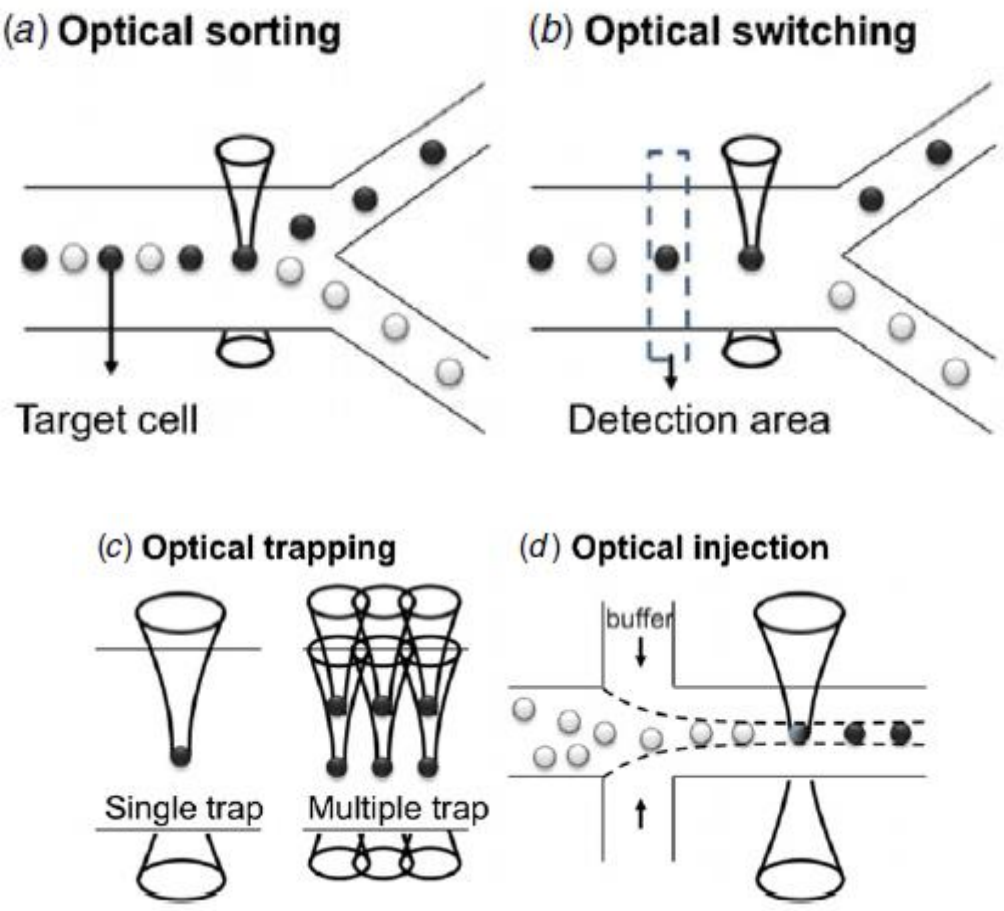

Figure 2.3 Illustrative schematics of various applications in cell manipulation techniques by using optical force. (*a*) Target cells in a microfluidic channel can be sorted based on physical properties of the cells affecting their optical trapping force, such as size, light absorption and refractive index. (*b*) The optical force was used as a switch to sort pre-determined target samples, while optical force in general can be directly used to recognize and sort simultaneously as shown in (*a*). (*c*) Both single trap and multiple traps can be made by optical trapping techniques. (*d*) Molecules in the surrounding fluid media can be delivered or injected into target cells by a focused femtosecond laser beam. [49]

We, here, explain briefly the principle of optical trapping of particles, which is valid when the size of the particles is much larger than the wavelength of the trapping laser. When the size of a particle is much larger than the wavelength of the trapping laser (usually $R > 10\lambda_0$, where R is the radius of the particle and λ_0 is the wavelength of the laser in vacuum), the optical forces on the particle can be calculated by ray optics model [57].

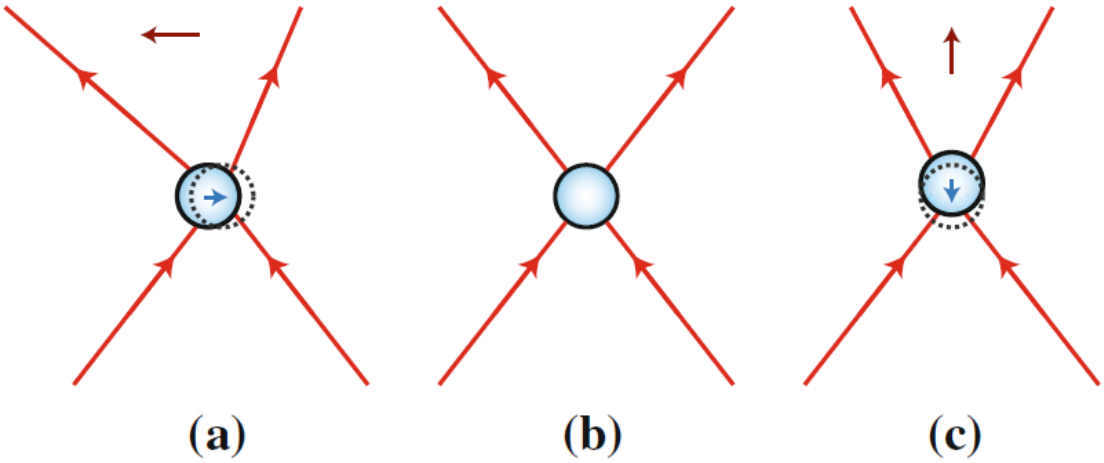

Figure 2.4 Qualitative view of optical trapping of dielectric particles. (a) Displays the force on the particle when the particle is displaced laterally from the focus. (b) Shows that there is no net force on the particle when the particle is trapped at the focus. (c) Displays the force on the particle when the particle is positioned above the focus.

A qualitative view of optical trapping of particles in the ray optics regime is shown in Figure 2.4 [58]. If we neglect surface reflection from the particle, then the particle will be trapped at the focus of the laser beam as shown in Figure 2.4(b). If the particle moves to the left of the focus like Figure 2.4(a), it will deflect the laser beam to the left and thus increase the momentum of photons to the left. The counter force from the deflected photons will push the particle to the right, i.e. back to the focus of the laser beam. If the particle moves along the propagation direction of the laser beam as shown in Figure 2.4(c), it will focus the laser more strongly and thus increase the momentum of photons along the propagation direction. The counter force from the deflected photons will push the particle back to the focus of the laser beam. The same thing will happen if the particle moves away from the focus in other directions. Thus a focused laser beam forms a stable optical trap in 3D. However, in reality, we need to consider the effect of the surface reflection mentioned before. The photons reflected back by the surface of a particle will push the particle forward. If this force is larger than the restoring force due to refraction, the particle will be pushed away from the focus, and thus cannot be trapped. The surface reflection depends on the relative refractive index of the particle and the medium $m = n_p/n_{md}$, where n_p is the refractive index of the microsphere and n_{md} is the refractive index of the medium. Larger m implies more surface reflection, and thus greater difficulty in trapping the particle with an optical tweezer [59]. It is, generally, more difficult to trap particles in air than in water because the refractive index of water (n_{water} =1.33) is greater than the

refractive index of air (n_{air} =1.00). To increase the restoring force for better trapping, the laser beam should be strongly focused by a high numerical aperture (NA) objective lens. Figure 2.5 and 2.6 are a typical schematic of test set-up and experimental results for optical tweezer array, respectively [60].

Optical techniques for cell manipulation are very robust and accurate for precise cell sorting and ease of single cell trapping, nevertheless there are inevitable limitations for low-cost and portable devices such as bulky instrumentation and need of external light source like laser.

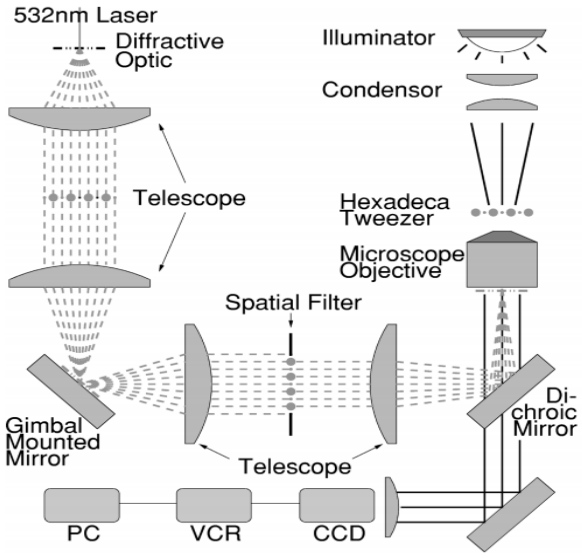

Figure 2.5. Schematic of a practical diffractively generated optical tweezer array

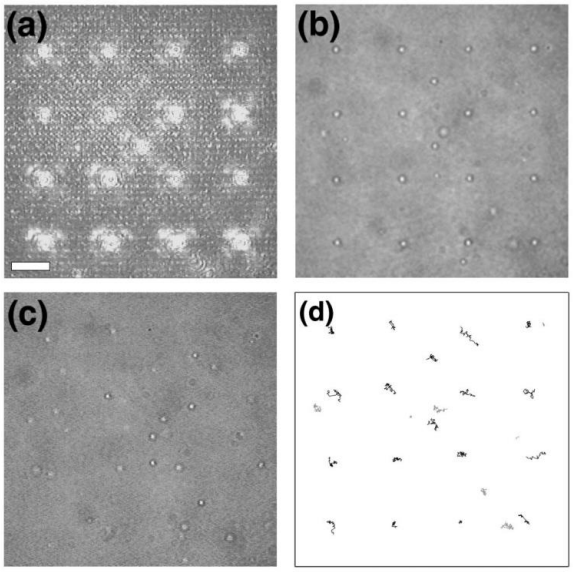

Figure 2.6. 4 X 4 Optical tweezer array created from a single laser beam using a holographic array generator.

2.2.2 Magnetic manipulation

An enormous surge of work using magnetic forces has been carried out in applications of biology for cell manipulation as well as biosensing based on molecular recognition. Even though some magnetic cell manipulation techniques utilize intrinsic magnetic properties of biological macromolecules such as iron-containing hemoglobin in erythrocytes [61], many researchers working on the field of biomagnetics have focused on magnetic particle (MP) of nano and micro-scale as a label of target biomolecule or cell, due to the relative simplicity of sample preparation, ease of processing and inherent biocompatibility [62,63]. Magnetic

particles can be used to selectively attach and manipulate or transport targeted species to a desired location under the influence of an external magnetic field. By virtue of their size, magnetic nanoparticles (MNPs) have a property of super paramagnetic, which offers great potential in a variety of applications in their bare form or through coating with a surface coating and functional group chosen for a specific biological application. We will discuss deeply about properties and bio-application of magnetic particles in chapter 5.

Magnetic manipulation techniques, generally, utilize magnetic fields and magnetic particles of various kinds and sizes. Typical magnetic particles have a magnetic core and a non-magnetic coating that can be tailored to bind to specific biological entities. Magnetite is one of the common materials for MPs, as it is hard to oxidize. The range of particle sizes is from 5 nm and up to a couple of μm. Particles that can be considered as a single magnetic domain will act as non-magnetic particles as soon as the magnetic field is removed. Larger particles will maintain a certain degree of magnetization after the field has been removed and there may, therefore, be difficulties in removing the particles from the trap and from the cluster formed during the trapping [64]. The magnetic force on a particle can be expressed as a function of the particle volume, the difference between the media and the particle in magnetic susceptibilities and the strength and gradient of the applied magnetic field [65]:

$$F = \frac{V \cdot \Delta\chi}{\mu_0} (B \cdot \nabla) B \qquad (2.1)$$

where V is the particle volume, $\Delta\chi$ is magnetic susceptibilities, B is magnetic flux density and ∇ is a gradient of the applied magnetic field.

In a homogeneous field, where the magnetic gradient is zero, there will be no force acting on a particle. Thus, all techniques used for magnetic manipulation of particles are required to create inhomogeneous magnetic fields in different ways. The magnetic force on a particle is typically between a few pico Newton (pN) to tens of pN.

The principle of magnetic tweezers, one of classic magnetic manipulation techniques, is similar to that of optical tweezers where a magnetic particle in an external magnetic field experiences a force proportional to the gradient of the square of the magnetic field. High forces can be achieved with relatively small magnetic field strengths, provided that a very steep field gradient can be generated. Owing to the steep gradient, however, the force falls off rapidly with displacement away from the magnet. Consequently, appreciable force can only be applied on a particle in close proximity to the magnet, and the force is not constant for small displacements of the magnetic particle in the vicinity of the magnet. Larger magnets provide a higher magnetic field strength and a shallower field gradient, resulting in forces that vary more slowly over a larger area. Figure 2.7 shows the concept of a typical magnetic tweezer with magnetic particle labeled by a single molecule of DNA.

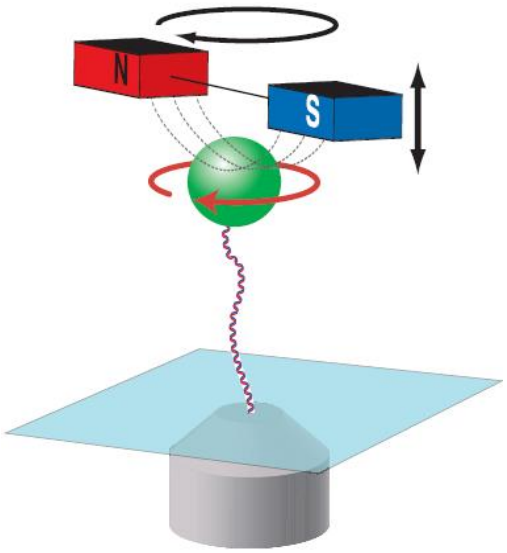

Figure 2.7**.** The layout of magnetic tweezers based on permanent magnets. A super-paramagnetic particle (green) is attached to the surface of the trapping chamber by a single molecule of DNA.

In general, permanent magnets have been used and are still very common as they can exert larger forces on particles than electromagnets [66]. As an example, a 5mm long permanent magnet can induce a magnetic force of 40 pN on a 500nm particles whereas an electromagnet would exert a hundred times lower force [67]. A system using electromagnets is, however, more flexible and there is also the possibility to use several magnetic poles, which can provide an ability to manipulate objects within the magnetic trap [68]. Another advantage of electromagnets is that an electromagnet's magnetic field can be rapidly manipulated over a wide range by controlling the amount of electric current

supplied to the electromagnet. Also, integration into LoC is much easier by fabricating micro-scale electromagnets.

Besides magnetic trapping, another magnetic manipulation techniques such as cell separation, sorting, and isolation, have been successfully developed and they offered new capabilities to biotechnology. The magnetic-activated cell sorting (MACS) technique [69] is one of the most commonly used techniques by using functional nanoparticles conjugated with antibodies corresponding to particular cell surface antigen. Using the magnetic separation technique, the target cells under the magnetic field can be separated positively or negatively with respect to the particular antigen. Cell capturing and isolation are another important application by magnetic cell manipulation techniques. Some studies verified that circulating tumor cells conjugated with MNPs can be captured and isolated using a microchannel integrated with permanent magnet [70,71]. The magnetic cell manipulation techniques can be potentially helpful for integrating on-chip sample preparation to microfluidic devices in a more systematic manner due to the ability to hold and release the cells easily.

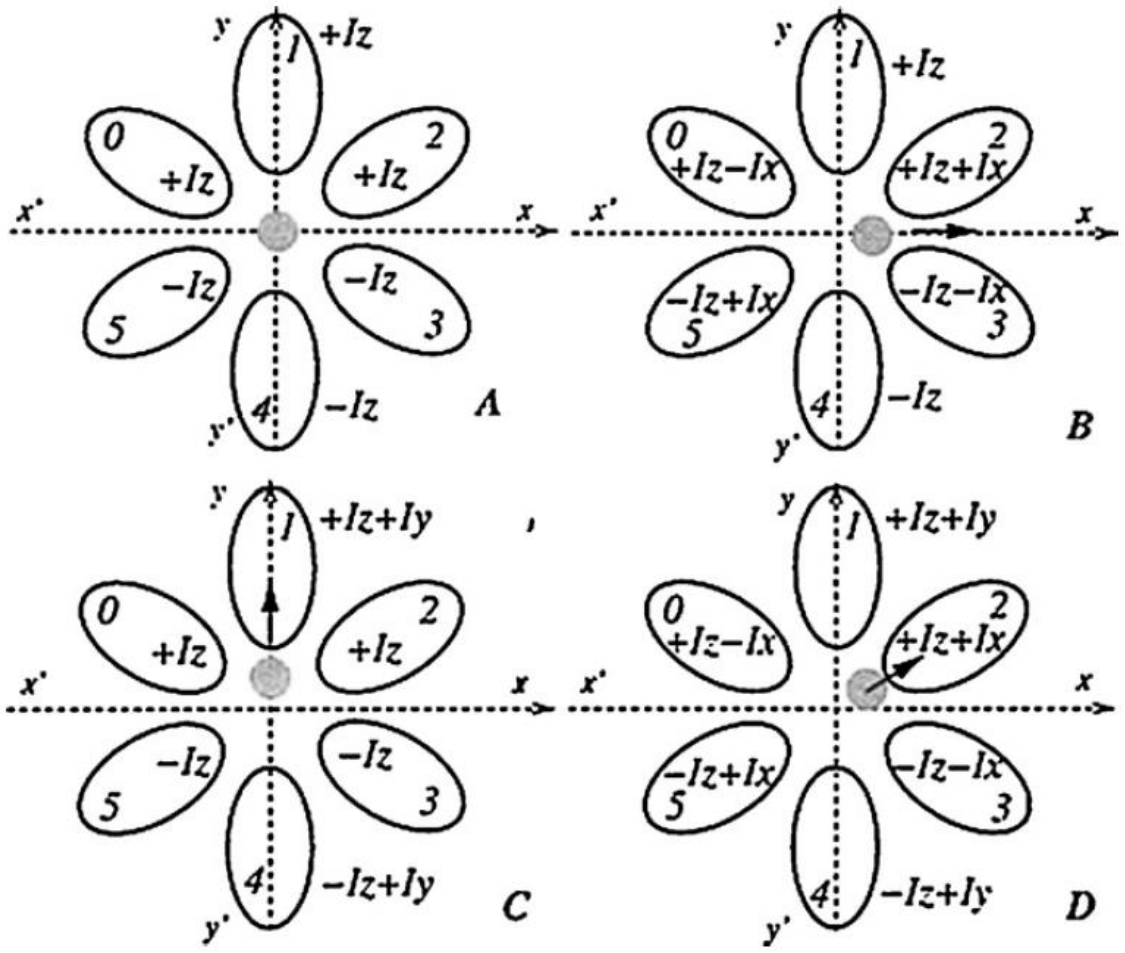

Figure 2.8. By computer controlling the driving current in the different coils used, a trapped particle can be manipulated in all dimensions. [68]

2.2.3 Electrical manipulation

Electric field-based manipulation techniques are particularly attractive for smaller bio particles and structures that require higher purity because of their high resolution and efficiency. Electrophoresis, which is the motion of dispersed

particles relative to a fluid under the influence of a spatially uniform electric field, is one method that enables the charge-based separation of suspended particles [72,73]. This electro-kinetic phenomenon was observed for the first time in 1807 by Ferdinand Frederic Reuss from Moscow State University, who noticed that the application of a constant electric field caused clay particles dispersed in water to migrate. It is ultimately caused by the presence of a charged interface between the particle surface and the surrounding fluid. Electrophoresis of positively charged particles (cations) is called cataphoresis, while electrophoresis of negatively charged particles (anions) is called anaphoresis. Electrophoresis is a size based separation technique and it is the basis for a number of analytical techniques used in biochemistry for separating molecules by size, charge, or binding affinity. This method has been used to separate and characterize a variety of biological and biomimetic structures including liposomes, bacteria, subcellular components and mammalian cells [72,74,75,76].

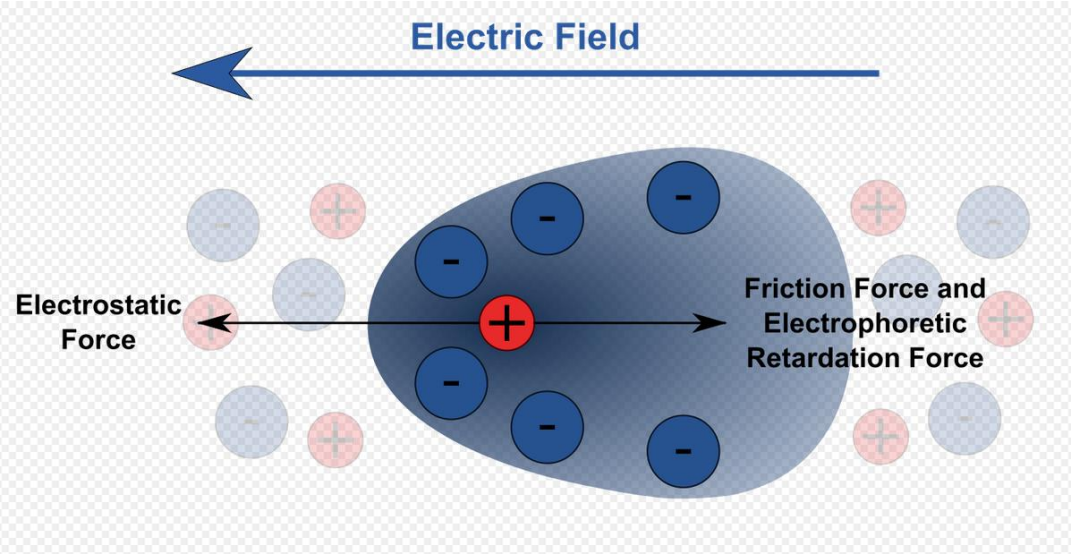

Figure 2.9 Mechanism of Electrophoretic migration

While electrophoresis depends primarily on the charge-to-size ratio of the particle, DEP depends on a rich set of both structural and chemical properties, which enables enhanced selectivity and sensitivity compared to electrophoresis. DEP exploits the force exerted by a non-uniform electric field on a polarizable particle. In general terms, dielectrophoretic force occurs as a result of the force exerted by the external field on the field-induced dipole moment of the polarized particle. The dipole moment induced in the particle can be represented by the generation of equal and opposite charges (+q and –q) at the particle boundary. The important fact is that this induced charge is not uniformly distributed over a particle surface, but creates a macroscopic dipole. If the applied field is non-uniform, the local electric field E and resulting force on each side of the particle will be different. Thus, depending on the relative polarizability of the particle with respect to the surrounding medium, it will be induced to move either towards the inner electrode and the high-electric-field region (positive DEP) or towards the outer electrode, where the field is weaker (negative DEP).

By the DEP approach, researchers have achieved impressive results including trapping, detecting and separating various biological samples [77,78,79]. More recently, some advanced researches presented multifunctional DEP based biochip using microfluidic technology as shown in Figure 2.10 [80]. More details about theory and applications of DEP will be discussed in chapter 3.

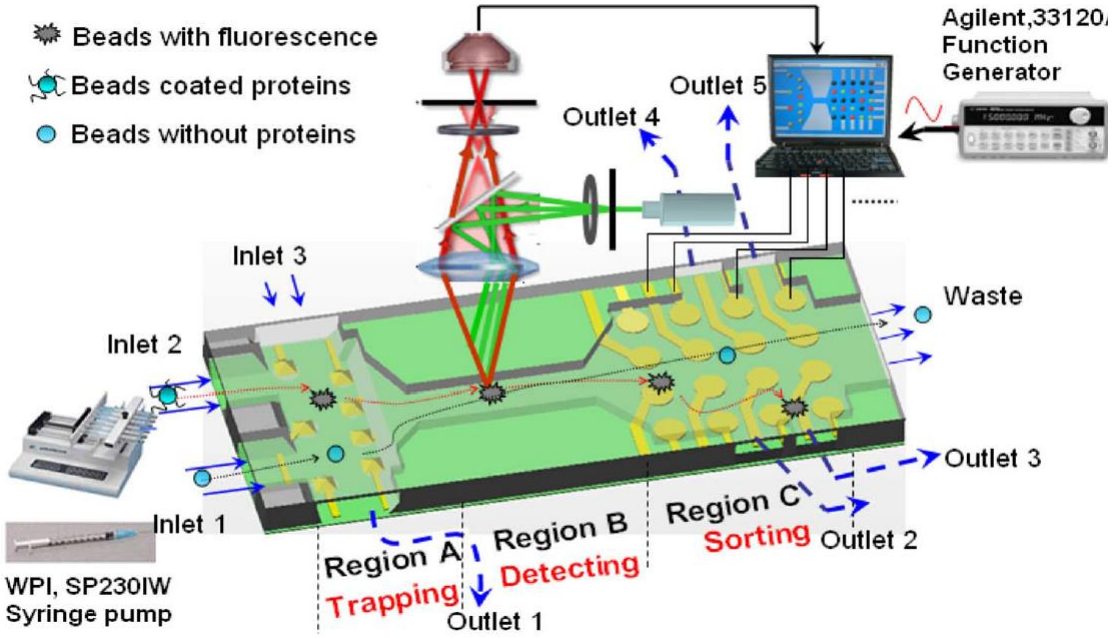

Figure 2.10. Illustration of our biochip for adaptive multi-sorting applications. Region A is the trapping and hybridization enhancement region with an array of micro-pyramid DEP traps. Mobile probe beads are injected from inlets 1 and 2 via external syringe pumps. Detected sample solution is injected from inlet 3. Region B is a fluorescent detection zone. The programmable DEP sorting array is located in region C to adaptively sort out mobile probes to different outlets (i.e.,2, 3, 4, and 5) based on the fluorescence detection signals fed back to a LabVIEW-implemented controller [80].

Chapter 3

Dielectrophoresis for cell manipulation and detection

3.1. Introduction

In the field of electrical manipulation of biological targets, dielectrophoretic force (DEP) based manipulation techniques are proven to be highly selective and versatile for smaller biological particles. As mentioned briefly in chapter 2, dielectrophoresis is the movement of a dielectric object due to forces generated by a non-uniform electric field, while electrophoresis relates to the movement of a charged particle in a uniform electric field [81]. Figure 3.1 illustrates the discrepancy between electrophoresis and dielectrophoresis. There is no dielectrophoretic net force in a uniform E-field as shown 3.1(b).

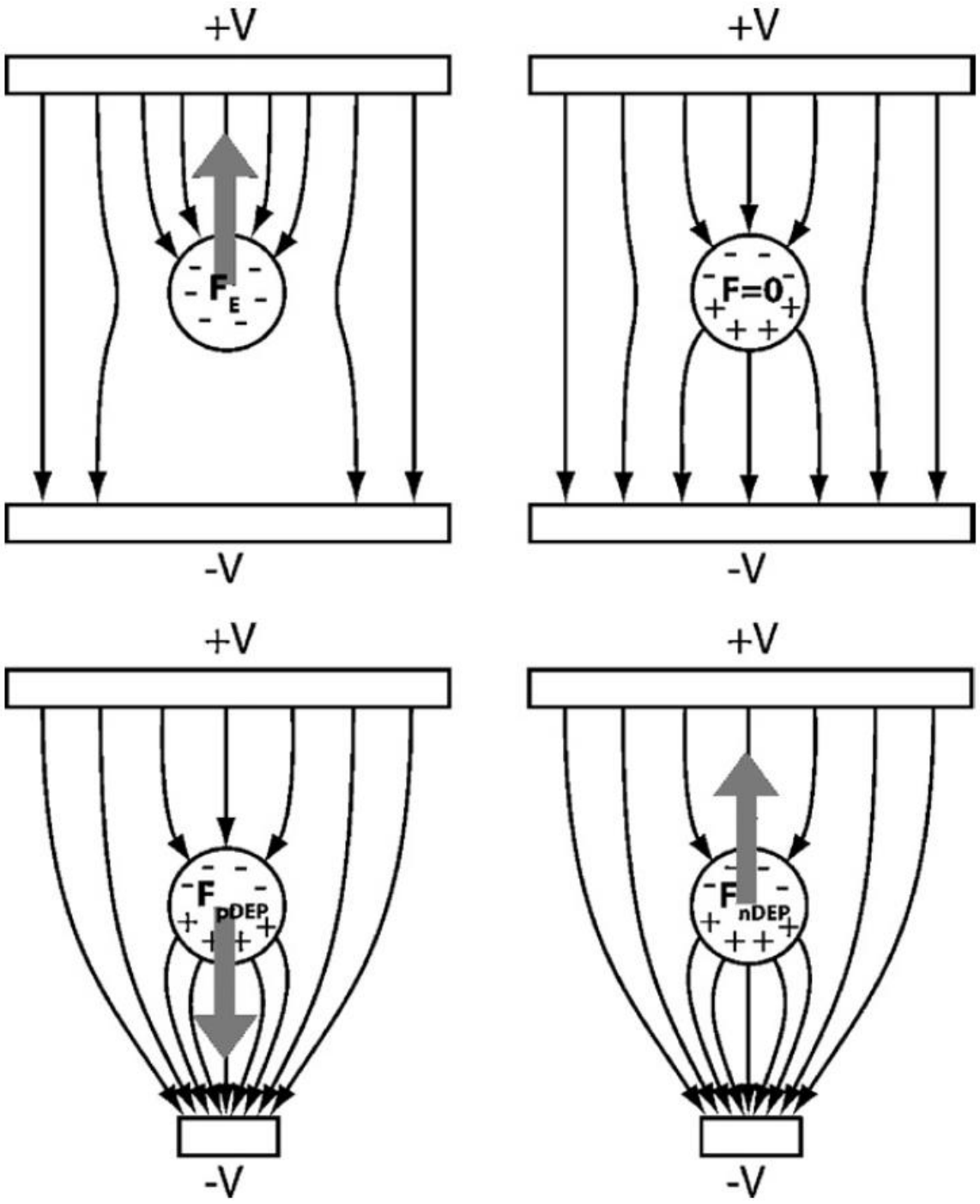

Figure 3.1 Electrophoresis (EP) and dielectrophoresis (DEP). (a) Electrophoretic movement of a charged object in a uniform electric field. (b)A dielectric object experiences no force in a uniform electric field. (c) p-DEP, the dielectrophoretic force moves the object towards the higher electric field. (d) n-DEP, the dielectrophoretic force moves the object towards the lower electric field. [81]

The direction of dielectrophoretic motion is determined by frequency dependent properties of the particle and the surrounding medium. The movement of particles on DEP can be manipulated either in the direction of higher electric field by a positive dielectrophoretic force (p-DEP), or in the direction of lower electric field by a negative dielectrophoretic force (n-DEP).

One of the most common applications of DEP is the cell separation. Cell-based microfluidic LoC applications using DEP have shown selective spatial separation of target cells, based on dielectric properties of the cells. DEP force acting on the cells, in general, is proportional to the size of cells. Thus, the displacement of cells that deviate from the streamlines depends on the cell size. By using this characterization of DEP in a microfluidic channel, heterogeneous biological molecules of a few to tens of micrometers difference in diameter can be continuously separated based on their size [82]. Also, the dielectric discrepancy of DEP response between viable (p-DEP) and nonviable (n-DEP) yeast cells enables viable and nonviable yeast cell mixture to be separated from each other with patterned electrodes in microfluidic device [83].

Another major application of DEP is the cell trapping. An example of simultaneous p-DEP and n-DEP trapping of viable and non-viable yeast cells is displayed in Figure 3.2 [84]. The shape of the polynomial electrodes was determined analytically to generate a well-defined non-uniform electric field in the trap. Due to the difference in the dielectric property, the viable cells experienced a p-DEP force collecting them at the electrode surface corners while

the non-viable cells were collected in the center of the trap as a result of the n-DEP force. The signal applied to adjacent electrodes is here 180◦ out of phase. Multi-polar electrode structures like polynomial electrodes can create a rotating electric field by applying multi-phase ac voltage into multiple electrodes, which is a potential of electro-rotation spectra [85]. In section 3.3, details of cell trapping and electro-rotation by DEP will be presented.

All the traditional DEP traps have on embedded electrodes to generate a high-frequency non-uniform electric field and this inherent configuration can cause undesirable electrochemical reactions and gas generation at the surfaces of these electrodes when running at low frequencies. Although the use of AC rather than DC voltage helps to minimize these effects, it does not perfectly eliminate them. In order to circumvent this drawback, the insulator-based dielectrophoresis (i-DEP) has been introduced by Cummings and Singh [86], where insulating posts are used to generate the non-uniform field in a microchannel connecting two reservoirs with external electrodes. The circular posts create both regions of high field strengths and regions of low field strengths, thus facilitating both p-DEP and n-DEP simultaneously.

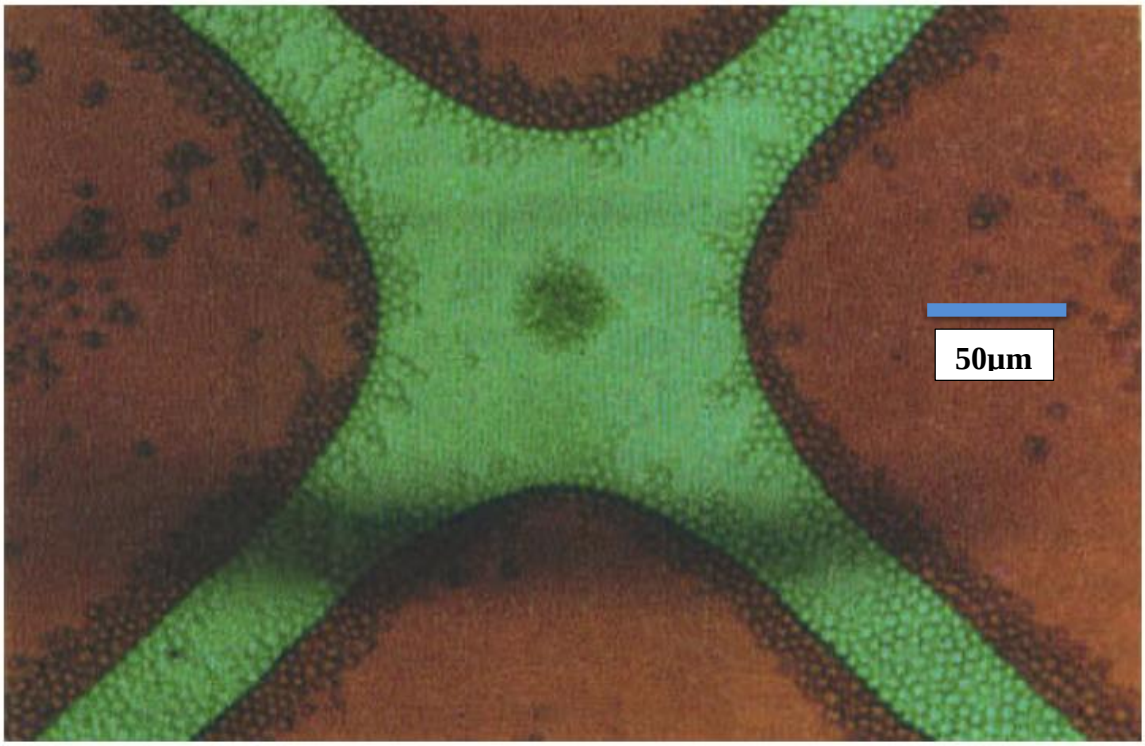

Figure 3.2 Polynomial electrodes for trapping yeast cells. Viable cells are trapped at the electrode surfaces by positive dielectrophoresis while non-viable are trapped in the center by negative dielectrophoresis. The trap was operated at 10 MHz, 5 Vrms. [84]

3.2. Derivation of dielectrophoretic force

In advance of the discussion regarding the dielectrophoretic force on dielectric particles, it is necessary to dig into the electromechanics of small particles under the influence of electroquasistatic fields and define a set of useful models in calculating electrical forces and torques on biological particles. The theory will be used to consider DEP manipulation such as trapping, electro-rotation and traveling-wave induced motion.

Effective moment method: The effective multipoles, including the dipole, the quadrupole, and other higher-order terms, facilitate a unified approach to electric-field-mediated force and torque calculations on particles. We, at first, get started with the effective dipole for simplifying a calculation of the force. Figure 3.3(a) depicts a small electric dipole of vector moment $\vec{p} = q\vec{d}$ located in a homogeneous, isotropic dielectric medium of permittivity ε_m, where $\vec{d}$ is the displacement vector pointing from the negative charge $-q$ to the positive charge $+q$. The dipole experiences a nonuniform, divergence free, electrostatic field $\vec{E}_0(\vec{r})$ imposed by electrodes (not shown in the figure 3.3). To define the effective moment, it is convenient to start with the electrostatic potential due to this electric dipole [87]:

$$\Phi = \frac{\vec{p}\cdot\vec{r}}{4\pi\varepsilon_m r^3} \tag{3.1}$$

where $\vec{r}$ is the radial vector distance measured from the center of the dipole and r is the absolute value of $\vec{r}$. If the dipole is small compared to the length of the imposed nonuniform field $\vec{E}_0$, then the force and torque may be approximated as follows [88]:

$$\vec{\mathrm{F}} \approx (\vec{p}\cdot\nabla)\vec{E}_0 \tag{3.2.a}$$

$$\vec{\mathrm{T}} \approx \vec{p}\times\vec{E}_0 \tag{3.2.a}$$

The dipole contribution to the total electric field cannot exert a force on itself and therefore is not included in $\vec{E}_0$.

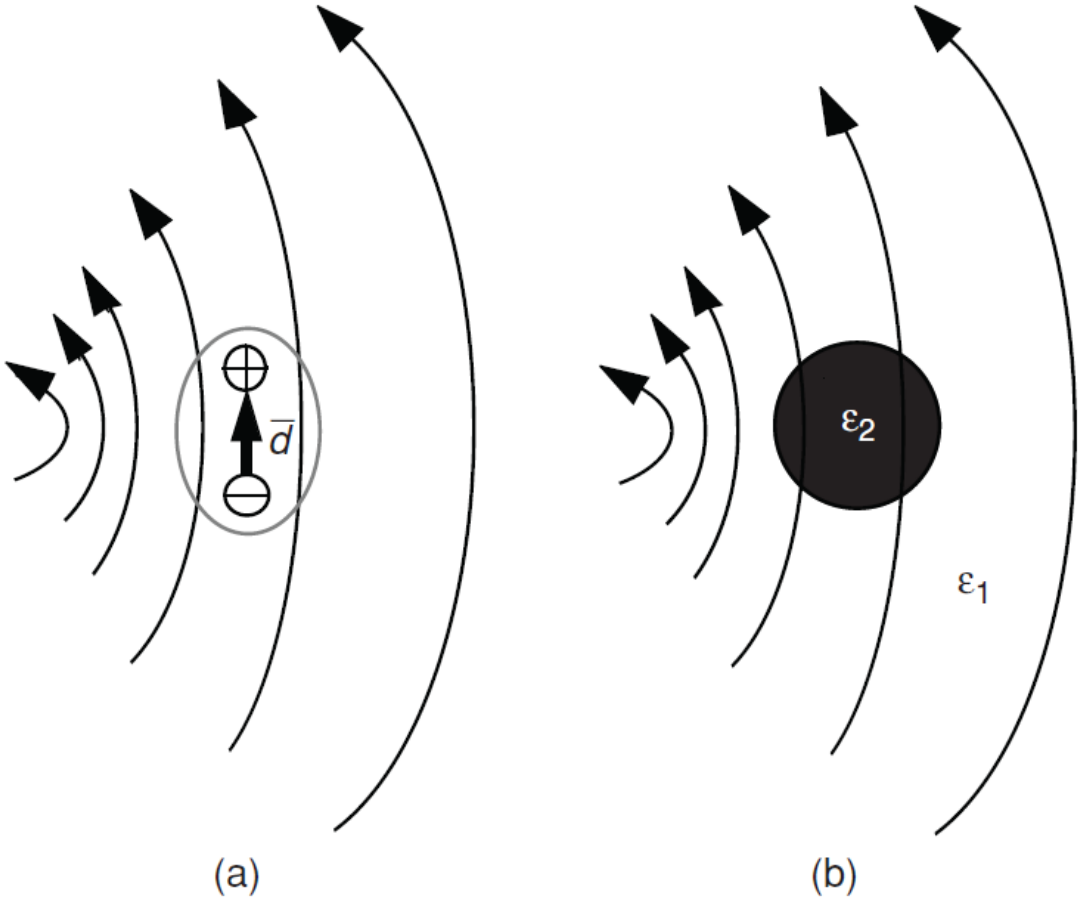

Figure 3.3 Definition of the effective dipole moment: (a) small physical dipole in nonuniform electric field; (b) dielectric particle in the same nonuniform electric field. Assuming that the physical scale of the nonuniformity of the imposed field is much larger than the particle radius *R*.

In order to adapt this derivation to a spherical bioparticle, let's replace the dipole by a small dielectric sphere of radius R and permittivity ε_p at the same position in the structure, as shown in Figure 3.3(b). The particle has the effect of perturbing the electric field and the induced perturbation is expressed in a form of an electrostatic potential as below:

$$\Phi_{induced} \approx \frac{(\varepsilon_p - \varepsilon_m) R^3 \vec{E}_0 \cdot \vec{r}}{(\varepsilon_p + 2\varepsilon_m) r^3} \tag{3.3}$$

where it has been assumed that the particle radius is small compared to the length scale of the imposed field nonuniformity. Equation (3.3) has the same form as (3.1) and the effective moment is defined by comparing these two expressions.

$$\vec{p}_{eff} \equiv 4\pi\varepsilon_1 K R^3 \vec{E}_0 \tag{3.4}$$

where $K = (\varepsilon_p - \varepsilon_m)/(\varepsilon_p + 2\varepsilon_m)$ is the Clausius-Mossotti factor [89]. Equation (3.4) defines the moment of the equivalent, free-charge, electric dipole that would create a perturbation field identical to and indistinguishable from that of the dielectric sphere for all conditions of $r > R$. The only distinction between this induced dipole and a general electric dipole is that, because we assumed the particle is a sphere and it is lossless, the moment will always be parallel to $\vec{E}_0$.

To evaluate the force on the dielectric particle we finally want to know, the effective moment of equation (3.4) is substituted directly into (3.2a). Combining (3.2a) and (3.4) gives the well-known expression for the DEP force on a dielectric sphere in a dielectric medium [90]:

$$\vec{\mathrm{F}} \equiv 2\pi\varepsilon_1 R^3 K(\nabla E_0^2) \qquad (3.5)$$

According to (3.5), a particle will be either attracted to or repelled from a region of strong electric field intensity, depending on whether $K > 0$, which is $\varepsilon_p > \varepsilon_m$ or $K < 0$, which is $\varepsilon_p < \varepsilon_m$, respectively.

Combining (3.2b) and (3.4) gives zero for the torque, because the dipole moment and electric field are always parallel by the assumption that the particle is spherical and lossless. However, nonspherical shapes are more common forms of bioparticles than spheres. For instance, mammalian erythrocytes (red blood cells), which are the most important cells in biomedical science, are essentially oblate spheroids with one side indented. Most recently, an analytic study has been published to get higher order terms of DEP force for nonspherical particles by replacing the simplified dipole approximation [91], where the results show that higher-order DEP forces are indeed of substantially increased significance for nonspherical particles, multipolar terms are seen to constitute more than 40% of the total force on ellipsoidal and cylindrical particles.

3.3 DEP based cell manipulation and detection

3.3.1 Effective forces in DEP trapping

The trapping and positioning of bioparticles have important applications in terms of cell injection, cell transfer, *in vitro* fertilization, cell interaction, stem cell research and immunoassays. Basically, cell trapping relies on the use of dielectrophoretic forces to hold and drag dielectric particles against a set of destabilizing forces, such fluid drag force or electro-thermal effect. As discussed earlier, the time averaged DEP force acting on a spherical dielectric particle in non-uniform electric field is :

$$\vec{\mathrm{F}} \equiv 2\pi\varepsilon_1 R^3 K(\nabla E_0^2) \tag{3.5}$$

The frequency dependence of DEP force is described by the Clausius-Mossotti factor (K) as shown in (3.6).

$$K = \frac{\varepsilon_p^* - \varepsilon_m^*}{\varepsilon_p^* + 2\varepsilon_m^*} \tag{3.6}$$

with complex permittivity given by

$$\varepsilon^* = \epsilon - j\frac{\sigma}{\omega} \tag{3.7}$$

The subscripts p and m refer to particle and medium respectively, σ is the conductivity and ω is the angular frequency of the applied electric field. Many important properties of DEP force lie within this simple relation. First, the

competition between the medium and particle polarizabilities will determine the sign of K factor, which will consequently determine the direction of the DEP force. Second, the real part of the K factor can only vary between +1 ($\varepsilon_p^* \gg \varepsilon_m^*$, which means the particle is much more polarizable than the medium) and -0.5 ($\varepsilon_p^* \ll \varepsilon_m^*$, the particle is much less polarizable than the medium). Thus n-DEP can only be half as strong as p-DEP. Third, by taking the appropriate limits, at low frequency, the K factor reduces to

$$\lim_{\omega \to 0} K = \frac{\sigma_p - \sigma_m}{\sigma_p + 2\sigma_m} \tag{3.8}$$

while, at high frequency, it is

$$\lim_{\omega \to \infty} K = \frac{\varepsilon_p - \varepsilon_m}{\varepsilon_p + 2\varepsilon_m} \tag{3.9}$$

Thus, similar to many electroquasistatic systems, the K factor will be dominated by relative permittivity at high frequency and conductivity at low frequencies. The induced dipole varies between a free charge dipole and a polarization dipole. Figure 3.4 shows changes of K factor in frequency domain as polarizations in a spherical particle and medium.

A particle suspended in moving liquid also experiences a drag force proportional to the difference in their velocity vectors. The hydrodynamic drag force on a spherical body with low Reynolds number in a uniform flow can be calculated using a standard form of Stokes' theorem:

$$F_{HD} = -6\pi a\eta V \qquad (3.10)$$

Where η is the fluid viscosity, a is the particle radius, and V is the particle velocity vector with respect to the fluid.

The spatially non-uniform temperature distribution created by the power dissipated by the electric field can lead to flows induced by electro-thermal effects. Since the medium permittivity and conductivity are functions of temperature, temperature gradients directly lead to gradients in permittivity and conductivity. These gradients in turn generate free charge which can be acted upon by an electric field to move and drag fluid along with it, creating fluid flow. This fluid flow creates a drag force on an immersed body just as it does for conventional Stokes' drag.

Another force on a particle is the gravity. The magnitude of the gravitational force is given by

$$\mathrm{F}_{gravity} = \frac{4}{3}\pi R^3(\rho_p - \rho_m)g \qquad (3.11)$$

where ρ_m and ρ_p refer to the densities of the medium and the particle, respectively, and g is the gravitational acceleration constant. Cells and beads are denser than the aqueous media and thus have a net downward force.

The fundamental requirement for any deterministic trap is that it creates a region where the net force on the particle is zero. In addition, the particle must be at a stable zero, in that the particle must have to do work to overcome the force

field in order to move out of that stable zero area. This is all codified in the requirement that $F_{NET} = 0$, $F_{NET} \cdot dr < 0$ at the trapping point, where F_{NET} is the net force and dr is an increment in any direction [92].

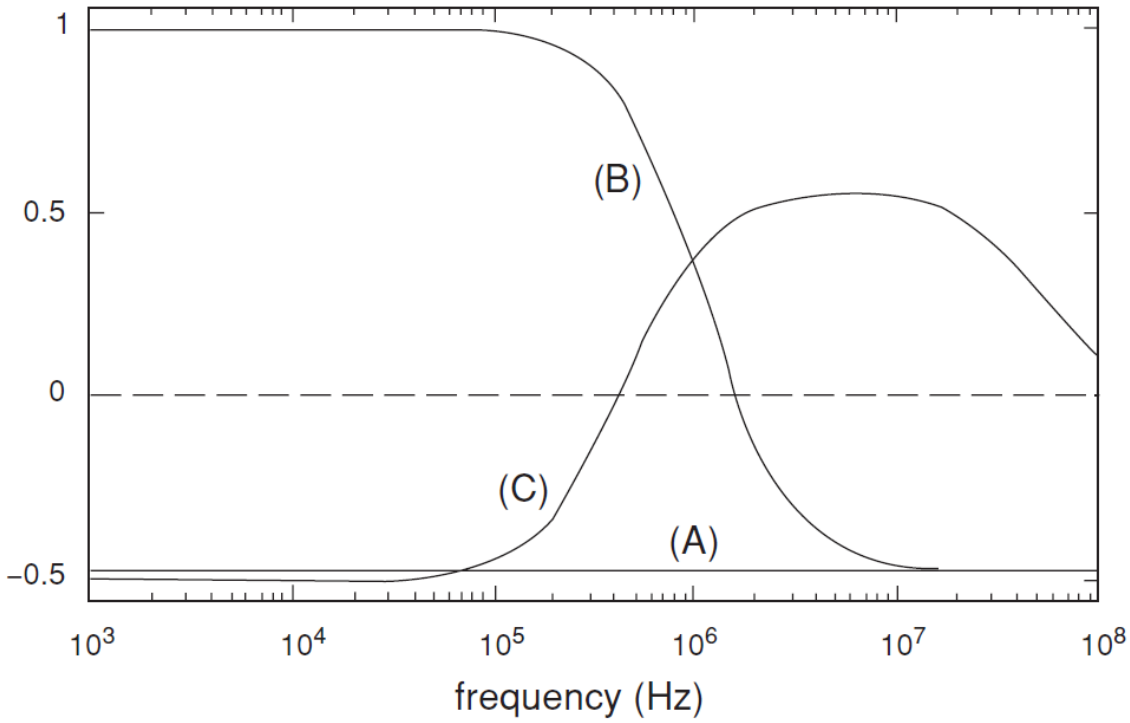

Figure 3.4. K Factor for three situations. (A) A non-conducting uniform sphere with ε_p=2.4 in non-conducting water (ε_p = 80). The water is much more polarizable than the sphere, and thus the K factor is approx.−0.5 over frequency band. (B) The same sphere, but with a conductivity σ_p=0.01 S/m in non-conducting water, there is one dispersion at low frequencies the particle is much more conducting than the water, hence there is p-DEP, while at high frequencies the situation is as in (A). (C) A spherical shell (approximating a mammalian cell), with (ε_{cyto}= 75, c_m=1 μF/cm2, σ_{cyto}= 0.5 S/m, g_m=5 mS/cm2) in a 0.1 S/m salt solution, calculated using results from [46]. There are two interfaces and thus two dispersions. Depending on the frequency, the shell can experience n-DEP or p-DEP.

3.3.2 Electro-rotation

Multi-polar electrode structure, shown in Figure 3.5, can be excited and create a rotating electric field by applying multi-phase ac voltage into multiple electrodes. If the field rotates counter-clockwise, a vector phasor form on the axis can be given by:

$$\vec{E}(x,y) = E_0(\vec{x} - j\vec{y}) \qquad (3.12)$$

where $\vec{x}$ and $\vec{y}$ are orthogonal unit vectors. If a spherical particle is introduced at the center, its induced dipole moment is

$$\vec{P}_{eff} = 4\pi\varepsilon_m R^3 K E_0(\vec{x} - j\vec{y}) \qquad (3.13)$$

This dipole moment rotates the particle synchronously with a rotating electric field but lags behind it by a phase factor associated with the complex, frequency-dependent K factor which is the phase factor that makes electro-rotation possible. The time-average electro-rotational torque is given by

$$\vec{\mathrm{T}} = -4\pi\varepsilon_m R^3 Im[K(\omega)]E_0^2 \qquad (3.14)$$

The torque depends on the imaginary part of $K(\omega)$, which is nonzero only if there is a loss mechanism. The positive or negative torque describes that the particle rotates in line with the electric field or in the opposite direction respectively.

.

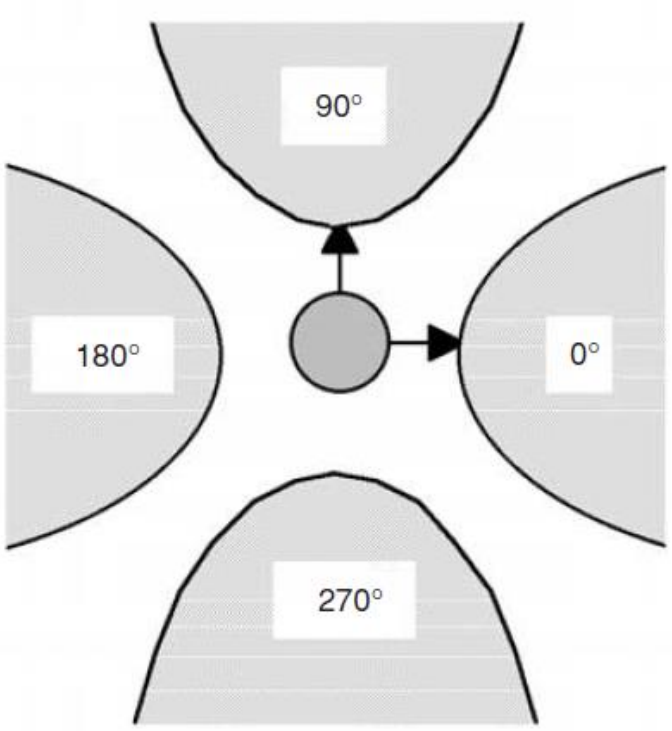

Figure 3.5 Illustration of four-pole electrode structure for electro-rotation.

3.3.3 Traveling-Wave DEP (tw DEP)

DEP forces created by applying a train of traveling-wave electric fields along a row of electrodes offer most features of conventional DEP such as trapping, size based separation and electro-rotation. A traveling-wave electric

field can be produced if the phase-shifted voltages are applied to the planar, horizontal electrode array shown in Figure 3.6 (c). The particle subjected to the traveling-wave field will move along or against the direction of field travel and even electro-rotation movement can be done with multi-phase signal application. Since, Huang published the model of traveling wave dielectrophoresis in 1992 [93], this technique has been developed and analyzed for various applications as cancer cell separation [94], multi-layer microelectrode array tw DEP device [95], higher sensitivity tw DEP with signal superposition [96] and so on.

For quadrupole electrode structure, assuming the electrodes are equally spaced and the phase angle change across each electrode is constant, the tw DEP acting on a particle in the electric field is given by [97] ;

$$\mathrm{F}_{twDEP} = -\frac{4\pi^2 \varepsilon_m}{\lambda} R^3 Im[K(\omega)] E_0^2 \qquad (3.15)$$

where λ is the wavelength of the traveling field, which is the distance between every fourth electrodes. The twDEP force is hence inversely proportion to the wavelength and the smallest possible spacing of the electrodes relative to the particle size should be designed to effectively manipulate the particles.

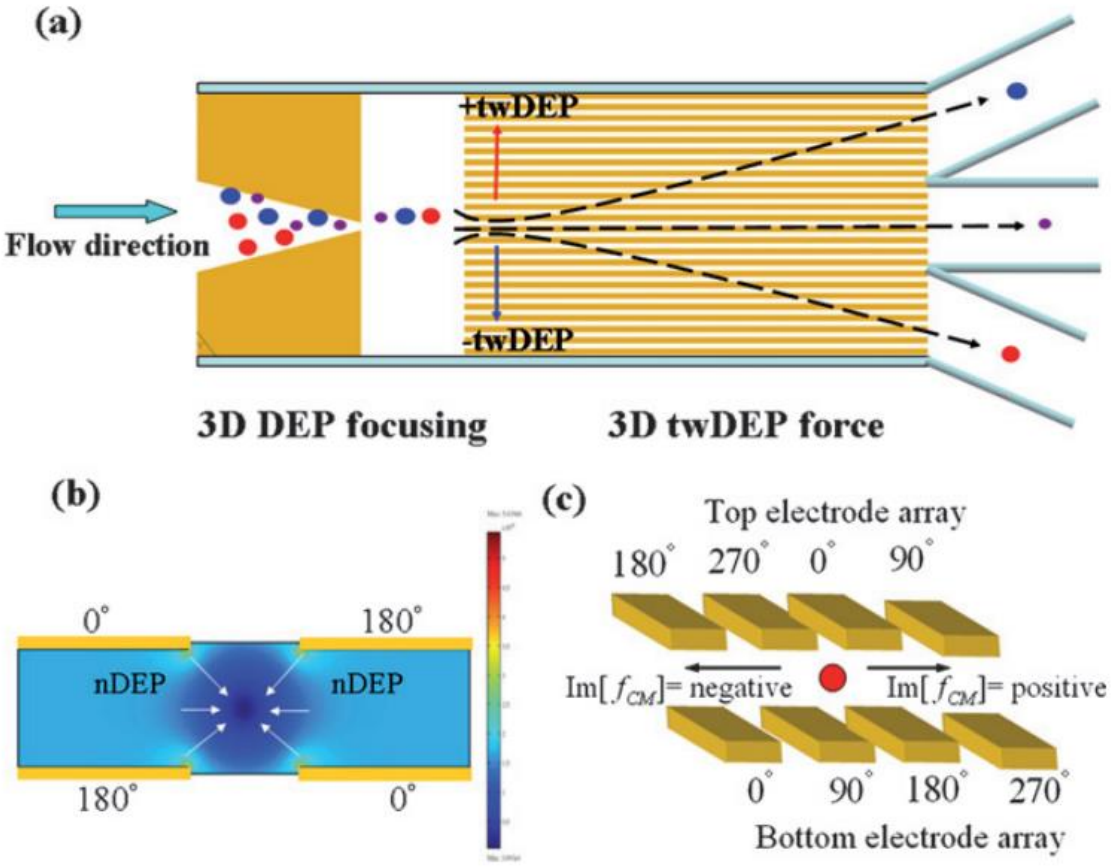

Figure 3.6 Schematic diagram of the 3D electrode design for tw DEP. (a) Top view of electrode structure, particles experience different directions or different velocities of tw DEP which transport them into relative outlets. (b) Side view of electrode structure depicting particles being repelled away from the electrode by n-DEP and (c) transported in different directions depending on the imaginary part of their CM factors. [95]

3.3.4 Label free impedance based detection

Label-free operation is one of most useful features of electrical impedance based biosensing/detection techniques. The capability of label-free operation is inherent in the DEP technique because DEP based cell manipulation depends on the dielectric properties of the particle with respect to the medium. Many bio-identification/manipulation techniques require a label attached to the target. During readout, the position and/or amount of label is detected and assumed to correspond to the position and/or number of bound targets. However, labeling requires extra time, expense, and sample handling, though labeling have benefits of enhanced selectivity and sensitivity.

When a target biomolecule interacts with a probe-functionalized surface, changes in the electrical properties of the surface (e.g., dielectric constant, resistance) can result from the presence of the target molecule. Thus, no label is required for impedance sensing. In addition, label-free operation enables detection of target-probe binding in real time [97], which is generally not possible with label-based systems. Real-time sensing confers at least two major advantages over endpoint detection. First, time averaging of binding/unbinding events can improve measurement accuracy. Second, it allows determination of affinity constants by curve-fitting the sensor output vs. time [98]. In short, DEP based detection/sensing techniques have potential for label-free, real-time monitoring and low cost with help of micro-fabrication technology. We will propose novel CMOS based DEP cell monitoring technique in chapter 4.

Chapter 4

CMOS Dielectrophoretic Lab-on-Chip Platform for Manipulation and Monitoring of cells

4.1. Introduction

Micro-fabricated lab-on-a-chip based electrical cell manipulation and detection techniques are more promising than existing optical/magnetic techniques owing to low cost, smaller form factor and more functionality from integration with electronics. CMOS technology offers significant advantages compared to other custom MEMS processes such as capability of 3D microelectrode structure and feasibility of system level integration implemented

in a high yield low cost industry standard process. This enables highly-parallel high throughput implementation of DEP based functions on chip.

In this chapter, we discuss the design and implementation of a CMOS based platform to perform DEP trapping of single or group of cells in high throughput manner. This proposed platform has another feature of reconfigurability by on-off signal switching that provides additional control to the movement of cells. Important issue is 3D multi-electrode design using built-in metal layers which must provide positive (or negative) trap which correspond to spatially confined maximum (or minimum) of electric fields for trapping. We present 3D octapole electrode design implemented using the built-in layers of the standard 0.5µm CMOS process. Detailed electro-magnetic simulations regarding electric field strength and experiments have been carried out with centrifuged yeast cells, which validate the design. Given the need to perform the operation in real-time, in-situ impedance monitoring of the trapping function, readout circuitry has been integrated with DEP electrodes on the same chip for a complete single chip solution. Using this analog front end for impedance monitoring of biological targets, we could detect the cell repositioning on reconfigurable 3D electrodes in real-time. It is important to mention that the approaches presented here can be easily scaled to sorting and identification of other cells and microorganisms and could be focus of future work.

4.2. 3D reconfigurable electrodes for DEP trap

4.2.1 3D DEP electrode arrangement

With recent remarkable advances in micro-fabrication technology, 3D electrode structures for DEP trapping have been introduced to overcome the limitation of planar electrodes [99,100,101]. For example, in n-DEP trapping using planar electrodes, the n-DEP force is quite balanced by the gravitational force. This means that it is not possible to increase the retention force by increasing the driving voltage since the force just moves the particle further away from the electrodes. Furthermore, 3D electrode structures create significantly stronger DEP force than planar electrodes, so it is used to trap single particle or particles with lower density. Figure 4.1 shows conventional electrode structures for DEP trapping ranging from planar interdigitated electrodes to multi-layer crossed electrodes. Among 2D structures, planar quadrupole electrodes are useful structures for DEP trapping and electro-rotation, which have four electrodes with alternating voltage polarities applied to every other electrode as shown Figure 4.2(b),(c). They have been also known to have ability to trap single particle down to hundreds of nm [102]. However, these 2D traps cannot increase confinement by increasing the electric field as mentioned. In order to overcome this drawback, some studies have introduced 3D DEP structures such as extruded quadrupole traps (Figure 4.2 (d), (e)) and stacked multilayer structures (Figure 4.2 (f) to (j)). Although those traps are much more difficult to be made, they are orders of

magnitude stronger than the planar quadrupole traps, and can successfully hold single cells against significant liquid flows. These electrode geometries are sufficiently complicated that only numerical simulation can derive the correct field solution.

The approaches for dielectrophoretic assembly with microscale and nanoscale objects can imply opportunities for better controllability and precise positioning of biological objects using DEP. While most applications of dielectrophoretic assembly aim at programmable nano-electronics rather than biotechnology [103], proposed electrode structures for this methodology can be employed to DEP manipulation of bio targets with better positioning and controllability. Figure 4.2 shows an example of precise positioning by ac dielectrophoresis using single-walled carbon nanotubes (SWCNTs) [104]. Several studies also focused on chemical sensing by DEP assembly of nanomaterials, where those chips were implemented in CMOS process [105,106,107]. A considerable degree of control over the dielectrophoretic alignment of carbon nanotubes using pre-patterned microelectrodes has been obtained as shown in Figure 4.2 (b). In particular, floating potential posts can guide nanotubes across primary electrodes along predefined and predictable paths. Another study regarding dielectrophoretic reconfiguration of nanowire interconnects has been presented by A. D. Wissner-Gross [108]. As shown in Figure 4.3, phase inversion of electrode potentials in planar three electrode structure allows the reversible reconfiguration of nanowires, either serially or in parallel. Various electrodes

structures coming from dielectrophoretic assembly methods can give hints to DEP manipulation in bio application [109,110].

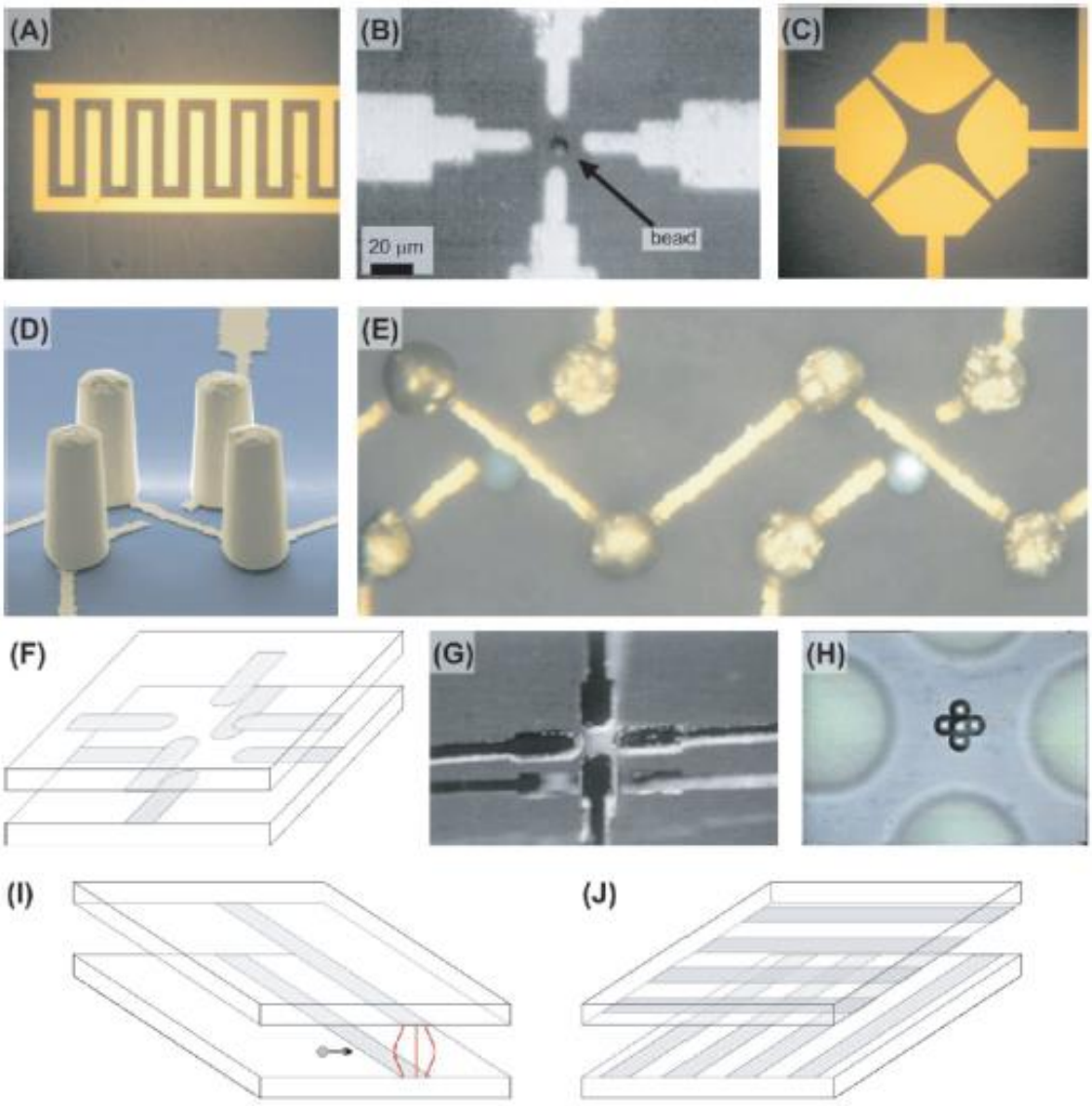

Figure 4.1 DEP trapping electrode structures. (A) Interdigitated electrodes. (B) A planar quadrupole, showing a bead in the center. (C) Quadrupolar polynomial electrodes. (D) A 3-D view of an extruded quadrupole trap, showing the four gold post electrode electrodes and the gold wiring on the substrate. (E) A top-down image of two extruded quadrupole traps showing living trapped HL-60 cells in liquid. (F–H) Schematic of the oppose octapole (F) Stereo image (G) Topdown view (H) Showing beads trapped at the center. (I) Schematic of the strip electrodes, showing the non-uniform electric field between them that creates an n-DEP force wall to incoming particles. (J) Schematic of the crossed-electrode p-DEP structure of Suehiro [101]

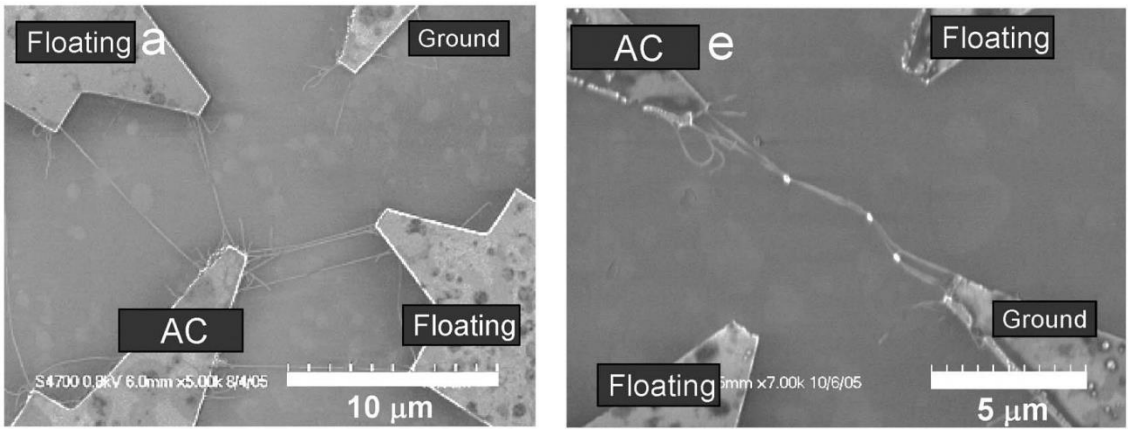

(a) (b)

Figure 4.2 Precise positioning by ac dielectrophoresis using single-walled carbon nanotubes (SWCNTs) (a) Single wall carbon nanotubes aligned across a 10 μm gap without any strips or posts in the gap. Some tubes were seen to bind to the floating electrodes. (b) Single wall carbon nanotubes zigzag aligned between 300nm diameter posts across the gap.

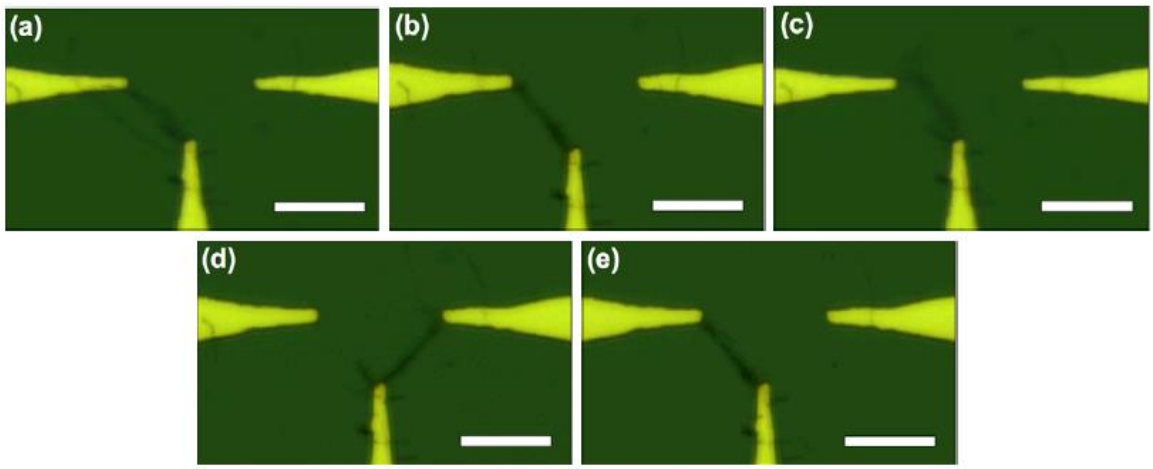

Figure 4.3 **T**hree-electrode serial reconfiguration of nanowires. The relative phase between the left (source) and middle (latch) electrodes is modulated from (a), (b) 180° to (c), (d) 0° to (e) 180°. The scale bars are 15 μm.

4.2.2 Design and simulation of 3D electrodes geometry

CMOS process benefits from the availability of multiple layers of metal used for electrical interconnects which can be utilized to create complex 2D and 3D multi-electrode arrangements to implement efficient traps for cells. As mentioned earlier, 3D multi-electrode configurations can generate a more controlled and reconfigurable electric field for target particles, compared to planar 2D designs. Basically, DEP electrode geometries should be explored based on three metrics: (1) Spatial confinement of trap (comparable to the size of cell to be trapped), (2) Strength of electric field in trap (as high as possible for positive DEP), and (3) Gradient distribution of the electric field away from the trap (as high as possible). Based on the design rules which dictate the minimum spacing between metal layers in a given 0.5um CMOS process, three designs were selected. The electric field distribution for the electrodes were modeled using electromagnetic simulation software (Ansoft Maxwell 3D). For simulation, all dimensions and material properties such as permittivity, conductivity and so on, have been employed from the available 0.5um standard CMOS technology. Figure 4.4 shows two of the 3D electrode geometries and their electric field distributions around the electrodes; the DEP force is proportional to the square of the gradient of this electric field. Quadruple electrode geometry in Figure 4.4(a) is most typical 3D electrode structure for DEP trapping, which is composed of symmetrical four electrodes with 10um electrode gap.

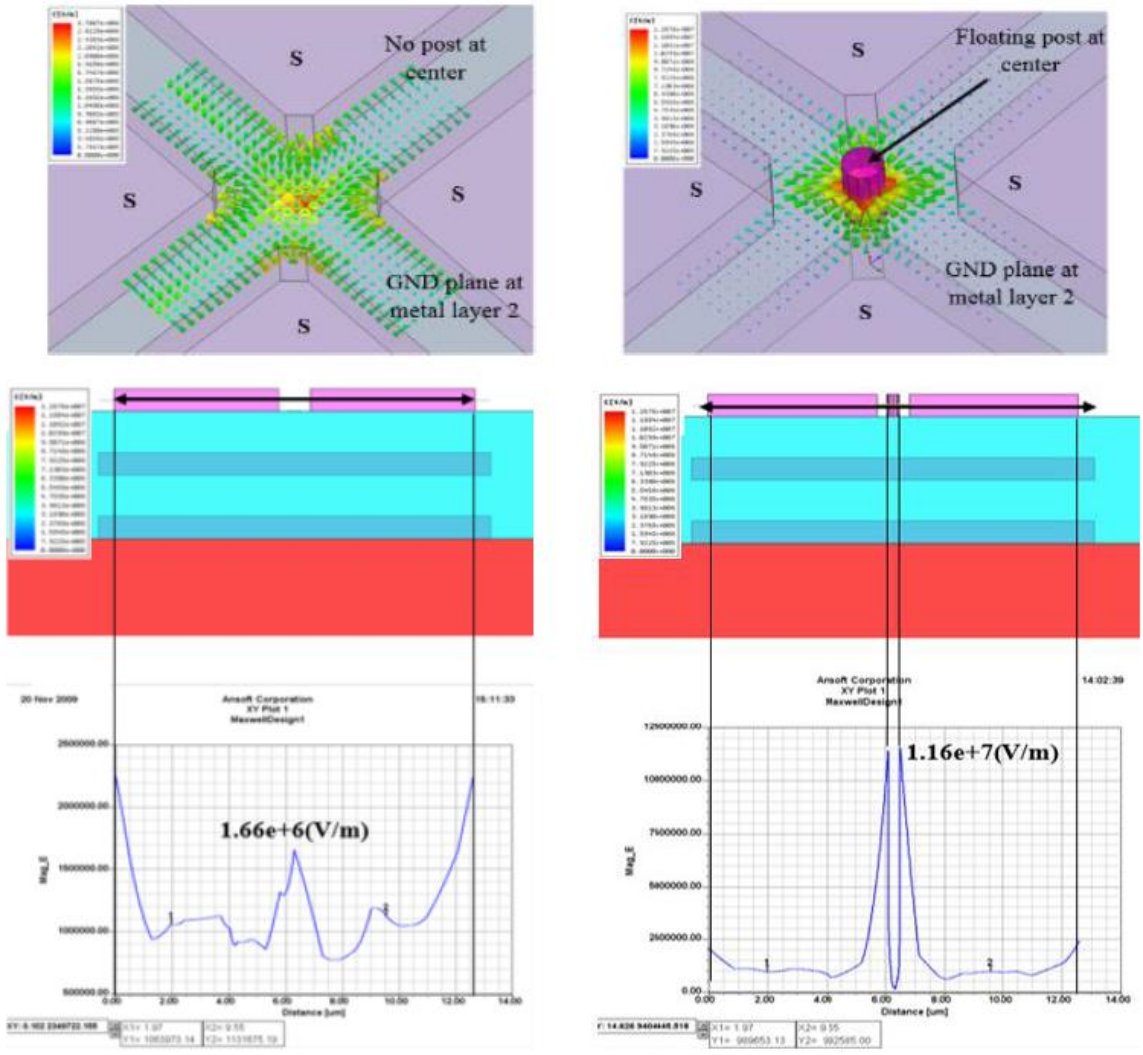

Figure 4.4 3D electrode geometries and simulation of electrical field strength for dielectrophoretic cell manipulation (a) Quadrupole DEP structure (b) Quadrupole DEP structure with floating metal post

Multi-polar electrode structure is chosen to enable electro-rotation of trapped cells by applying multi-phase ac voltage into multiple electrodes. Increasing number of electrodes facilitates more exquisite manipulation for target particle. Another design utilizes floating metal posts within the electrode gaps to increase the electric field in the gap and create much higher gradient; this

translates into stronger DEP force and precise particle positioning [104]. We designed and simulated this electrode geometry of quadrupoles with 10um electrode gap and a floating post of 5um diameter at the center of the electrodes. However, these approaches do not provide controllability such as programmable positioning or reorientation, and the size restrictions due to the design rules of the CMOS process, which limits the maximum strength and gradient of the electric field needed for efficient trap.

Figure 4.5 shows the third and the preferred 3D electrode geometry and signal excitations at each electrode in this multi-electrode geometry for the purpose of cell trapping with the added ability to switch orientations of trap for rotational movement. The DEP structure consists of octapole electrodes where four electrodes with 5.7um gap on top layer are symmetrically placed along with four pedestal planes on bottom layer. AC and grounding signals to the multiple electrodes in this geometry is shown in Figure 4.5 (d). In contrast to traditional octapole geometry using multi-phase signal excitation, our proposed structure can have reconfigurability with simple on-off switching. This particular biasing would generate electric field gradient between the AC and ground electrodes at the top layer.

Figure 4.6 shows the simulated rotating electric field indicating a strong confinement in one of four directions that can be easily reoriented by changing the electrodes that were connected to AC signal and ground. This is far easier than in conventional DEP multipolar structures where the signal excitation scheme will

require complex phase shift circuitry in LoC platform to generate a multi-phase signal for such reorientations.

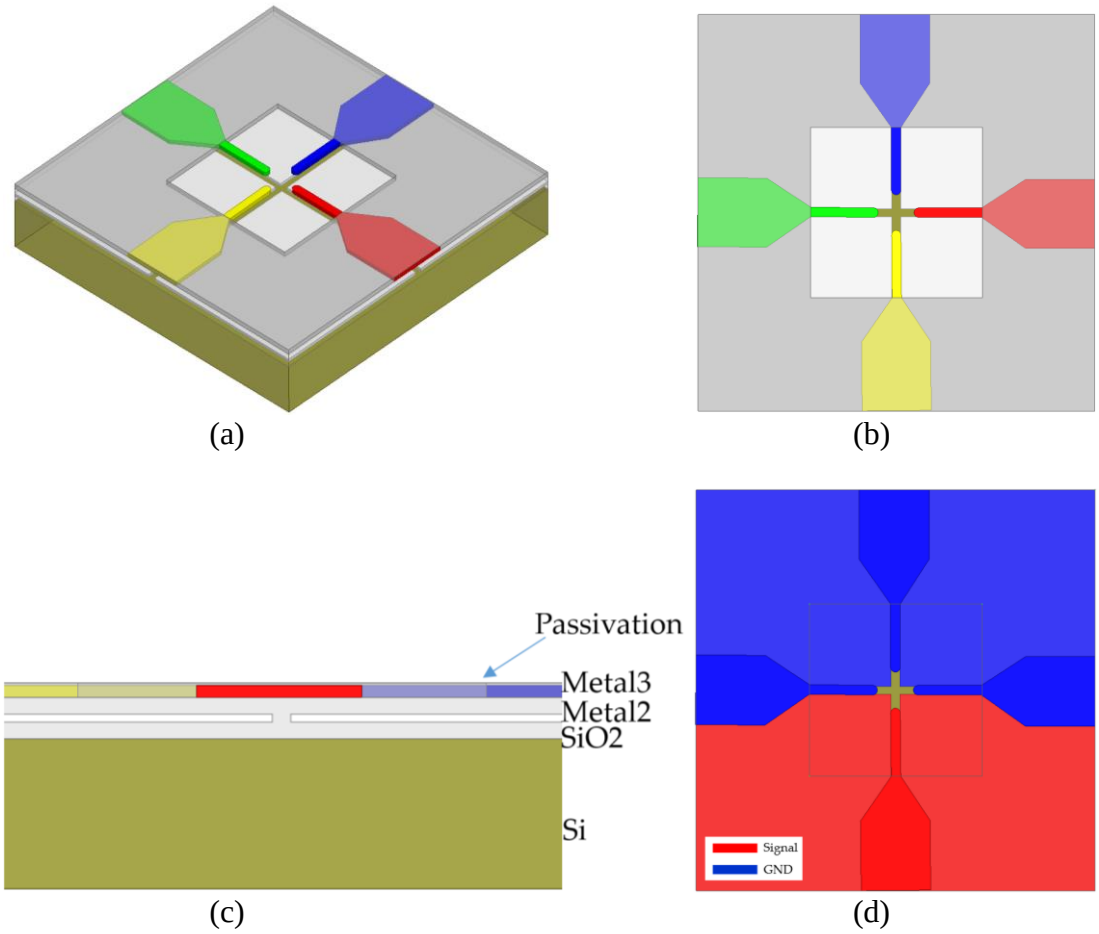

Figure 4.5 Proposed reconfigurable electrode geometry for dielectrophoretic cell trapping and electro-rotation (a) 3D octa-pole DEP structure (b) Top view (c) Cross sectional view of DEP structure implemented by CMOS process (d) Signal excitation pattern on the multi-polar electrodes

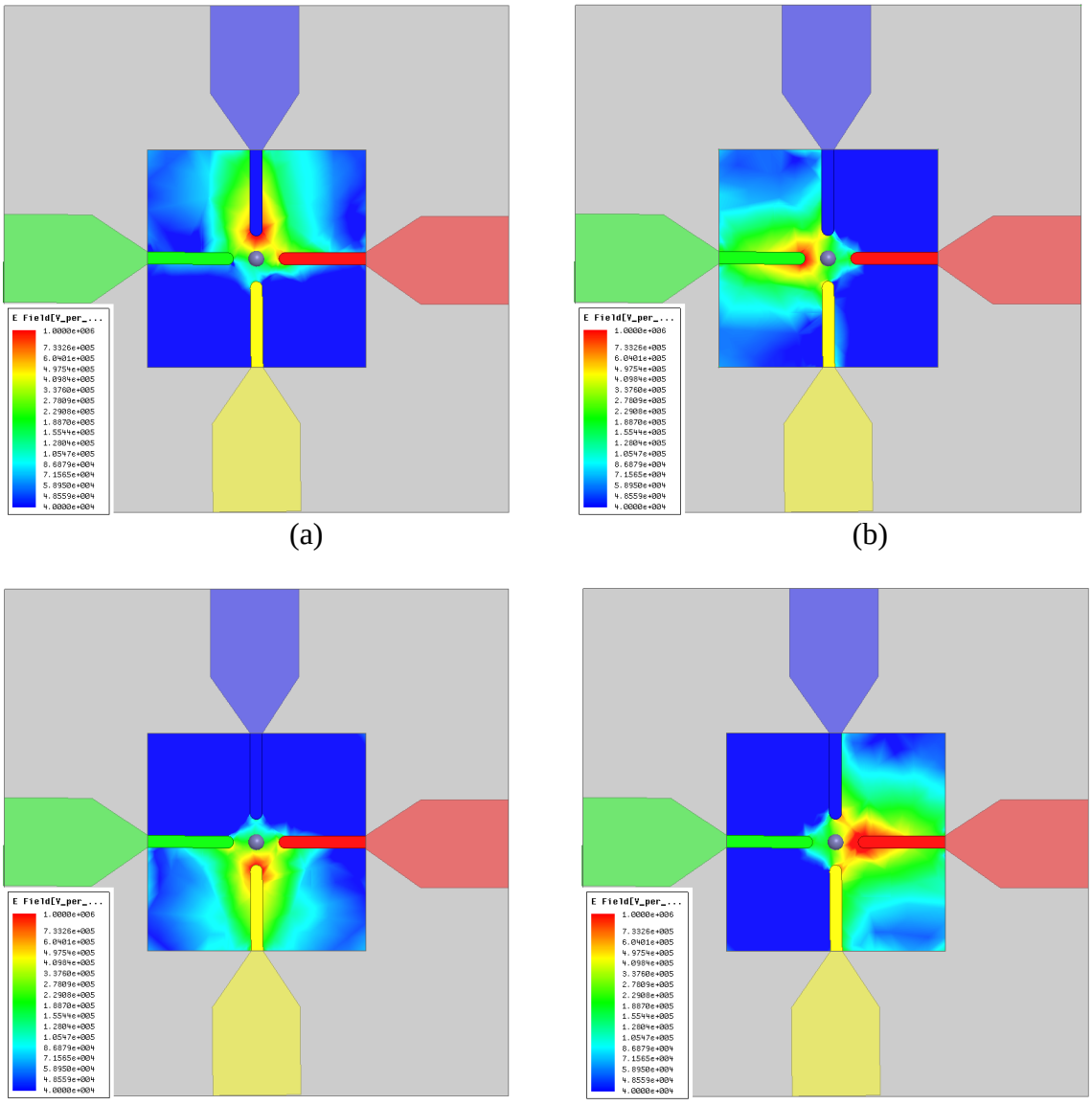

Figure 4.6 Electromagnetic Simulation of proposed reconfigurable 3D octa-pole electrode geometry. Electric field strength with excitation of 3 electrodes at (a) top side (b) left side (c) bottom side (d) right side. AC signal of 1MHz and 5Vp-p applied to the electrodes. The material of medium is distilled water with high dielectric constant of 80.

4.3. Proposed LoC platform and sample preparation

4.3.1 Fabrication of single chip LoC platform on CMOS

A. 3D DEP electrodes

The proposed DEP LoC platform with 3D reconfigurable electrodes has been fabricated in On Semi 0.5um CMOS process. This single chip platform includes 4 sites of octapole DEP structure with an integrated operational amplifier in TIA topology as analog front end for electrical impedance measurement.

In Figure 4.7, microscopic images of reconfigurable LoC platform fabricated in CMOS process are presented. Figure 4.7 (a) shows 1.6mm X 2.0mm sized single chip platform with integrated operational amplifier (OP-AMP) used for impedance measurement. The schematic of the on-chip operational amplifier is also shown in Figure 4.8. The integrated OP-AMP consumes 10mW with 5V supply voltage. Details of the OP-AMP is shown in Table 2. Figure 4.7 (b) is a detail view of multilayer octa-pole DEP electrodes.

Packaging is also important to mount the chip onto a test board and run measurements. LCC28 package was used to mount and wirebond the CMOS chip to package pins. Then, fully packaged chip has been assembled on a printed circuit board (PCB) with external circuits for readout of impedance.

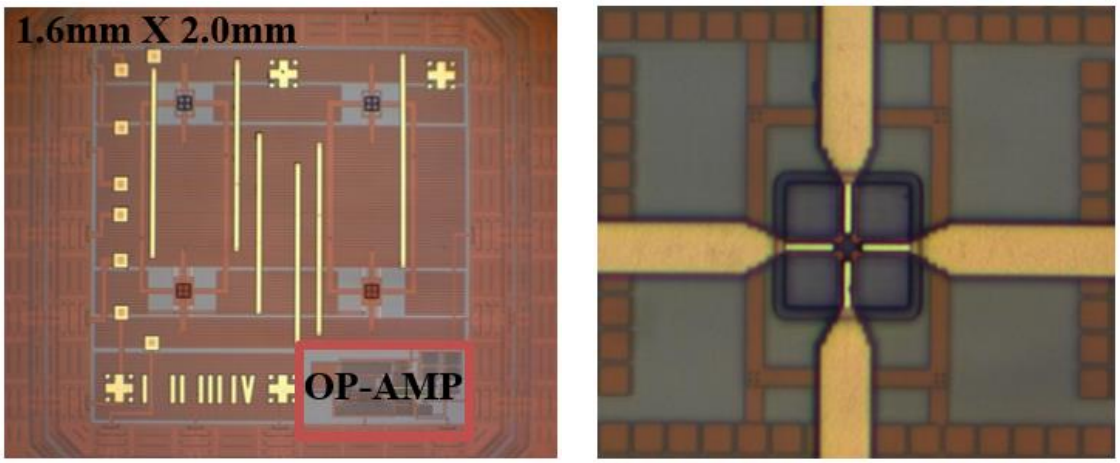

(a) (b)

Figure 4.7 Reconfigurable LoC platform on CMOS (a) CMOS microphotograph - dimension is 1.6mm X 2.0mm. Chip shows OP-AMP used for impedance measurement (b) Detail view of 3D octa-pole DEP electrodes (c) Before and after PDMS wall on CMOS chip

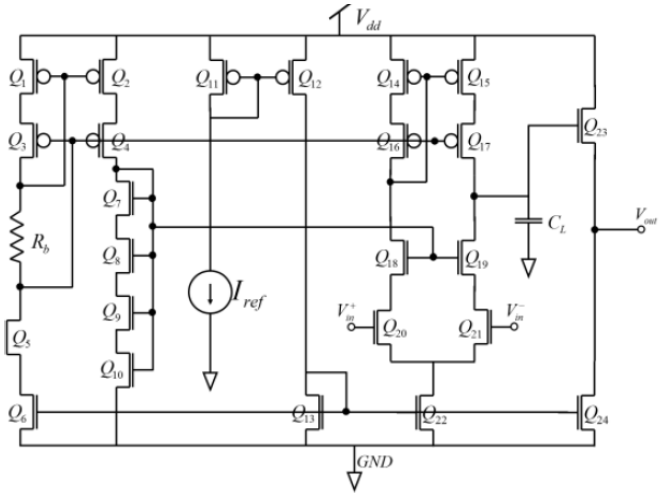

Figure 4.8 Schematic of on-chip operational amplifier for impedance monitoring

Table 2. Details of integrated operational amplifier

Parameter	**Specification**
Vdd	5V
C_L	1pF
Iref	400uA
Common mode voltage	1.5V
DC gain	65.03 dB
GBW	56.15 MHz
PM	60.086˚

B. Well fabrication

In order to protect all electronics in the chip from aqueous biological media during testing, polydimethylsiloxane (PDMS) well was fabricated onto the chip as shown in Figure 4.9. For the cavity open encapsulation, PDMS base was mixed with a curing agent with the ratio of 10:1. Then it was placed in a vacuum chamber to remove bubbles. The chip was placed on the heater with a temperature of 80 °C and a thin layer of PDMS was added around the electrodes and immediately cured before spreading all around. All this process was monitored under microscope and repeated several time to make a deep well with the approximate height of 2mm.

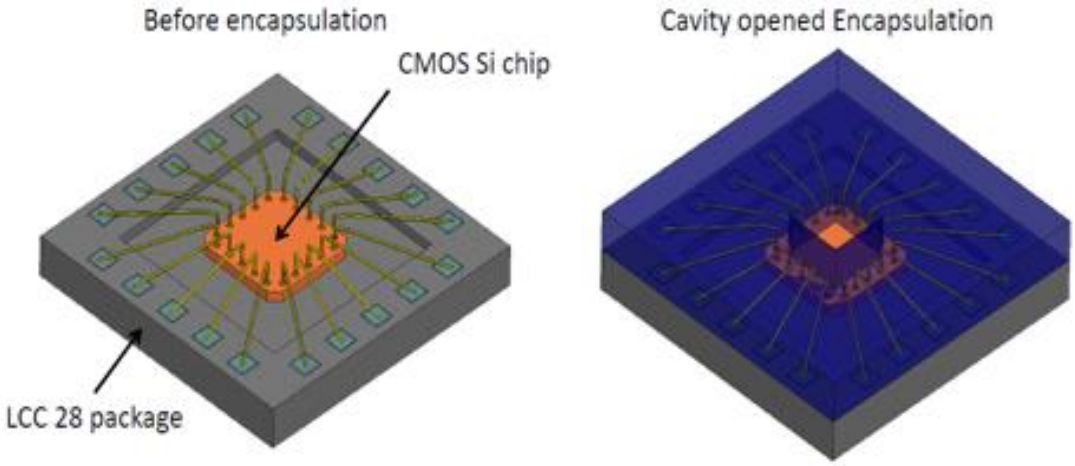

(a) (b)

Figure 4.9 PDMS wall protection (a) Before and (b) after PDMS wall on CMOS chip

4.3.2 Preparation of yeast cell solution

DEP response of yeast cells

In our experiments, we used yeast cells as test sample to be trapped in the LoC platform. Due to the discrepancy in the electric conductivities and the complex permittivities of live and dead yeast cells, those cells respond dissimilarly to AC electric field [111]. Figure 4.10 compares the model predicted K factors of the two types of cells suspended in 1mM phosphate buffer as a function of the AC field frequency (from 1 kHz to 1MHz). In the range from a pure DC field to a 500 kHz AC field, both types of cells possess a negative K factor and hence experience negative DEP. At around 200 kHz, the DEP responses become comparable between the two types of cells and their relative difference even reverses. For frequencies higher than 500 kHz, live yeast cells start to experience a positive DEP while dead cells still keep tied to a negative DEP.

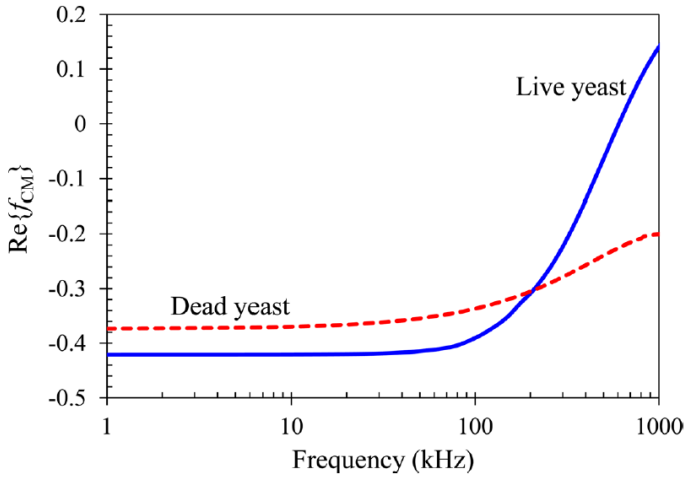

Figure 4.10 Comparison of the model predicted K factors of live (solid line) and dead (dashed line) yeast cells suspended in 1mM phosphate buffer as a function of the electric field frequency. Positive DEP (Re{ f_{CM} }>0) and negative DEP (Re{f_{CM}}<0) region are different over frequency for live and dead yeast cells. [111]

Yeast Cell preparation

The gap between electrodes is 5 µm but yeast cells have the size distribution between 4 to 8 µm. To separate smaller size of yeast cells, yeast cells were suspended in 0.85 % of NaCl solution and centrifuged for 5 sec in 100 rpm then the upper solution which is contains smaller cells, separated and transferred to another centrifuge tube. In the next step cells were washed three times with deionized water (DI) and suspended in Phosphate buffered saline (PBS) with final concentration of 10^6 cells/mL.

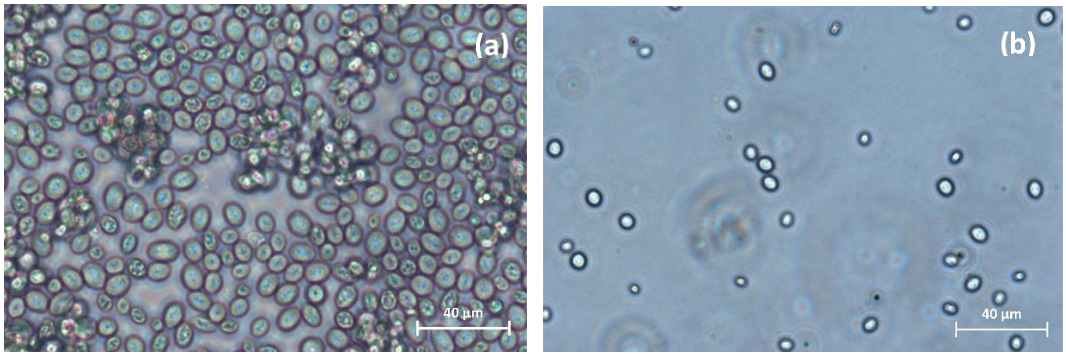

Figure 4.11 Yeast cells (a) before doing centrifuge and (b) after doing centrifuge.

4.4. Experimental Results

Experiments were performed to demonstrate cell trapping and its control of the proposed dielectrophoretic LoC platform with live yeast cells. Since we need to have yeast cells exposed to positive DEP for trapping, pure viable cells have been tested with higher frequency than 500KHz for experimental consistency. We observed yeast cell trapping and repositioning by CCD camera connected to the microscope.

4.4.1 Single cell trapping

Figure 4.12 describes sequential images of single yeast cell trapping in the 3D DEP electrodes. We applied 5Vp-p, 1 MHz AC sinusoidal signal to the electrode of left side in top layer and a pair of electrodes of left side in bottom layer. All other electrodes have been grounded. Since viable yeast cells respond to positive DEP at the applied signal frequency, each individual yeast cell in the neighborhood of the electrodes will finally gather to the center of the DEP trap.

Proposed 3D octapole geometry and signal application scheme also provide the ability to control cell positioning and reorientation through simple switching of signal to a suitable set of electrodes. Figure 4.13 shows that single yeast cell can be trapped and repositioned by alternating AC signal to two sets of electrodes in the DEP structure. First, a horizontal DEP force was generated by applying 5Vp-p, 1 MHz AC signal to a set of electrodes at right side and a yeast cell in diluted solution was trapped and positioned on the right. When the AC signal excitation is switched to another set of electrodes at the down side, the direction of DEP force is perpendicular to the prior force and the trapped cell moved quickly to the down side electrode. Finally, as soon as AC signal was switched back to right set of electrodes, yeast cell repositioned to the original location promptly. Given the nature of the force depends on the cell permittivity, size and density, there is potential for trapping single or multiple cells based on these parameters.

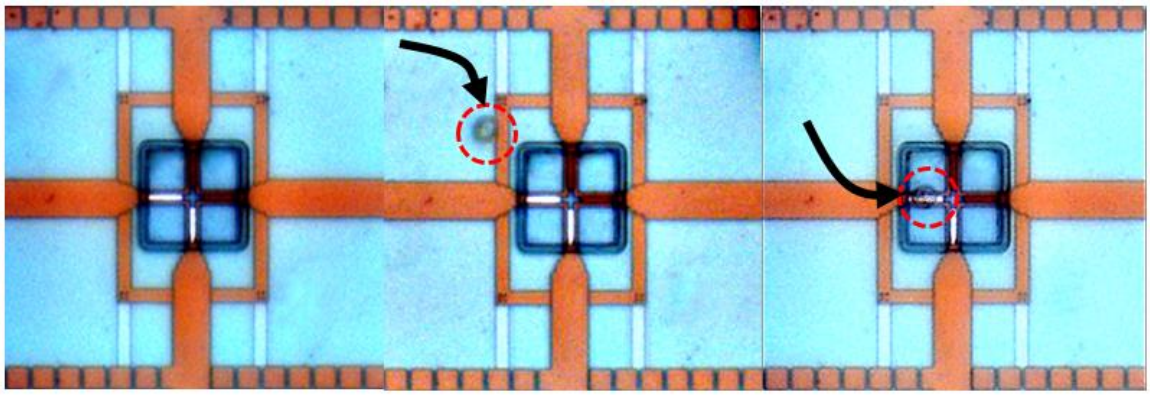

Figure 4.12 Single yeast cell trapping by positive DEP on 3D octa-pole electrode (a) before applying AC sinusoidal signal (b) Yeast cell moves due to p-DEP after applying AC signal (c) Yeast cell trapped

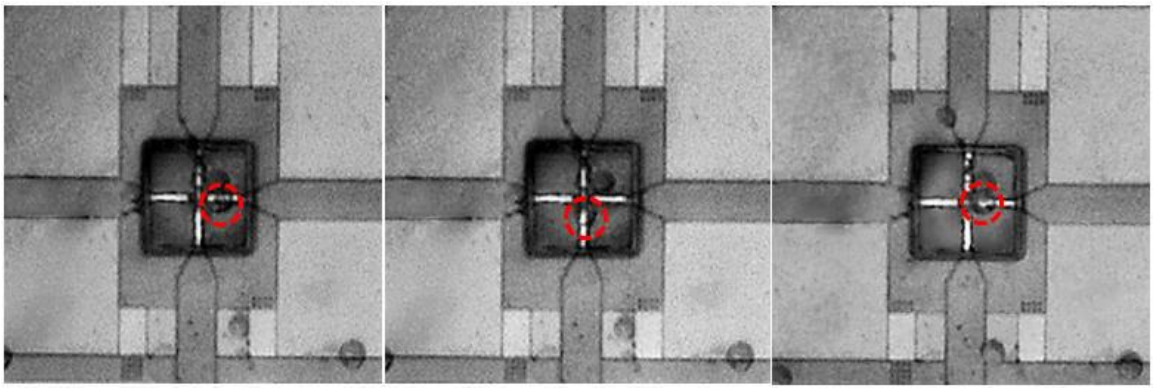

Figure 4.13. Single yeast cell repositioning by positive DEP and switching AC signal to 3D octapole electrodes (a) Cell positioned at the electrode of right side with initial excitation before signal switching (b) Cell moved to the electrode of bottom side after signal switching (c) Cell repositioned to the electrode of right side with signal switched back

4.4.2 Parameter analysis

Applied voltage

From calculations of the time averaged DEP force for dielectric particle, DEP force is proportional to electric field gradient(∇E_0^2), which is directly related

to applied voltage. The experiment for change of applied AC voltage from 100mVp-p to 10Vp-p, where the frequency has set to 700 KHz, was performed and the microscopic images for varying voltages are displayed in Figure 4.14. In order to guarantee all the experiments have done with same test condition, we used same concentration and volume of yeast cell solution and let the cells exposed to DEP force for same time duration 30 seconds. As higher voltages applied to the electrodes, the number of trapped yeast cells inside the rectangular DEP site increased along with the voltage. Also, confined time for the cells was drastically reduced as voltage went up. The graph in Figure 4.15 explains that DEP force gets exponential increments at higher voltage than 5Vp-p.

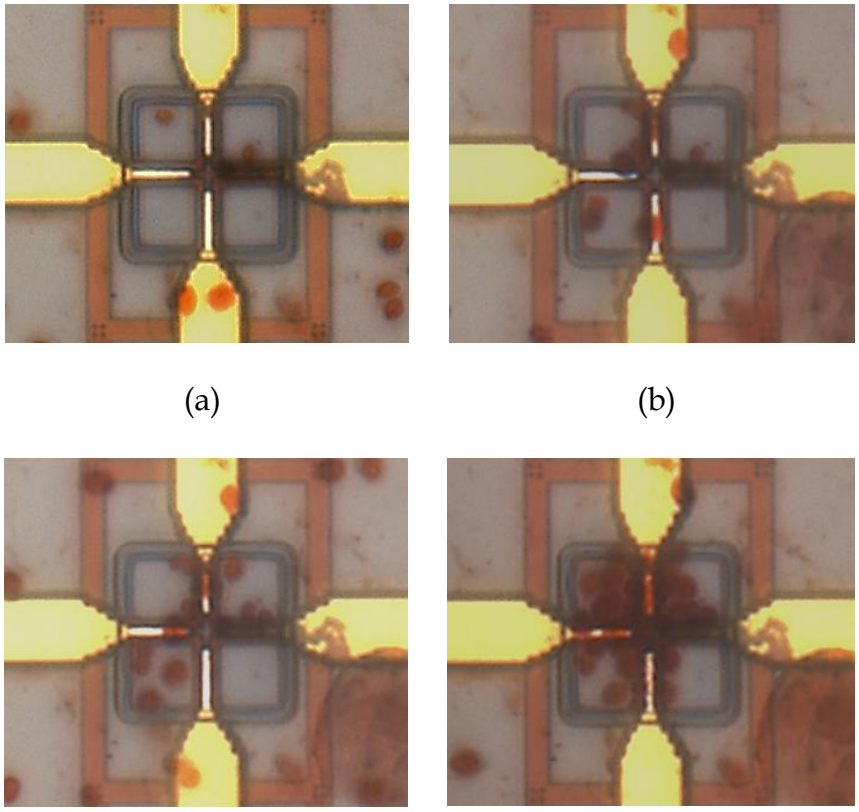

Figure 4.14. DEP trapping of yeast cells for application of varying voltage (a) 100mVp-p (b) 1Vp-p (c) 5Vp-p (d) 10 Vp-p with 700KHz

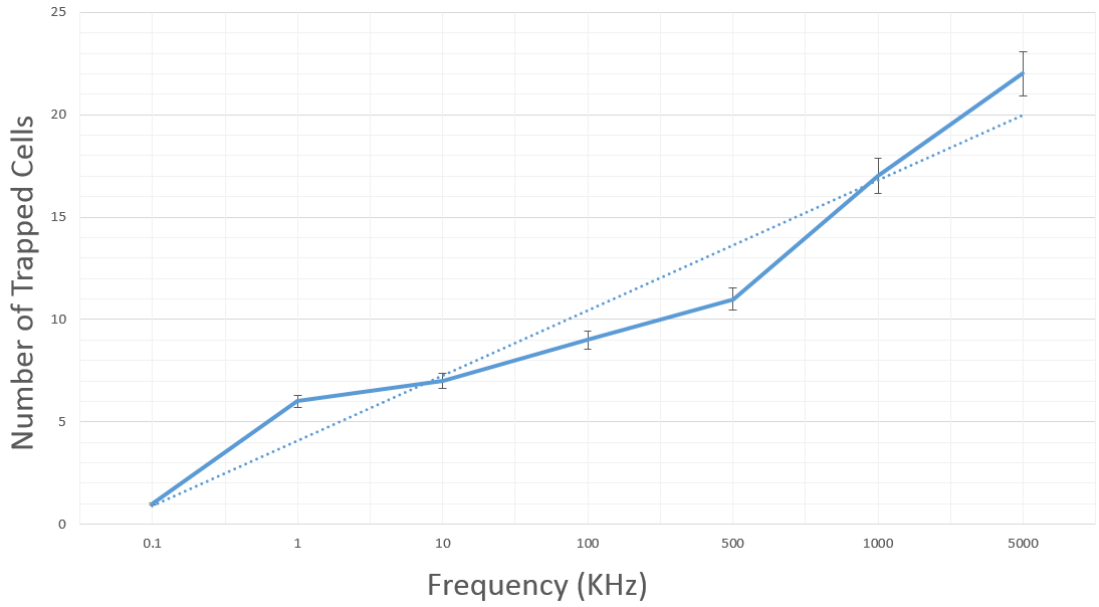

Figure 4.15. Number of trapped yeast cell vs. Applied voltage change

Frequency

As we discussed in previous chapter, K factor is most critical for direction and strength of DEP force, which is frequency dependent parameter. By predicting K factor of live yeast cell through two-shell model, the live yeast cells is expected to experience DEP force switching from negative to positive when frequency of applied signal sweeps. Similar to the voltage variation test, all the experiments have carried out with identical voltage of 5Vp-p and same yeast cell solution during 30 seconds time duration. Frequency swept from 100Hz to 5MHz. Figure 4.16 shows that the more live yeast cells have been trapped exponentially at higher frequency than 500 KHz, while there was no significant difference for the number of trapped cells at less than 100 KHz. This result is in line with the prediction of K factor for yeast cell model, implying DEP force switched negative to positive around 500KHz. Gradual increment of the trapped cells from 100 Hz to 100 KHz might be caused by hydrodynamic drag force rather than DEP force because no cell is seen to be trapped at electrodes by positive DEP.

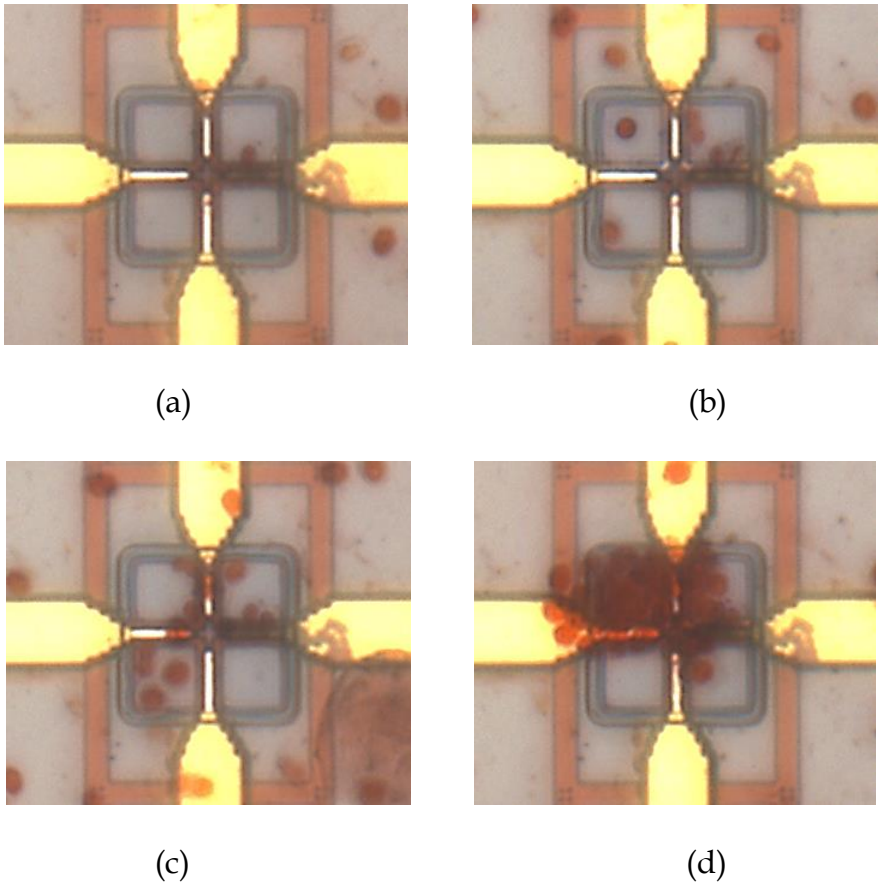

Figure 4.16. DEP trapping of yeast cells for frequency sweep from 100Hz to 5MHz (a) 100 Hz (b) 10 KHz (c) 500 KHz (d) 5 MHz

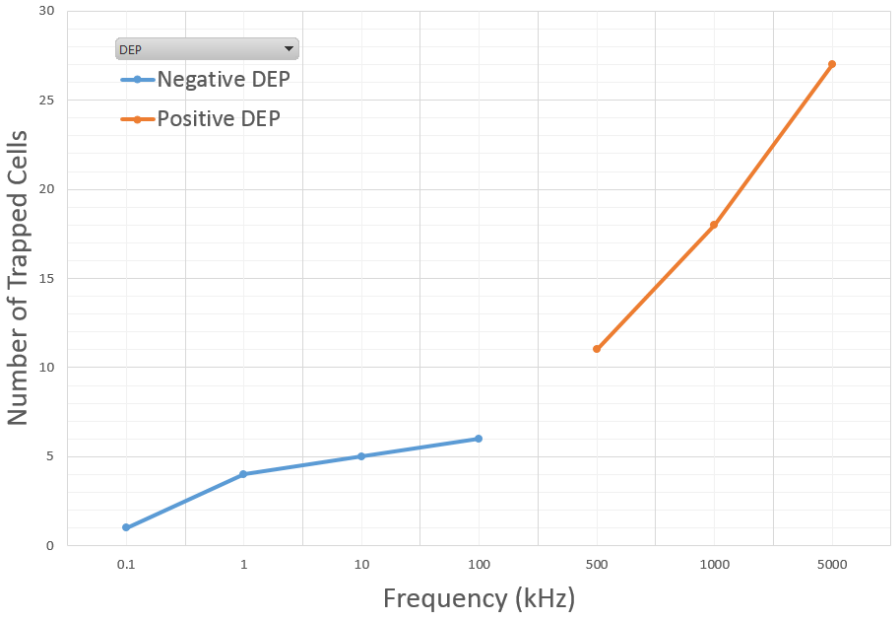

Figure 4.17. Number of trapped yeast cell vs. Frequency

4.4.3 Impedance detection of cell repositioning

Electrical sensing of cell location and properties is highly desirable compared to visual inspection for portable in-situ real time monitoring. We implemented a trans-impedance amplifier (TIA) to measure impedance as shown in Figure 4.18. A TIA was implemented on test board using on-chip operational amplifier in Figure 4.8 and external feedback resistor of 50 KΩ to detect impedance change due to the yeast cell repositioning by AC signal switching. We added a single-pole double-throw switch to swap AC signal application between two sets of electrodes for in-situ monitoring of impedance change. DC offset adjustment has been made to minimize an intrinsic DC offset of amplifier because its offset could conceal small voltage signal from output of TIA by cell trapping. We applied low amplitude of AC signal 2Vp-p with 1MHz to trap a cluster of few yeast cells. Supply DC voltage, common mode voltage and reference current to operate on-chip amplifier were 5V, 1.5V and 400μA, respectively and power dissipation of the TIA was approximately 10mW.

We were able to perform in-situ measurement of voltage discrepancy from TIA output due to impedance change with AC signal switching as well as validate visually as shown in Figure 4.19. Without cell trapped into the DEP electrodes, only hundreds of μV caused by DC offset was observed. When DEP signal was applied to a set of left side electrodes, AC voltage signal of 12mVp-p was detected at TIA output. Sequentially, we measured lower amplitude of 4mVp-p AC signal after switching to the bottom set of electrodes. Since a DEP signal path has been

built in the test bench from left to upside electrode, positioning and bridging of yeast cells between two electrodes results in low impedance for the path, while the cell position at opposite side introduces a higher impedance in the electrical path, which results in lower amplitude of output voltage. This result gives a positive evidence for our concept of impedimetric detection of cell reposition on proposed DEP based impedance sensing platform.

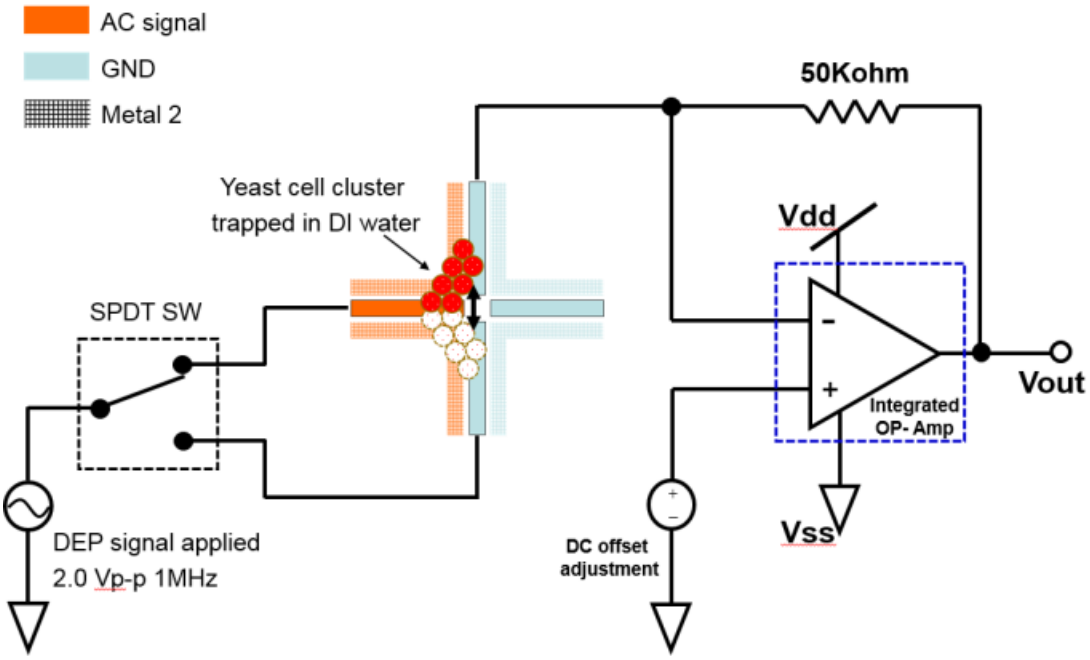

Figure 4.18. Test configuration for electrical detection of cell repositioning. Test bench consists of a SPDT switch for signal switching, proposed LoC platform and Trans-Impedance Amplifier for impedance measurement.

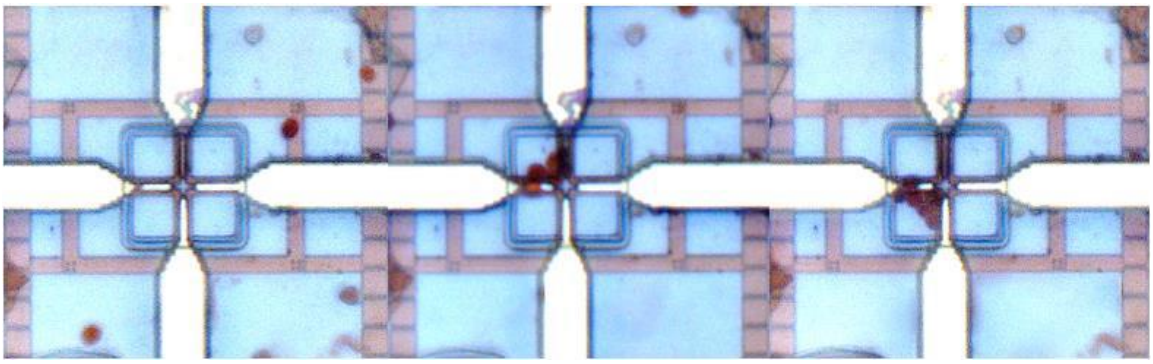

(a) (b) (c)

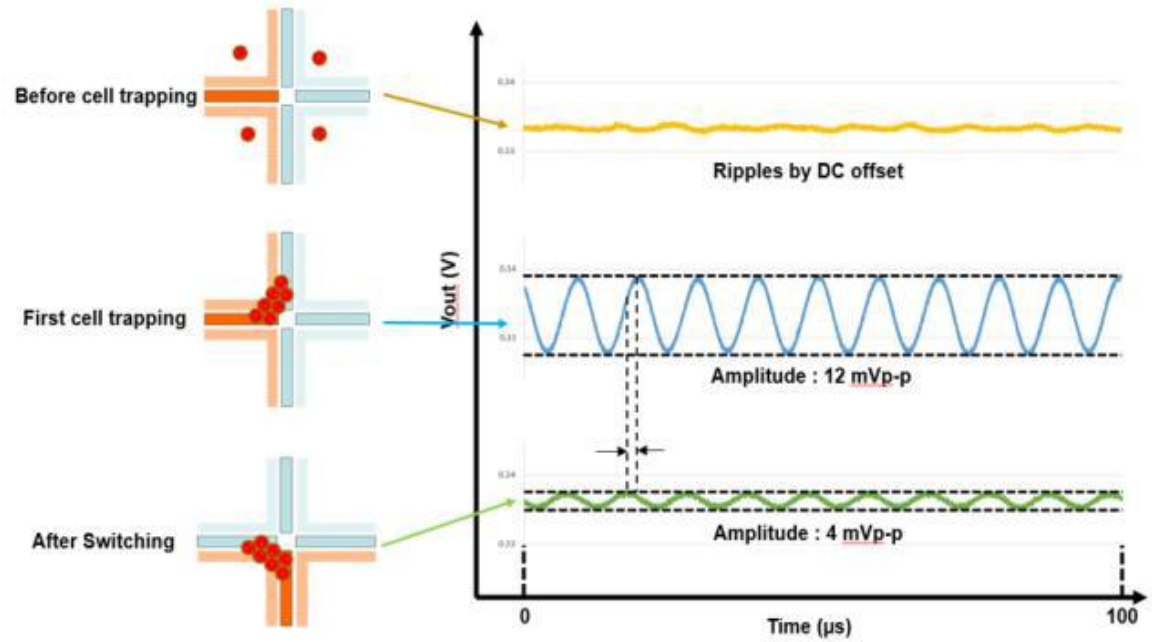

(d)

Figure 4.19. Impedance detection of yeast cells repositioning by switching AC signal to 3D octapole electrodes (a) Yeast cells scattered in the vicinity of the electrode before initial excitation (b) A cluster of cells trapped at the electrode of left side after initial excitation (c) Cell repositioned to the electrode of right side with signal switching (d) Measurement of impedance discrepancy for electrical detection of cell repositioning at 3D octapole DEP structure

4.5. Summary

We presented a DEP based platform for trapping of cells and microorganism in aqueous solution using standard CMOS technology. The proposed platform is based on dielectrophoresis (DEP) which is the force experienced by any dielectric particle including biological entities in non-uniform electrical field. DEP depends on the permittivity of the cells, its size and shape and also the permittivity of the medium. We also discussed the important issues of electrode design using the built-in metal layers of the CMOS process for the most effective trap for single or group of cells. The proposed Lab-on-Chip platform has the ability to trap and detect desired biological entities based on their physical properties and response to DEP forces. Given the need to perform the operation in real-time, in-situ impedance monitoring of the trapping function is also suggested. Simulation results for three electrode designs, and CMOS implementation for one, namely the three-dimensional (3D) octapole electrode geometry have been demonstrated. It also presents an analog front end for impedance monitoring of biological targets as they are repositioned on electrodes due to DEP in real-time. Yeast cells suspended in PBS solution were used as model system for test and evaluation. Since CMOS process offers high throughput and large scale integration, future works will start with multi-site, microarray for DEP manipulation using integrated decoder and MUX so that we would be able to control and program individual DEP site. This approach can open up the

possibility of nano-electronic circuits/devices for computation using conductive nanomaterial such as graphene, metal nanowires or SWNTs. Another work will be a hybridization with precise microfluidics channels for multi-functional application. Also, future efforts will target specific cell types for applications in biology, medicine and life sciences.

Chapter 5

Magnetic nanoparticle based biosensing

5.1. Introduction

During the last decade, a large amount of research work has been carried out on biological application of magnetism such as MRI, and implementation of magnetic biosensors based on molecular recognition processes. In particular, applications of magnetic particles in biomedicine [112], their synthesis [113], functionalization [114] and their detection by magnetic sensors [115] have been highlighted. Through the synergistic interaction of magnetic particles with nanotechnology, new approaches of research and clinical methods have been

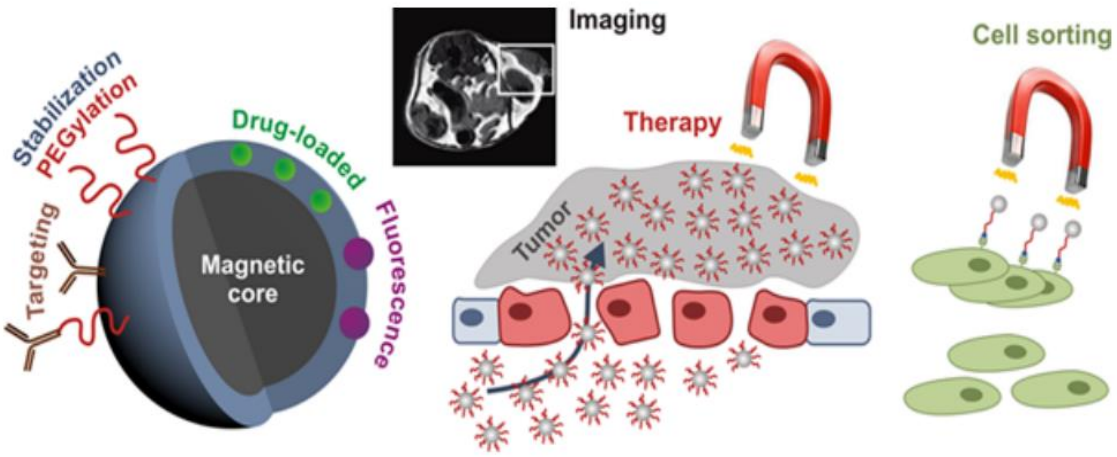

Figure 5.1 Applications of magnetic nanoparticles for biomedicine. [159]

successfully established, such as magnetic actuation [116], hyperthermia treatment [117], targeted drug delivery [118] and the use of magnetic particles as MRI contrast agents [119].

Magnetic nanoparticles (MNPs) offer some attractive possibilities in biomedical applications. First, they have controllable sizes ranging from a few nanometers up to tens of nanometers, which places them at dimensions that are smaller than or comparable to those of a cell (10–100μm), a virus (20–450 nm), a protein (5–50 nm) or a gene (2 nm wide and 10–100 nm long). This means that they can get close to a biological entity of interest. Indeed, they can be coated with biological molecules to make them interact with or bind to a biological entity, thereby providing a controllable methods of tagging or addressing it. Second, the nanoparticles are magnetic, which means that they can be manipulated by an external magnetic field gradient. This remote action combined with the intrinsic

penetrability of magnetic fields into human tissue, allows many applications involving the transport and immobilization of magnetic nanoparticles, or of magnetically labelled biological entities. In this way, they can be made to deliver a package (e.g. an anticancer drug) to a targeted region of the body such as a tumor. Third, the magnetic nanoparticles can be made to resonantly respond to a time-varying magnetic field, with advantageous results related to the transfer of energy from the exciting field to the nanoparticle. For example, the particle can be made to heat up, which leads to their use as hyperthermia agents, delivering toxic amounts of thermal energy to targeted bodies such as tumors; or as chemotherapy and radiotherapy enhancement agents, where a moderate degree of tissue warming results in more effective malignant cell destruction. These, and many other potential applications, are made available in biomedicine as a result of the special physical properties of magnetic nanoparticles.

On the other hand, magnetic nano/micro sized particles can make a valuable contribution towards high sensitivity biosensors. Many types of biosensors employ magnetic nanoparticles (diameter = 5~300 nm) or magnetic particles (diameter = 300~5,000 nm) which have been surface functionalized to recognize specific molecular targets. Generally, three types of biosensors are classified by biosensing principles, magnetic materials, and instrumentation. The first type consists of magnetic relaxation switch assay-sensors, which are based on the effects magnetic particles exert on water proton relaxation rates.

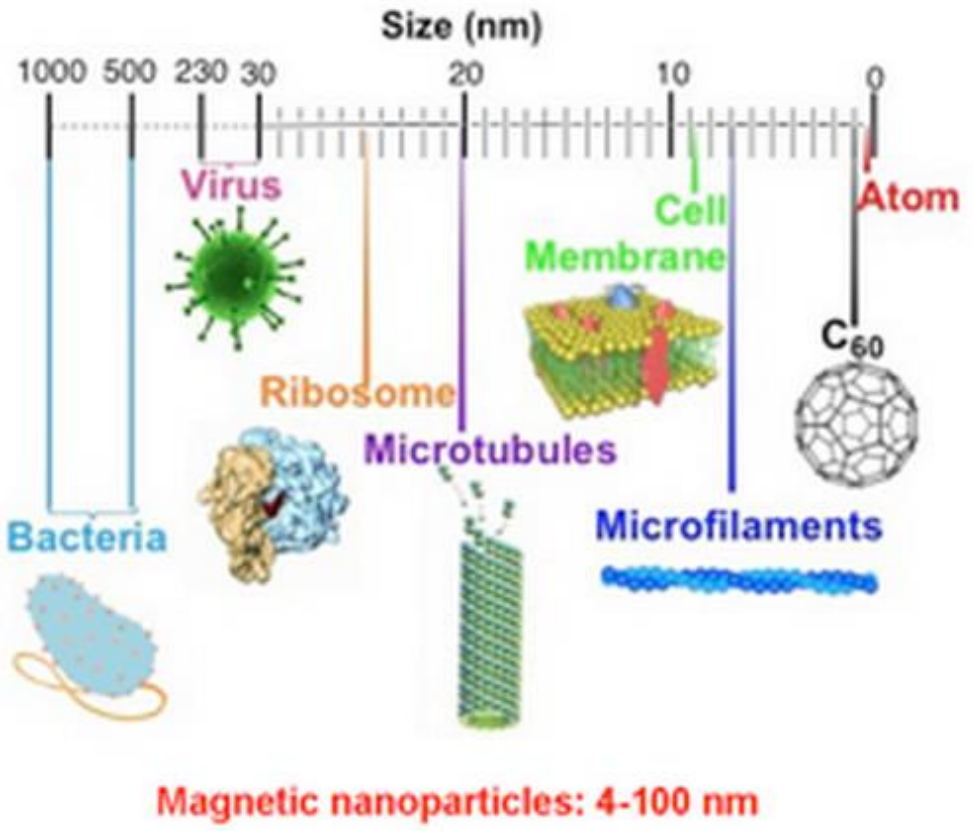

Figure 5.2. Comparison of the sizes of atoms, nanoparticles, and biological entities. [160]

The second type consists of magnetic particle relaxation sensors, which determine the relaxation of the magnetic moment within the magnetic particle. The third type is magnetoresistive sensors, which detect the presence of magnetic particles on the surface of electronic devices that are sensitive to changes in magnetic fields on their surface. We will have more discussion about magnetic particle based biosensors in section 5.3.

5.2. Fundamentals of magnetic nanoparticle

5.2.1 Basics of magnetism

Magnetization

If a magnetic material is placed in a magnetic field of strength $\boldsymbol{H}$ and the individual atomic moments in the material contribute to its overall response, the magnetic induction can be expressed by

$$\boldsymbol{B} = \mu_0(\boldsymbol{H} + \boldsymbol{M}) \qquad (5.1)$$

where μ_0 is the permeability of free space, and the magnetization $\boldsymbol{M} = m/V$ is the magnetic moment per unit volume, where $\boldsymbol{m}$ is the magnetic moment on a volume V of the material. All materials are magnetic to some extent, with their response depending on their atomic structure and temperature. They may be conveniently classified in terms of their volumetric magnetic susceptibility $\boldsymbol{\chi}$, where

$$\boldsymbol{M} = \chi \boldsymbol{H} \qquad (5.2)$$

describes the magnetization induced in a material by $\boldsymbol{H}$. The magnetic susceptibility χ is dimensionless and both $\boldsymbol{M}$ and $\boldsymbol{H}$ are expressed in A/m.

Classification of magnetic materials

Most materials display little magnetism, and even then only in the presence of an applied field; these are classified either as paramagnets, for which $\boldsymbol{\chi}$ falls in

the range 10^{-6} to 10^{-1} and diamagnets, with $\boldsymbol{\chi}$ in the negative range -10^{-6} to -10^{-3}. In contrast, some materials exhibit ordered magnetic states and are magnetic even without a field applied; these materials are classified as ferromagnets, ferrimagnets and antiferromagnets, where the prefix refers to the nature of the coupling interaction between the electrons within the material. This coupling can give rise to large spontaneous magnetizations.

The susceptibility in ordered materials depends not just on temperature, but also on $\boldsymbol{H}$, which gives rise to the characteristic sigmoidal shape of the $\boldsymbol{M}$ – $\boldsymbol{H}$ curve, with $\boldsymbol{M}$ approaching a saturation value at large values of $\boldsymbol{H}$. Furthermore, hysteresis exists at the $\boldsymbol{M}$ – $\boldsymbol{H}$ curve in ferromagnetic and ferrimagnetic materials, which is an irreversibility in the magnetization process. This cause the open $\boldsymbol{M}$ – $\boldsymbol{H}$ curves, called hysteresis loops. The shape of these loops are determined in part by particle size. In large particles of the micron size or more, there is a multi-domain state which leads to a narrow hysteresis loop since it takes relatively little field energy to make the domain walls move, while, in smaller particles, there is a single domain state which leads to a broad hysteresis loop. In single domain state, changes in magnetization occur through the rotation of spins rather than through the motion of domain walls.

At much smaller size particles, as the tens of nanometers or less, superparamagnetism can be seen, where the magnetic moment of the particle as a whole is free to fluctuate in response to thermal energy, while the individual atomic moments maintain their ordered state relative to each other. This leads to

the anhysteretic, but still sigmoidal. Figure 5.3 shows ***M*** **–** ***H*** curve for each class of magnetization.

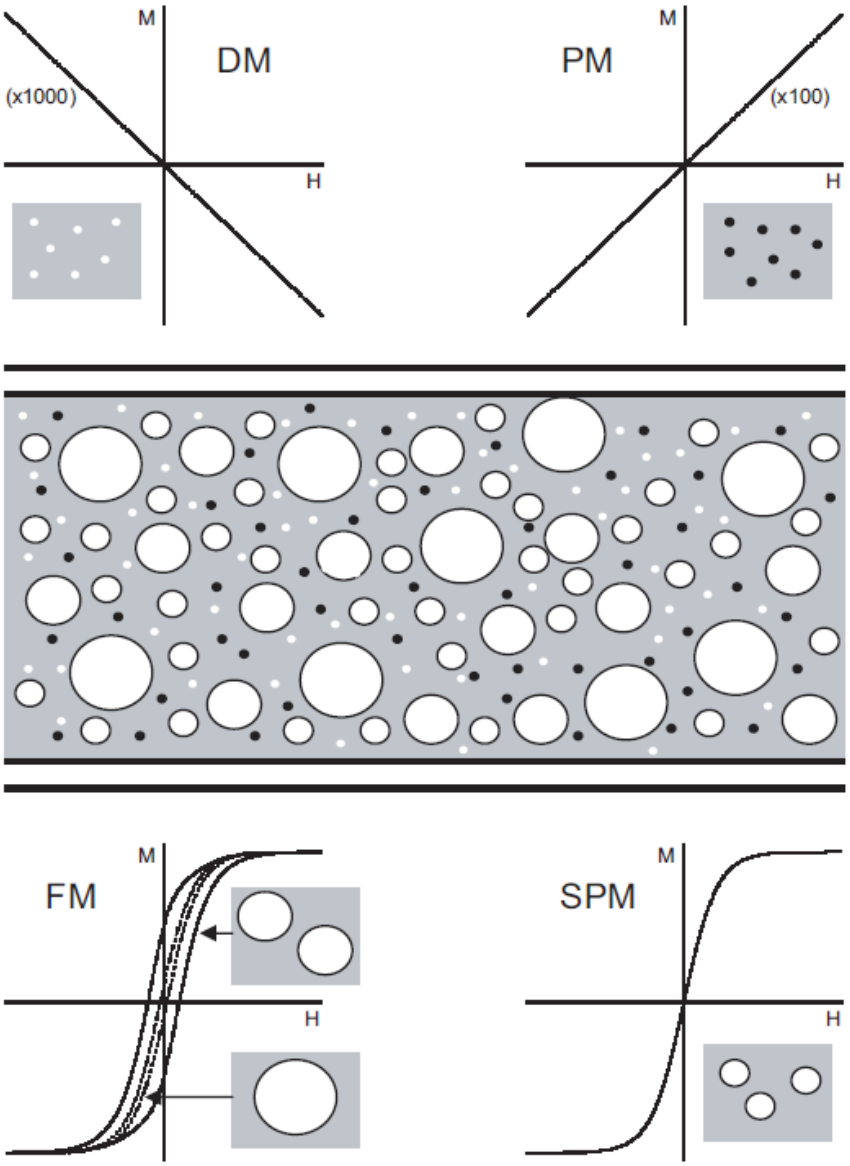

Figure 5.3 Magnetic responses associated with different classes of magnetic material, illustrated for a hypothetical situation in which ferromagnetic particles of a range of sizes from nano scale up to micron scale are injected into a blood vessel. ***M*** **–** ***H*** curves are shown for diamagnetic (DM) and paramagnetic (PM) biomaterials in the blood vessel, and for the ferromagnetic (FM) injected particles, where the response can be either multi-domain (dotted line in FM diagram), single-domain (solid line in FM diagram) or superparamagnetic (SPM), depending on the size of the particle.

5.2.2 Superparamagnetic nanoparticles

When the size of single-domain particles further decreases below a critical diameter, the coercivity, which is the intensity of the applied magnetic field required to eliminate the magnetization of the material, becomes zero and such particles become superparamagnetic. Superparamagnetism is caused by thermal effects. In superparamagnetic particles, thermal fluctuations are strong enough to spontaneously demagnetize a previously saturated assembly; therefore, these particles have zero coercivity and have no hysteresis. Nanoparticles become magnetic in the presence of an external magnet, but revert to a nonmagnetic state when the external magnet is removed. This avoids an 'active' behavior of the particles when there is no applied field. When this property is introduced in the living systems, particles are 'magnetic' only in the presence of an external field, which gives them unique advantage in working in biological environments. There are a number of crystalline materials that exhibit ferromagnetism, among others Fe, Co, or Ni. Since ferrite oxide-magnetite (Fe3O4) is the most magnetic of all the naturally occurring minerals on earth, it is widely used in the form of superparamagnetic nanoparticles for all sorts of biological applications [120,121]. In addition, the particle size provides enough surface area for functionalization which lends itself to applications of such a small dimensions of interest. In Figure 5.4, we can see the comparison of magnetization behavior between ferromagnetic and superparamagnetic nanoparticles (NPs) under an external magnetic field. In the absence of an external field, superparamagnetic NPs will exhibit no net

magnetization due to rapid reversal of the magnetic moment, whereas ferromagnetic NPs will maintain a net magnetization.

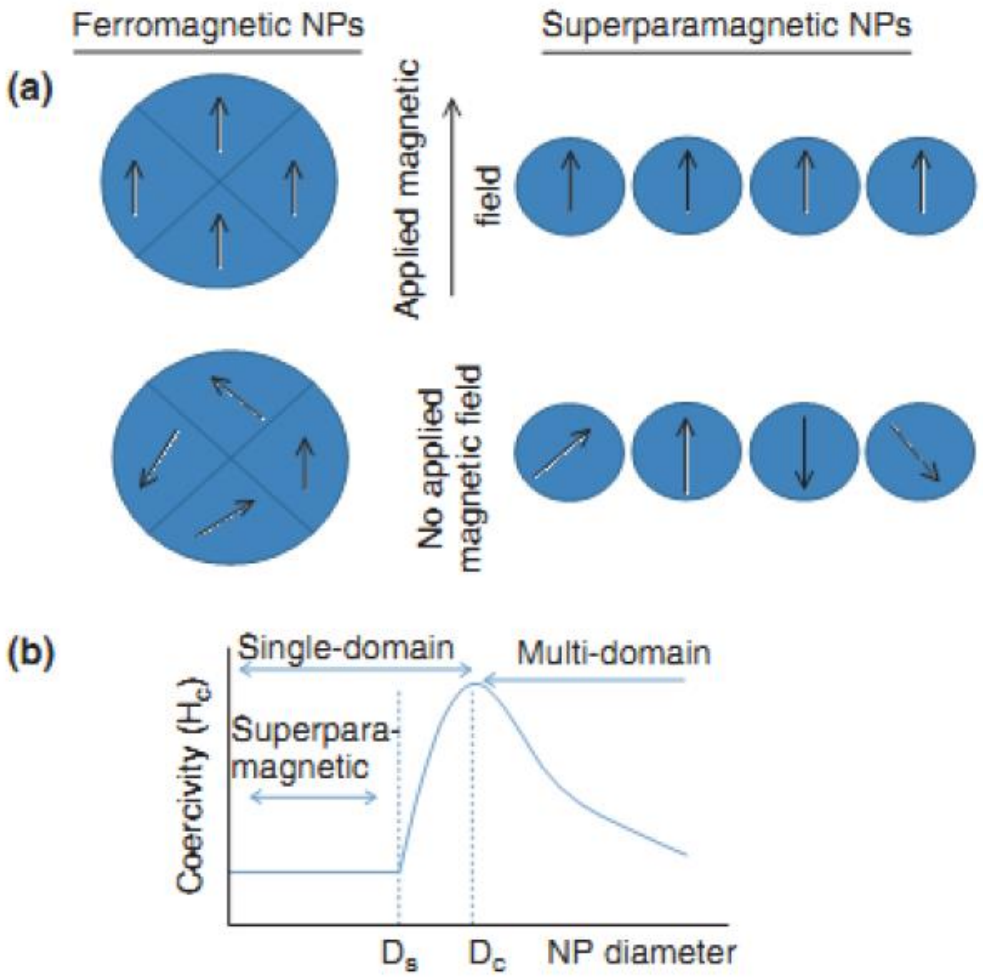

Figure 5.4 Magnetization behavior of ferromagnetic and superparamagnetic nanoparticles (NPs) under an external magnetic field. (a) Magnetic moment alignment of ferromagnetic and superparamagnetic particles with and without the applied field. (b) Relationship between NP size and the magnetic domain structures. Ds and Dc are the 'superparamagnetism' and 'critical' size thresholds.

5.2.3 Forces on magnetic nanoparticles

In order to understand how a magnetic field may be used to manipulate magnetic nanoparticles, we need to recognize that a magnetic field gradient is required to exert a force at a distance where a uniform field gives rise to a torque, but no translational action. The definition of the magnetic force acting on a point-like magnetic dipole m is

$$\boldsymbol{F}_m = (m \cdot \boldsymbol{\nabla})\boldsymbol{B} \tag{5.3}$$

which can be geometrically interpreted as differentiation with respect to the direction of m. In the case of a magnetic nanoparticle suspended in a weakly diamagnetic medium such as water, the total moment on the particle can be written as $m = V_m \boldsymbol{M}$, where V_m is the volume of the particle and $\boldsymbol{M}$ is its volumetric magnetization. This volumetric magnetization is given by $\boldsymbol{M} = \Delta\chi \boldsymbol{H}$, where $\Delta\chi = \chi_m - \chi_w$ is the effective susceptibility of the particle relative to the water. For the case of a dilute suspension of nanoparticles in pure water, we can approximate the overall response of the particles in water by $\boldsymbol{B} = \mu_0 \boldsymbol{H}$, so that equation (5.3) becomes:

$$\boldsymbol{F}_m = \frac{V_m \Delta\chi}{\mu_0} (\boldsymbol{B} \cdot \nabla)\boldsymbol{B} \tag{5.4}$$

If there are no time-varying electric fields or currents in the medium, we can apply the Maxwell equation $\nabla \times \boldsymbol{B} = 0$ and finally obtain a more intuitive form for magnetic force on nanoparticle as equation (5.5).

$$\boldsymbol{F}_m = V_m \Delta\chi \nabla\left(\frac{1}{2}\boldsymbol{B} \cdot \mathbf{H}\right) \qquad (5.5)$$

where the magnetic force is related to the differential of the magnetostatic field energy density, $\frac{1}{2}\boldsymbol{B} \cdot \mathbf{H}$. Thus, if $\Delta\chi$ >0, the magnetic force acts in the direction of steepest ascent of the energy density scalar field. This explains why, for example, when iron filings are brought near the pole of a permanent bar magnet, they are attracted towards that pole.

5.3. Magnetic nanoparticle based biosensors

As mentioned earlier, MNPs are an important source of labels for biosensing due to their strong magnetic properties which are not found in biological systems. Size, modulation of the composition and magnetic properties of the nanoscale materials permit their use in a variety of application for biosensing. The development of MNP based sensing are promising for point of care sensors in variety of bioapplications. We, here, demonstrate three types of biosensors that employ MNP labels with different sensing principles.

5.3.1 Magnetic relaxation switching based biosensors

Superparamagnetic nanoparticles are clinically proven as contrast agents for magnetic resonance imaging (MRI) and widely used in pre-clinical, targeted molecular imaging applications [122]. When the particles are used as targeted

contrast agents, surface-modified nanoparticles for high affinity to biotargets bind specific molecules producing local inhomogeneity in tissues by the applied magnetic field. This inhomogeneity results in decreases in the transverse (T2) relaxation time which means increases the T2 relaxation rate. These, in turn, lead to changes in the contrast of MR images.

The principle of T2 relaxation processes is presented in Figure 5.5, showing the process of transverse relaxation after a 90° radio frequency (RF) pulse is applied at equilibrium. Initially, the transverse magnetization (red arrow) has a maximum amplitude as the population of proton magnetic moments (spins) rotate in phase. The amplitude of the net transverse magnetization (and therefore the detected signal) decays as the proton magnetic moments move out of phase with one another (shown by the small black arrows). The resultant decaying signal is known as the Free Induction Decay (FID). The overall term for the observed loss of phase coherence (de-phasing) is T2* relaxation, which combines the effect of T2 relaxation and additional de-phasing caused by local variations (inhomogeneity) in the applied magnetic field. T2 relaxation is the result of spin-spin interactions and due to the random nature of molecular motion, this process is irreversible. T2* relaxation accounts for the more rapid decay of the FID signal, however the additional decay caused by field inhomogeneity can be reversed by the application of a 180° refocusing pulse. Both T2 and T2* are exponential processes with times constants T2 and T2* respectively. This is the time at which the magnetization has decayed to 37% of its initial value immediately after the 90° RF pulse.

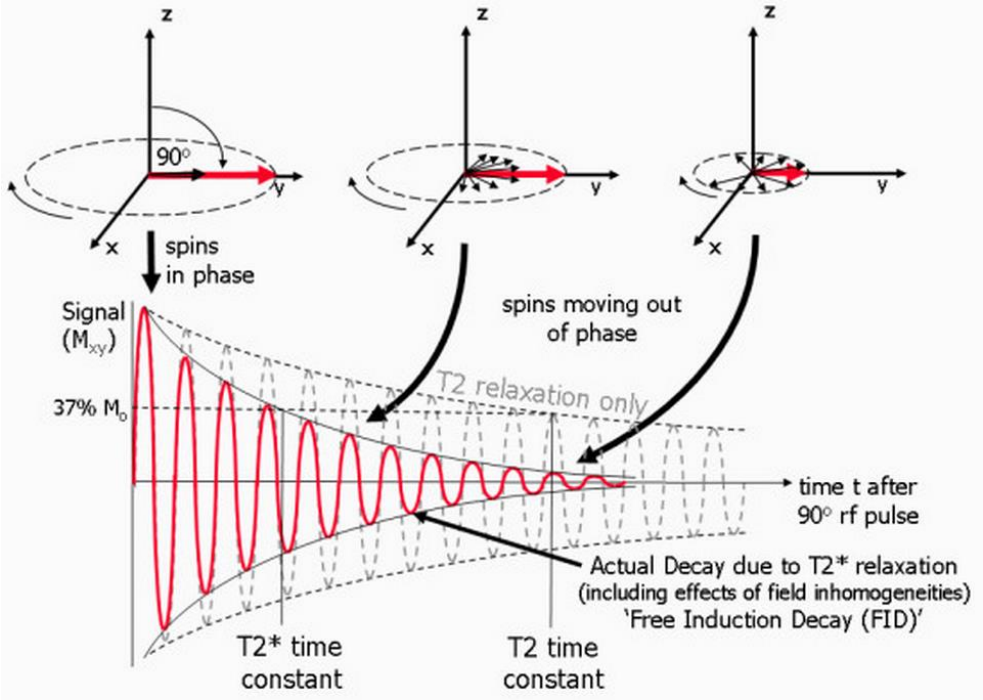

Figure 5.5 Transverse (T2 and T2*) relaxation processes [123]

Basically, T2 relaxation based biosensing techniques detect the change in T2 relaxation time caused by the discrepancy between the dispersed and aggregated states of magnetic NPs in water. The aggregation of NPs and the size range of the resulting aggregates depend on the type of analyte and analyte concentration. Due to the reversal of the dispersed and aggregated states for NPs by some factors such as temperature, pH, and a high concentration of competing analytes, those are referred as Magnetic Relaxation Switches (MRSws) [124]. MRSws are homogeneous particle aggregation/disaggregation-based assays similar to aggregation assays using Latex particles, red blood cell hemagglutination, and antibody reactions with proteins (nephelometry). Figure 5.6 illustrates a nuclear

magnetic resonance (NMR) for biosensing, which is one of T2 relaxation based sensing techniques [125].

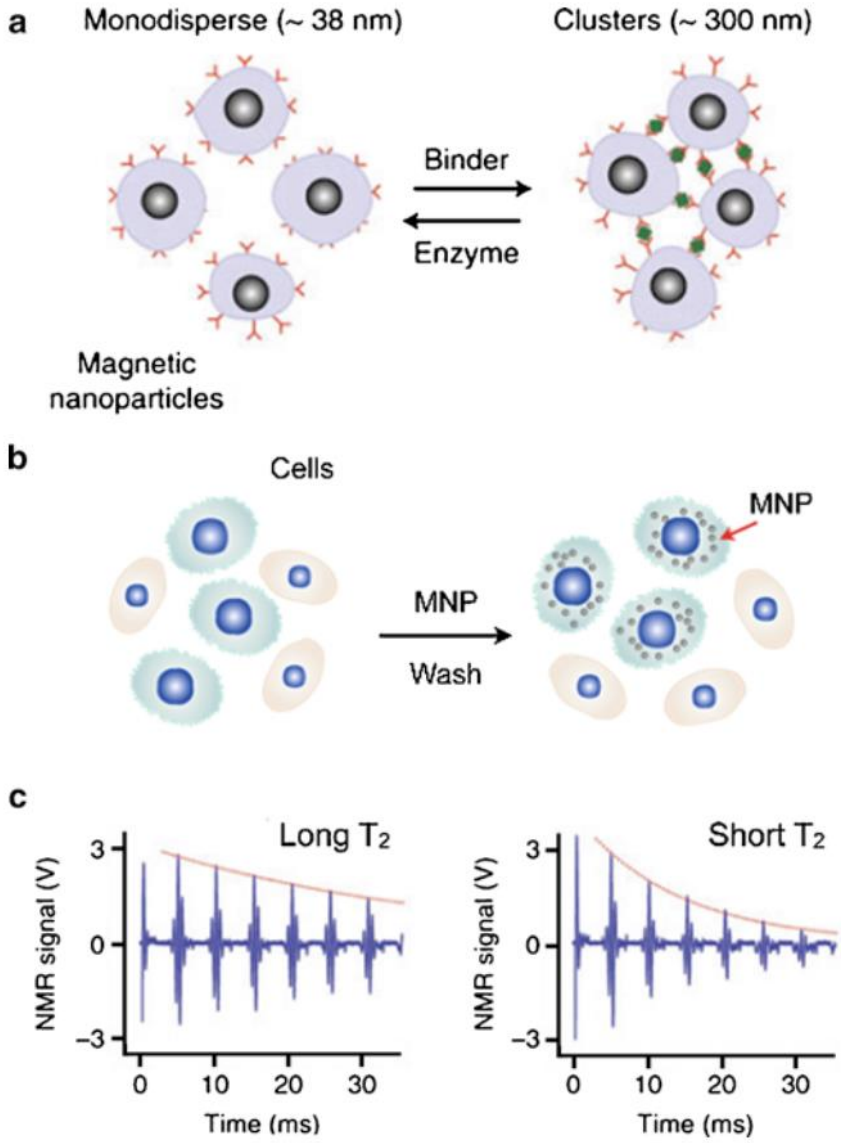

Figure 5.6 NMR sensing principles. (a) Magnetic relaxation switching (MRSw) involves the assembly of MNP into clusters or disassembly of preformed clusters by the action of a target biomolecule. Clustered MNP dephase the nuclear spins of neighboring water molecules more efficiently than evenly dispersed MNP, shortening the bulk transverse relaxation time (T2). (b) Tagging cells with MNP imparts a magnetic moment that is proportional to the number of nanoparticles bound. Following washing procedures to remove unbound MNP, the magnetic moment can be measured as a decrease in T2 relaxation time. (c) Representative NMR output depicting the shortening of T2 relaxation time that accompanies MNP clustering (MRSw) or cellular tagging.

5.3.2 Magnetic particle relaxation based biosensors

The relaxation of the magnetic moments within magnetic particles have been used as a basis for magnetic particle based sensing. The sensing scheme is based on the detection of dynamic magnetic properties [122]. Tiny magnetic particles in aqueous solution, with magnetic moments aligned by an applied magnetic field, employ two relaxation mechanisms when magnetic field is turned off, which are Brownian and Néel relaxation. When the magnetic anisotropy energy is high enough to block the magnetization inside the nanoparticle, then the relaxation occurs due to rotational diffusion (Brownian). However, if the magnetization is unblocked, then the particles are superparamagnetic and the magnetization relaxes internally (Néel). Generally, the effective relaxation is a combination of both relaxation mechanisms.

The dominant relaxation of the two mechanisms depends on the particle size. Néel relaxation is the dominant mechanism for particles less than 10–20 nm while the Brownian mechanism is dominant for larger particle diameters. However, when the particle diameter increases further, the magnetization ceases to be single domain and a multi-domain state develops to reduce the magnetostatic energy. In this case, the magnetic relaxation no longer reflects the Brownian motion, but instead can be dominated by internal changes of the magnetization, i.e., domain-wall motion. Therefore, there is an upper limit on the magnetic particle size for the relaxation based sensing. Furthermore, beyond a certain limit the particles are not easily suspended in a liquid. In fact, the use of

small magnetic nanoparticles may be beneficial in general, since they may avoid structural change of the biological entities or blockage of the biological binding interactions.

Superconducting quantum interference device (SQUID) has been used to detect biological binding activity through the relatively slow magnetic Néel relaxation upon immobilization of the biomagnetic particles [126]. AC susceptibility measurements based on Brownian relaxation has been introduced [127], which measure the change in the Brownian relaxation of the beads as analyte molecules bind and increase the bead's hydrodynamic radius. We will propose compact AC susceptometer and discuss more details about Brownian relaxation based magnetic sensing approach in chapter 6.

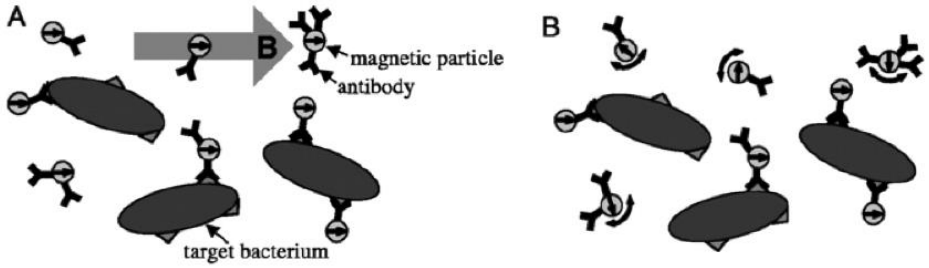

Figure 5.7 SQUID-based homogeneous magnetic relaxation detector (A) A pulse-form magnetic field orients the magnetic moments of NPs. (B) after the field pulse is over, Brownian motion randomizes the magnetic moments of unbound NPs. However, the Brownian rotations of NPs bound to the bacteria are restricted. The bound NPs undergo Néel relaxation for reorientation of the magnetic moments. The SQUID detects the slower Néel relaxation for the bound NPs [126].

5.3.3 Magnetoresistance based biosensors

Magnetoresistance (MR) is the property of a material to change the value of its electrical resistance when an external magnetic field is applied to it. There is a variety of effects that can be called magnetoresistance, some of them occurring in bulk non-magnetic metals and semiconductors, others in magnetic metals such as negative magnetoresistance in ferromagnets or anisotropic magnetoresistance (AMR). Since the first magnetoresistive effect was discovered by Lord Kelvin in 1851, nowadays, it is known that magnetic field can change resistance by orders of magnitude in some MR system.

Magnetoresistive biosensors are based on the binding of magnetic particles to a surface of a magnetoresistive material acting biosensor. The magnetic fields of the particles alter the magnetic fields in the MR sensor which result in electrical current changes within the sensor. There are two mechanisms through which magnetic particles bind to the sensor surface, which are direct labeling and indirect labeling named a sandwich type binding.

Magnetic probes bind to the surface functionality on the surface in direct labeling by using protein-biotin interaction or complementary DNA sequence recognition. Figure 5.8 shows a schematic illustrations of a magnetic array GMR spin valve sensor using direct labelling [128]. A single magnetic nanoparticle label is directly bound to the sensor through hybridized probe and target DNAs in the biologically active area. The aluminum leads define the electrically active area where an electrical sense current passes in the SV.

Indirect labeling uses the principle of sandwich immunoassay in enzyme-linked immunosorbent assay (ELISA). For example, antibodies that bind to the target protein are immobilized on the surface. After treatment of the surface with a sample solution containing the target proteins, second antibodies that are biotinylated are added to the system. Finally a high affinity protein for biotin (e.g. Streptavidin), coated magnetic particles are applied for tagging the biotinylated antibodies. Giant magnetoresistance (GMR) spin valve (SV) or magnetic tunnel junction (MTJ) sensors have been successfully used to detect magnetic particles. Sensors are composed of multiple layers of ferromagnetic materials. A biologically active molecule can be deposited on an Au layer or SiO2 layer to obtain a surface for the attachment of biomolecules. An example of a giant magnetoresistive (GMR) sensor for an ELISA-type protein assay is presented in Figure 5.9 [129].

Earlier applications for magnetoresistive biosensing used relatively large magnetic particles, with diameters between 0.1 and 3 mm [130]. Micrometer sized particles have the advantages of facile observation under light microscope and a higher particle-based magnetic moment that permits detection very small numbers of particles. However, superparamagnetic NPs have recently replaced the larger particles because the NPs are stable in suspension and are less prone to particle clustering in an applied magnetic field [131, 132]. Streptavidin coated MPs were applied to spin valve sensors in the protein marker detection at 27 pg/mL level of sensitivity [133].

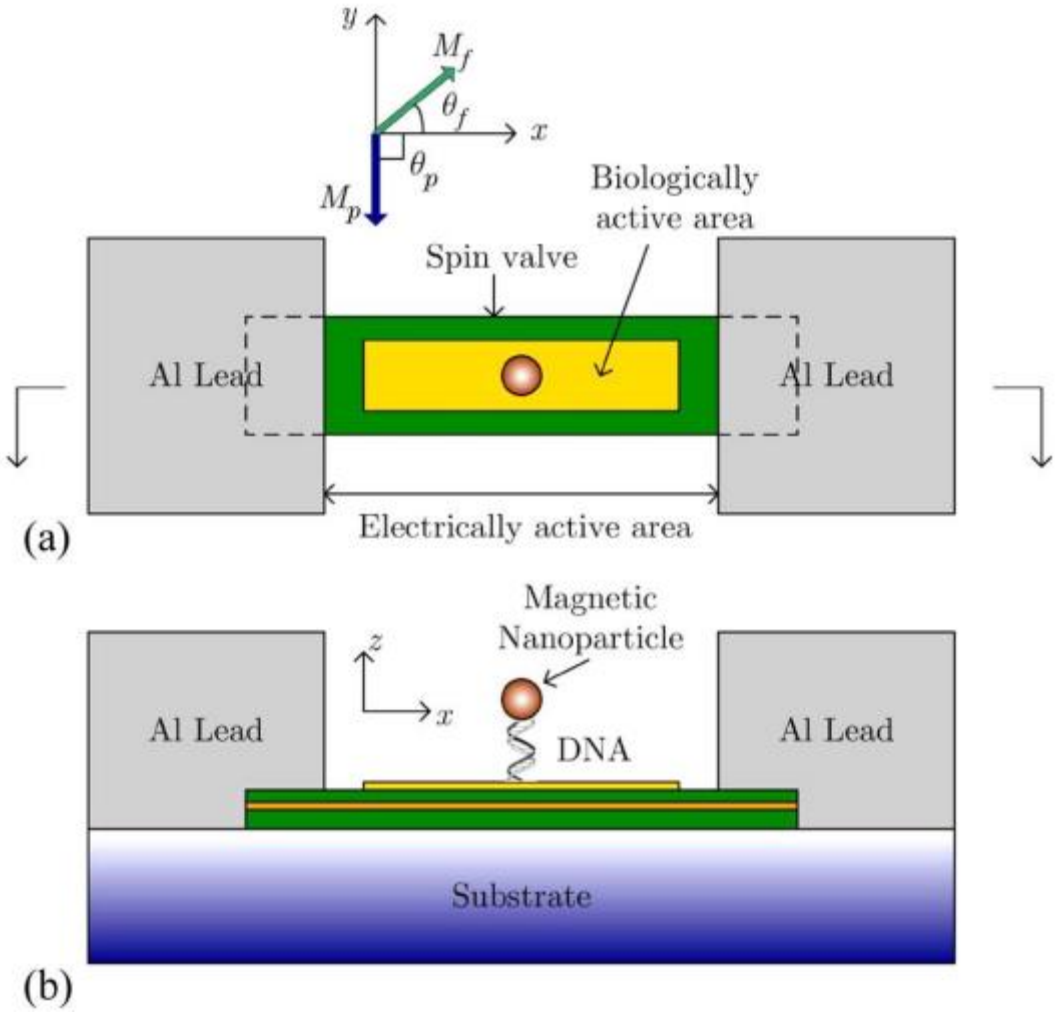

Figure 5.8 Schematic illustrations of (a) the top view of a MagArray SV sensor and (b) its cross section.

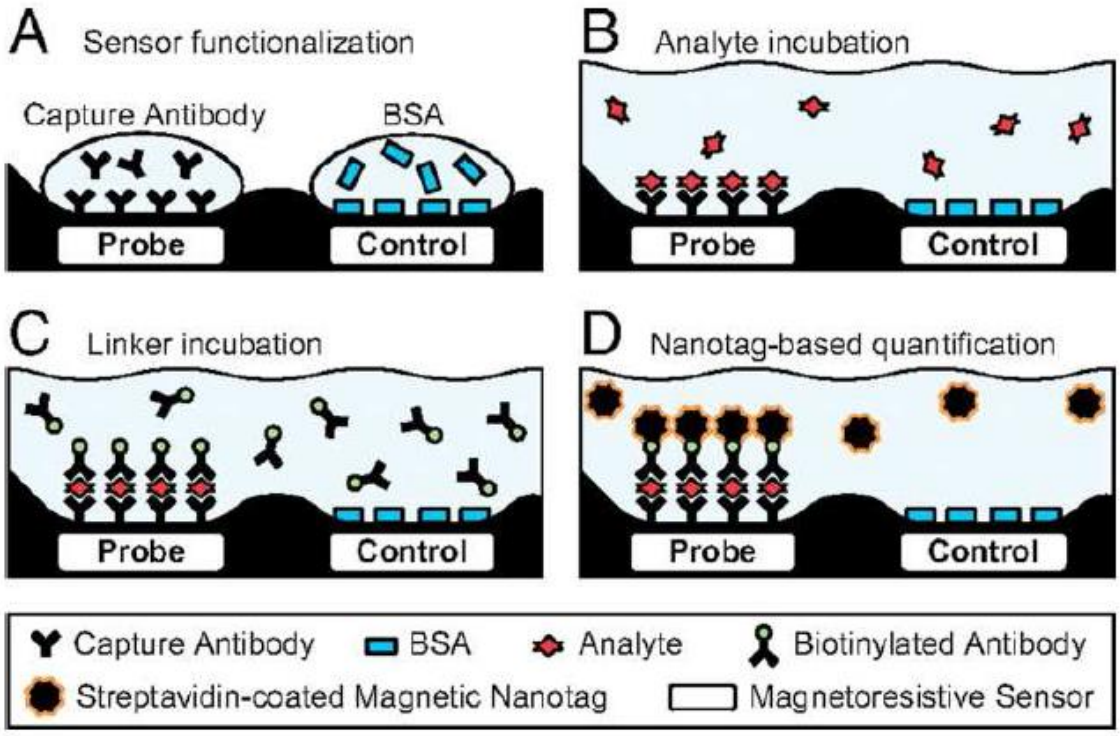

Figure 5.9 Schematic representation of a giant magnetoresistive (GMR) sensor for an ELISA-type protein assay. (A) The probe surface was functionalized with a specific antibody, while the control surface was passivated with BSA. (B) A sample solution was added for a specific binding of analyte proteins to the probe surface. (C) A biotinylated antibody bound to the surface-immobilized analytes. (D) Finally streptavidin-coated NPs were added for tagging the probe surface by biotin-streptavidin interaction. GMR signals were detected for sensing the presence of analytes on the surface.

Chapter 6

Brownian relaxation based biosensing using AC magnetic susceptometer

6.1. Introduction

Due to the relative simplicity of sample preparation, ease of processing and inherent biocompatibility, magnetic nanoparticles (MNPs) are increasingly of great interest in biotechnology and biomedicine as alternatives to conventional radioisotopes or fluorescent materials [134, 135]. The development of bio-conjugated MNPs allows various opportunities for the application of MNPs for biomedical diagnostics [136, 137].

Several sensing schemes using the magnetic stray field of MNPs bound to targets have been studied by means of magnetoresistance [138], Hall effect [139] or superconducting quantum interference devices [140]. However, many

established devices and techniques require extreme conditions such as high magnetic fields and/or low temperature and are also time consuming. An alternative method to detect the binding of biomolecules such as protein to the MNPs is via measurement of the AC magnetic susceptibility of the nanoparticles based on Brownian relaxation. AC magnetic susceptometry is a precise detection technique that capitalizes on the diffusive properties of MNPs in solution [141, 142] and is appropriate for point-of-care diagnostics with potential for chip implementation [143].

The use of AC susceptometry for the detection of biomolecules using tagged MNPs was initially described theoretically by Connolly and St Pierre [144]. Magneto-optical measurement [145, 146] and fluxgate relaxometry [147, 148] have recently been proposed to measure Brownian relaxation of MNPs to acquire AC magnetic susceptibility as a function of frequency. Although previous studies have shown good performance with outstanding sensitivity, experiments have been done for only single-sized MNPs with bulky conventional instruments. Our focus is on achieving multiplexed biosensing for the mixture of differently sized MNPs utilizing a compact, room temperature, low cost, low power AC susceptometer. The susceptometer and the proposed approach are scalable for LoC application using planar microcoils and microfluidics.

6.2. Theory of magnetic detection using Brownian relaxation

The principle of a Brownian relaxation detection scheme uses the random rotational motion of magnetically tagged sensors, determined via measurement of collective magnetic susceptibility as a function of the frequency of the applied magnetic field [149]. When the excitation frequency is close to the rotational motion frequency of the magnetically labeled sensor, a large increase in the loss component of the complex magnetic susceptibility occurs. This is observed as a peak frequency of the imaginary component of the complex magnetic susceptibility (90◦ out-of-phase: χ''). The application of this technique for biological diagnostics relies on a shift in the peak frequency of χ''upon target binding to labeled MNPs. Figure 6.1 depicts mechanism of Brownian magnetic sensing for spherical geometry. If a target molecule then binds to a specified receptor on the sensor, the hydrodynamic size of the sensor is effectively increased and there is a readily measurable shift of the frequency maximum to lower values with cubic dependence on hydrodynamic radius. The real (χ') and imaginary (χ'') components of the complex magnetic susceptibility are described by the following relations [149]:

$$\chi(\omega) = \chi'(\omega) - j\chi''(\omega) \qquad (6.1)$$

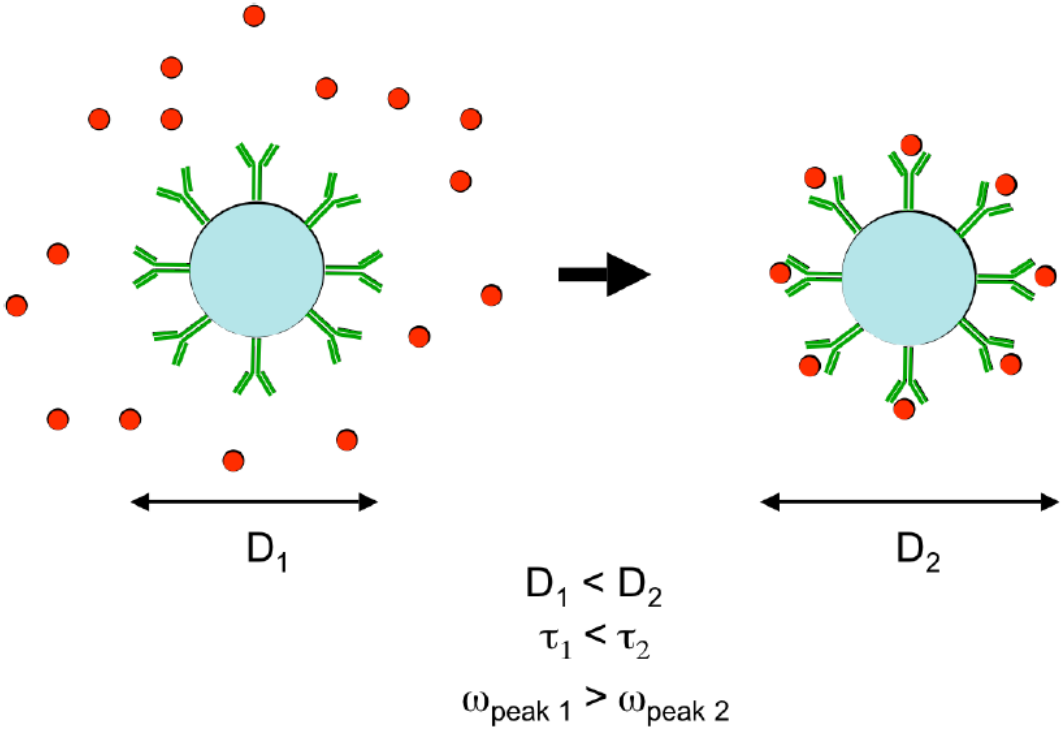

Figure 6.1. Mechanism of Brownian magnetic sensing for spherical geometry. (A) Upon target binding, the hydrodynamic diameter of the antibody-magnet conjugate is increased and diffusion slows. This results in a detectable reduction in the peak frequency of the imaginary (out of phase or loss) component of the magnetic susceptibility. (B) This shift is proportional to the cube of the radius of a sphere or length of a rod, so that very small changes in diameter/length are detectable. Electronic detection of these changes provides the basis of a new diagnostic technique for the detection of biomolecules in solution [150].

$$\chi'(\omega) = \frac{\chi_0}{[1+(\omega\tau_r)^2]} \tag{6.2}$$

$$\chi''(\omega) = \frac{\chi_0\omega\tau_r}{[1+(\omega\tau_r)^2]} \tag{6.3}$$

where χ_0 is the static magnetic susceptibility, ω is the frequency and τ_r is the effective relaxation time. For MNPs in solution in an AC magnetic field, this relaxation time is primarily dependent on Brownian motion. Thus, the effective relaxation time for monodisperse MNPs can be approximated by the Brownian diffusion time (τ_r) [142]:

$$\tau_r = \frac{4\pi\eta r^3}{k_B T} \tag{6.4}$$

where η is the fluid viscosity, r is the hydrodynamic radius of magnetic nanoparticles, k_B is Boltzmann's constant and T is the absolute temperature. It follows that χ'' is maximum at $\omega\tau_r = 1$ and $\omega_{max} = 1/\tau_r$. Since τ_r is a function of r^3, the peak frequency of imaginary susceptibility will decrease proportional to the hydrodynamic radius with cubic dependence. Unlike other ELISA techniques that require tight binding for detection, even dynamic binding should perturb the relaxation of sensor particles, resulting in a detectable signature. Low inherent susceptibility in most biological samples should facilitate low background detection even in unpurified samples. Binding events to small and large organisms, large molecules (e.g. DNA) and other macromolecular aggregates can

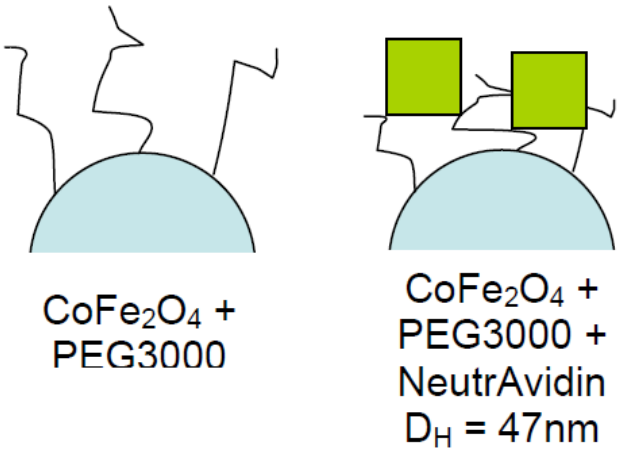

(a)

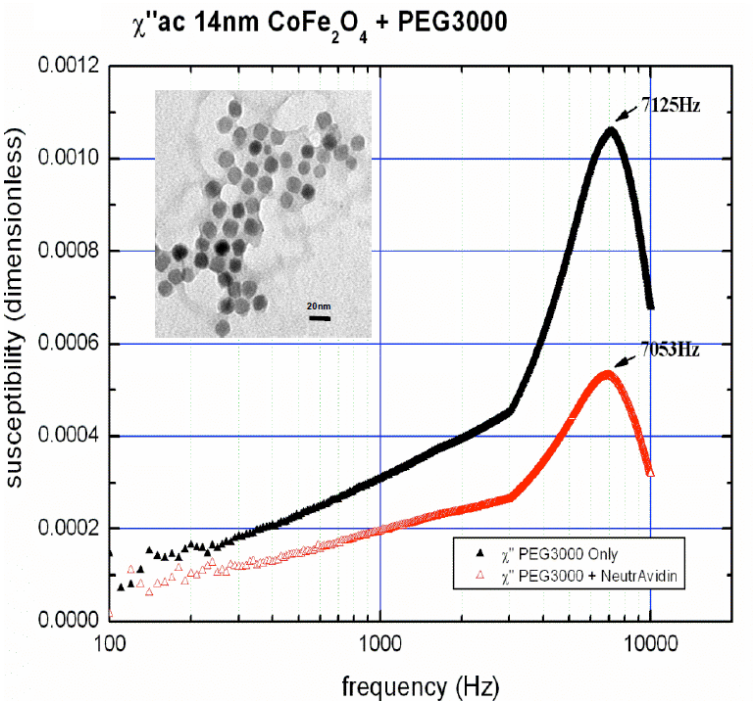

(b)

Figure 6.2. Measurement of frequency peaks in the imaginary component of the complex AC magnetic susceptibility (a) The surface modification scheme of PEG + Neutravidin coated CoFe2O4 magnetic particle. Average hydrodynamic diameters was measured by dynamic light scattering at room temperature in deionized water. (b) Measurement of AC susceptibility for CoFe2O4 nanoparticles using conventional MagLab susceptometer. The complex magnetic susceptibility was measured using a 5Oe field from 100 Hz ~ 10 kHz [150].

be detected using the proposed scheme. Figure 6.2 shows a measurement of sharp, highly differentiable peaks in the imaginary component of the complex AC magnetic susceptibility are shown for polyethylene glycol (PEG) and PEG + Neutravidin coated CoFe2O4 magnetic particles. Inset shows TEM image of the Neutravidin coated particles. The narrow size distribution and regular shape of the magnets contribute to remarkable peak sharpness.

The AC magnetic susceptibility can be measured with balanced coils configuration for the detection of the magnetic nanoparticles shown Figure 6.3(a) [161]. The AC susceptibility system has primarily three coils, which are the pickup coil for the detection of the magnetic signal, the field coil for applying the excitation field to the nanoparticles, and the compensation coil to cancel out offset. The pickup coil consisted of two identical coils, which are separated apart by a specific distance and the direction of the winding of the two coils are opposite each other. The field coil can be big single coil or made of two identical coils, which were mounted just outside of the pickup coils. Compensation coil is desirable to compensate unmatched magnetization by inaccurate positioning of magnetic sample. Due to the excitation field, the magnetic particles are magnetized, and the resulting signal is detected with the pickup coil. The voltage across the pickup coil can be measured with lock-in-amplifier for the case of the sinusoidal signal. From the measured voltage, we can extract the changes of in-phase and out-of phase susceptibility of inserted magnetic samples in terms of applied signal frequency as equation (A.33).

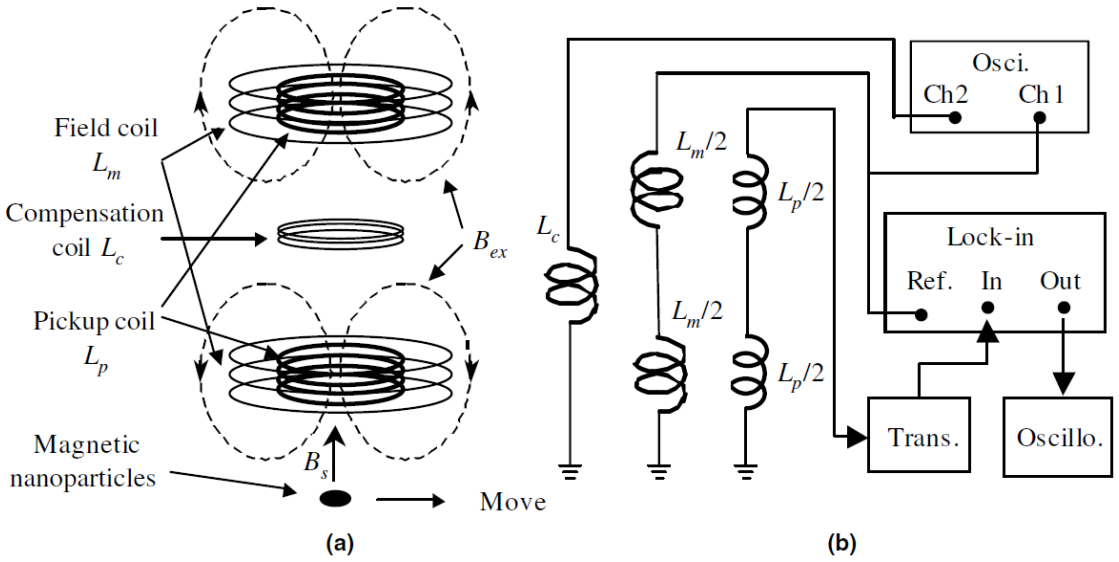

Figure 6.3 AC susceptibility measurement system for the detection of the magnetic nanoparticles. (a) Schematic diagram of coils. (b) Equivalent circuit of the system.

Figure 6.4 is an example of conventional AC susceptometer, which provides operation at cryogenic condition and even stronger magnetic field by giant coils so that it allows much higher sensitivity. However, commercial AC susceptometer is not suitable for portable application such as clinical point of care devices.

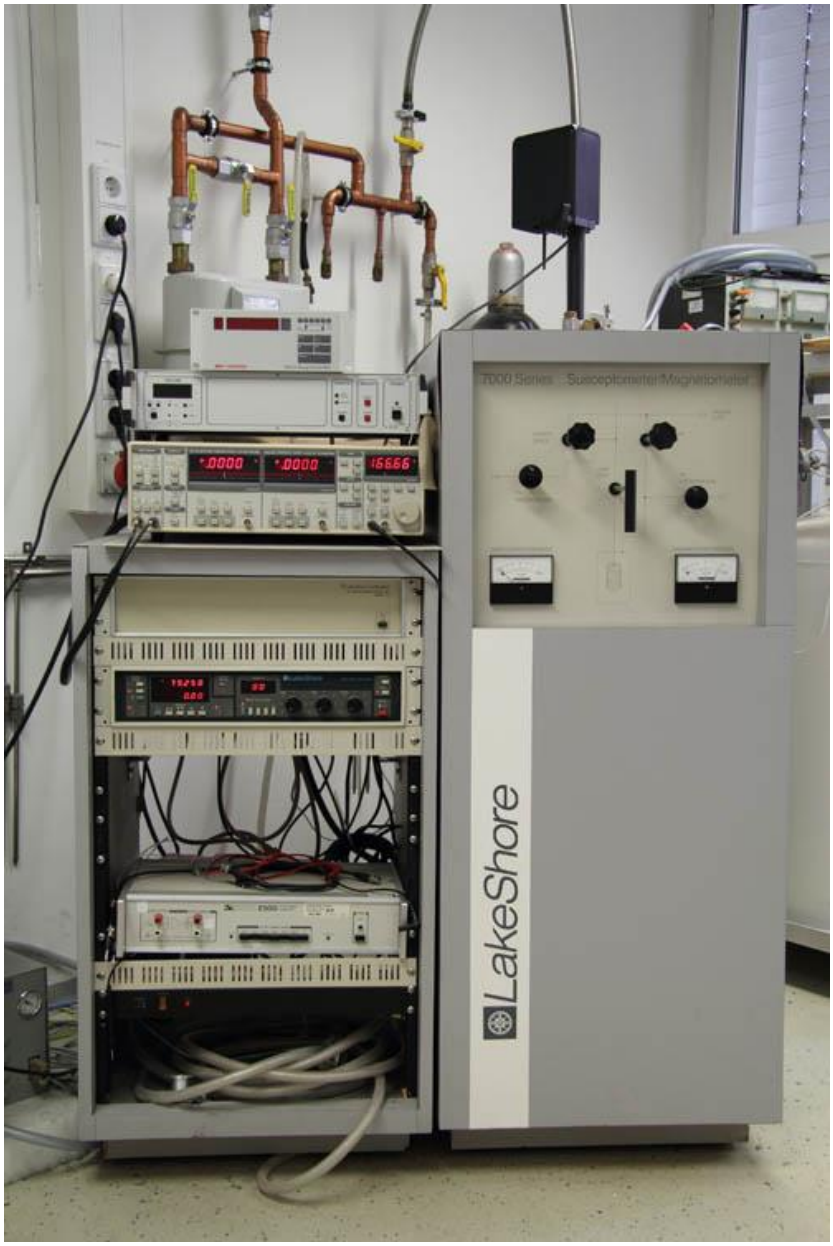

Figure 6.4 Conventional AC Susceptometer, Lake Shore, Model 7000

6.3. Compact AC magnetic susceptometer for Brownian sensing

6.3.1 Numerical analysis of sensitivity

In most AC susceptometers, especially commercially available, the typical coil assembly consists of a vertical long magnetizing solenoid and a pair of short measuring with compensating coils, which are identical and connected in series opposition and coaxially symmetrically placed upper and down within (or surrounding) the solenoid. Thus, when feeding AC current in the primary solenoid, the induced voltage in the secondary coils is practically zero when the sample is absent, and if the sample is placed inside the measuring coil, the induced voltage will be proportional to the sample moment. Figure A.1, in appendix section, illustrates axial cross-sectional view of typical solenoid coils for AC susceptometer.

The design of coil assembly is very critical in implementing AC susceptometer because the sensitivity of the detection system mostly depends on performance of the coils. For point of care medical application, low volume and low concentration biological samples generate very weak signal (usually less than tens of μV) to sense, even if high magnetization on the biosamples is allowed. Therefore, high sensitivity design of coils system is essential and accurate design of symmetric coil configuration is necessary to eliminate offset.

The derivation of sensitivity for AC susceptometer with differential solenoid coil configuration is shown in Appendix 1. From the calculation, we can infer which/how design parameters affect sensitivity of the AC susceptometer. The sensitivity of AC susceptometer first is related to the output differential voltage measured across the sensing coils. For a given susceptibility χ of the test sample, the measured voltage sensitivity is determined by equation (A.30) for both in-phase and out-of-phase output voltage signal. From the equation (A.30), the output voltage can be enhanced by increasing the applied AC current magnitude, frequency, number of coil turns with fixed length, and sample volume. In standpoint of coil dimension, if we are able to decrease radius of sensing coil, reducing length of sensing coil using microfabrication techniques, the sensitivity would be considerably improved theoretically as shown in Figure 6.5. However, micro-fabricated coils have an intrinsic drawback of very low Q factor less than 5 in low frequency we are interested in for Brownian relaxation based biosensing (~10 KHz). This means relatively high resistance compared to inductance, which create a significant resistive noise at the devices. Some studies about microcoil design has shown that when trying to increase inductance of coils for higher magnetic induction, the resistance increases much faster than the inductance [151]. Hence, many AC susceptometers operates in low temperature to reduce the resistance of coils and lock-in-amplifier is also employed in the measurement system to improve sensitivity.

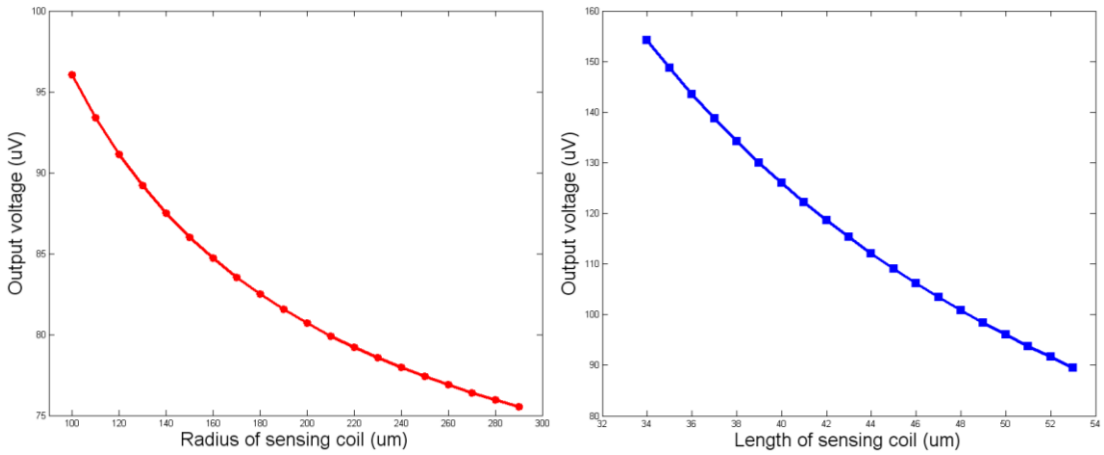

(a) (b)

Figure 6.5 Sensitivity of differential solenoid AC susceptometer in terms of (a) radius of sensing coil with fixed length of sensing coils and (b) length of sensing coil with radius of sensing coils. All other parameters have been fixed such as sample volume, frequency, applied current, number of turns of coils.

6.3.2 Design of compact AC magnetic susceptometer

Prior work on utilizing magnetic detection of Brownian relaxation has been limited to single-sized magnetic nanoparticles using bulky conventional instruments. Here, we propose a platform for simultaneous multiplexed detection of multiple magnetic nanoparticles utilizing a compact low power AC susceptometer. The proposed compact AC magnetic susceptometer consists of a high impedance AC current source (6221; Keithley, USA), precise millimeter-sized differential sensing coils and a lock-in amplifier (LIA: 5210; EG&G, UK) to extract the in-phase and out-of-phase components of minute voltage signals from the sensing coil output as shown in Figure 6.6. For amplifying the weak signal from the secondary coil and rejecting environmental noise, a low noise amplifier

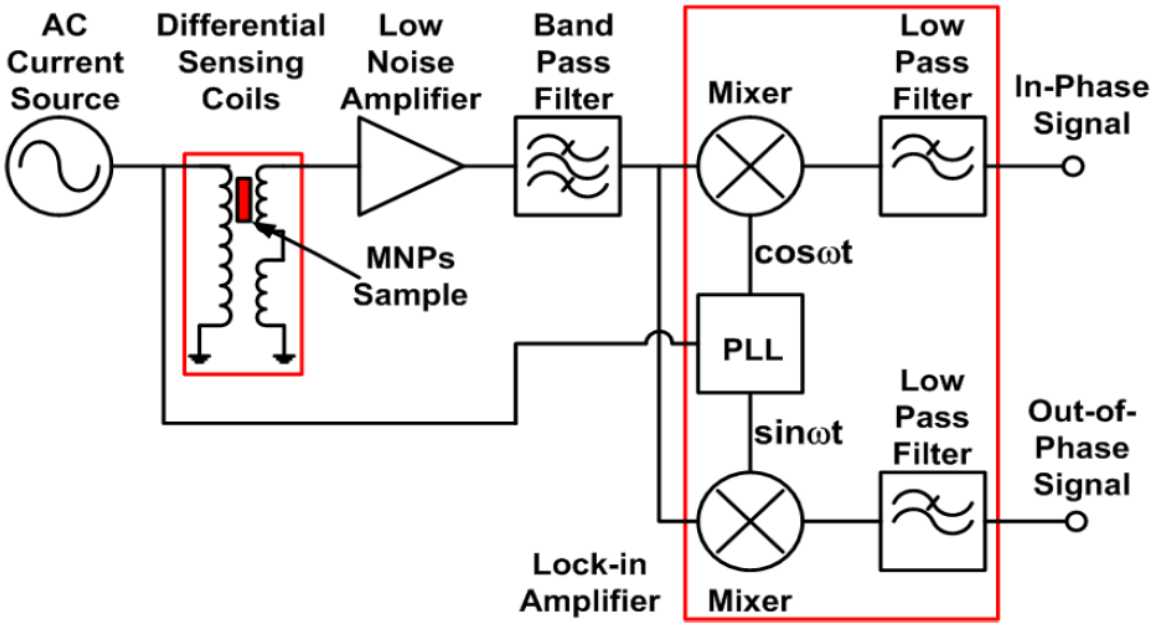

Figure 6.6 Block diagram of proposed compact AC magnetic susceptometer

(OPA124; TI, USA) and band pass filter (MAX268; Maxim, USA) implemented on a printed circuit board were used before a lock-in amplifier. The entire system can be miniaturized in future versions using complementary metal oxide semiconductor (CMOS) technology. The differential sensing coil system has two cylindrical coil pairs; an excitation coil and two identical sensing coils. Differential arrangement provides noise immunity and sensitive measurement of the induced voltage in secondary coils, which originates from the magnetization of the MNPs. Further details regarding our coils are given in Table 3. Offset voltage compensation was achieved by sliding the sensing coils inside the excitation coil. Magnetic nanoparticles were loaded in a capsule with a volume of 80 μl and then the capsule was inserted into the core of one of the secondary coils. The other secondary coil is air core with no sample. All measurements are carried out at

room temperature. AC sinusoidal current from the current source was applied to the excitation coil and the phase of the reference signal was adjusted in the LIA to maximize the imaginary component of the detected signal. The measurement process has been automated and performed by NI LabView. Frequency was swept between 10 Hz and 10 kHz in equal steps. One frequency scan was acquired in about 30 min and can be reduced with better board design and high-speed data acquisition. Since the detected signal from the LIA is of the order of microvolts and is sensitive to noisy environments, an averaging technique has been employed in this measurement.

Table 3. AC magnetic susceptometer coil design

	Excitation coil	Sensing coil 1	Sensing coil 2
No. of turns	2000	1000	1000
Diameter (mm)	15.88	9.53	9.53
Length (mm)	190.55	57.25	57.25
Distance between Sen. 1 and Sen. 2 (mm)		41.28	
Wire diameter (mm)	0.20	0.20	0.20

6.4. Experimental Results

Magnetic detection of Brownian motion of MNPs based on the measurement of complex AC susceptibility in aqueous solution depends on several critical parameters such as effective hydrodynamic size of MNPs, concentration of MNPs, temperature and applied magnetic field. We first report the parameter analysis of AC susceptibility for Brownian relaxation of MNPs utilizing our compact AC susceptometer. We carried out all measurements under room temperature and identical conditions except for the parameter to be analyzed using our handheld AC susceptometer. Although the present detection sensitivity is limited due to coil dimensions and amplifier sensitivity, the study provides a useful guide to further improve the detection limit to 1 μg ml^{-1} with just 10 μT field excitation in smaller and compact planar sensing coils and sensitive low noise amplifiers. Furthermore, for proof-of-concept demonstration, we have verified the capability of detection of biomolecules tagged to magnetic nanoparticles through the detection of streptavidin–biotin interaction.

6.4.1 Parameter analysis

Effective hydrodynamic size

The measurement of AC susceptibility for individual monodisperse iron oxide MNPs in solution (100 μl; functionalized with carboxylic acid groups) having core diameters of 15, 25, 35 and 50 nm with a concentration of 5 mg ml^{-1}

(supplied by Ocean Nanotech, USA) under an external magnetic field of 0.5 mT is displayed in Figure 6.7. The result shows each frequency peaks in log scale are at 8836, 8544, 7865 and 2230 Hz with increasing effective hydrodynamic size of MNPs. Although the shifts of frequency peaks are discrepant from theoretical values, possibly due to the broad size distribution and anisotropic nature of the MNPs, results validate that the resonant frequency for the imaginary component of the complex magnetic susceptibility is inversely proportional to the effective hydrodynamic size of MNPs as predicted in equations (6.1) and (6.2). Also, we find that downsizing of MNPs causes a gentle slope of the curve for the real part of magnetic susceptibility in Figure 6.7(b). MNPs with a narrow size distribution and regular shape are desirable for Brownian relaxation detection, since these factors have been shown to contribute significantly to frequency peak shifts and peak sharpness even across small changes in effective hydrodynamic size [141].

Concentration

Experiments varying the concentration of MNPs in suspension gives us information about the sensitivity of the proposed compact AC susceptometer. We measured the complex magnetic susceptibility for varying concentrations of dextran-coated MNPs (10 nm core size: supplied by Liquids Research, UK) in 80 μl volume and 0.5 mT field excitation strength as shown in Figures 6.8 (a) and (b). Measurements of AC susceptibility for concentration dependence show that detection of frequency maxima in 10 μT fields is definitely workable to at least 1

mg ml^{-1} sensor concentrations with our present susceptometer, and can be easily improved further with optimal coil geometry and detector sensitivity.

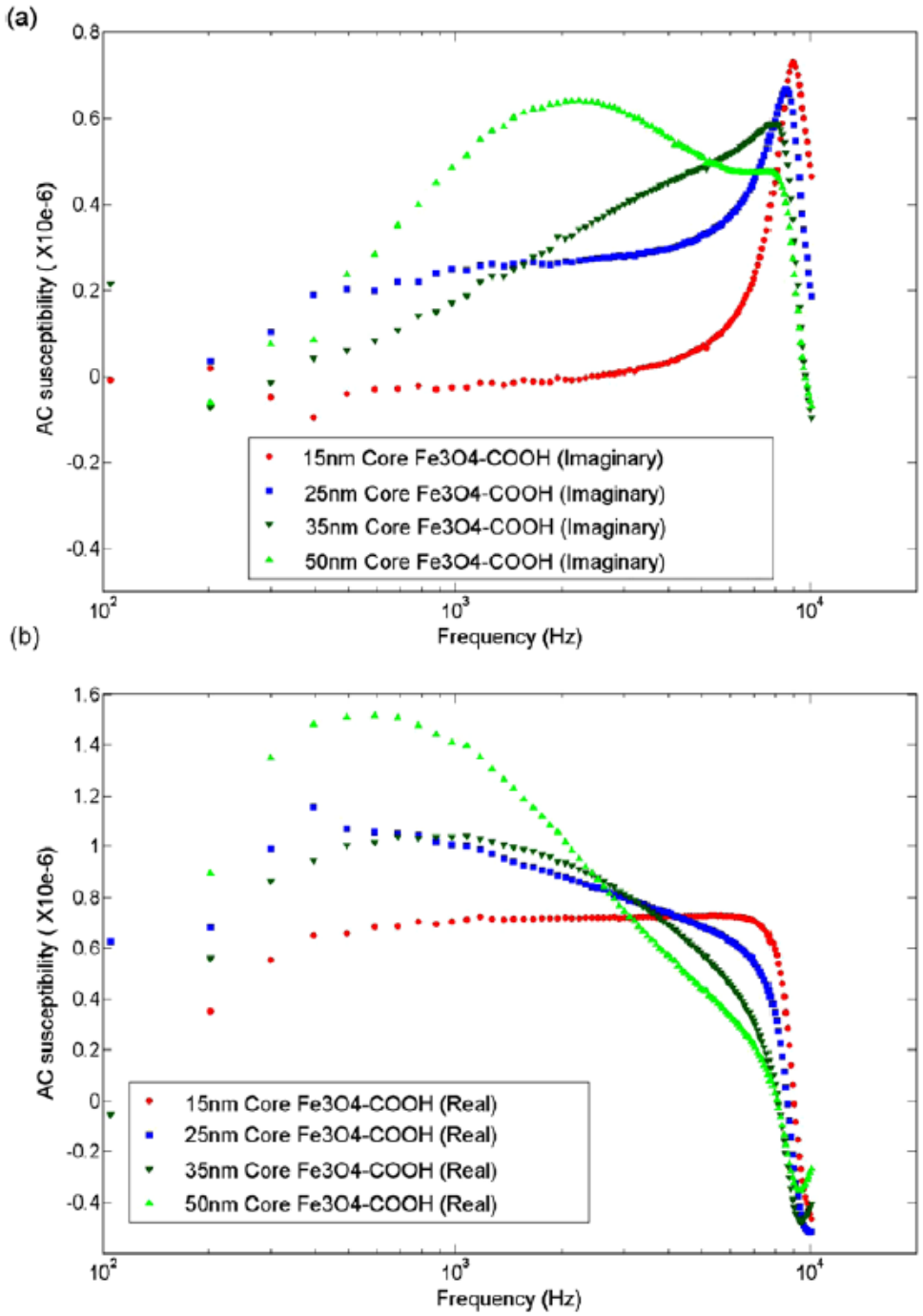

Figure 6.7 Measured complex AC magnetic susceptibility for iron oxide nanoparticles in water with carboxylic acid functional group (Fe_3O_4–COOH) having various core sizes; (a) real component and (b) imaginary component of complex magnetic susceptibility.

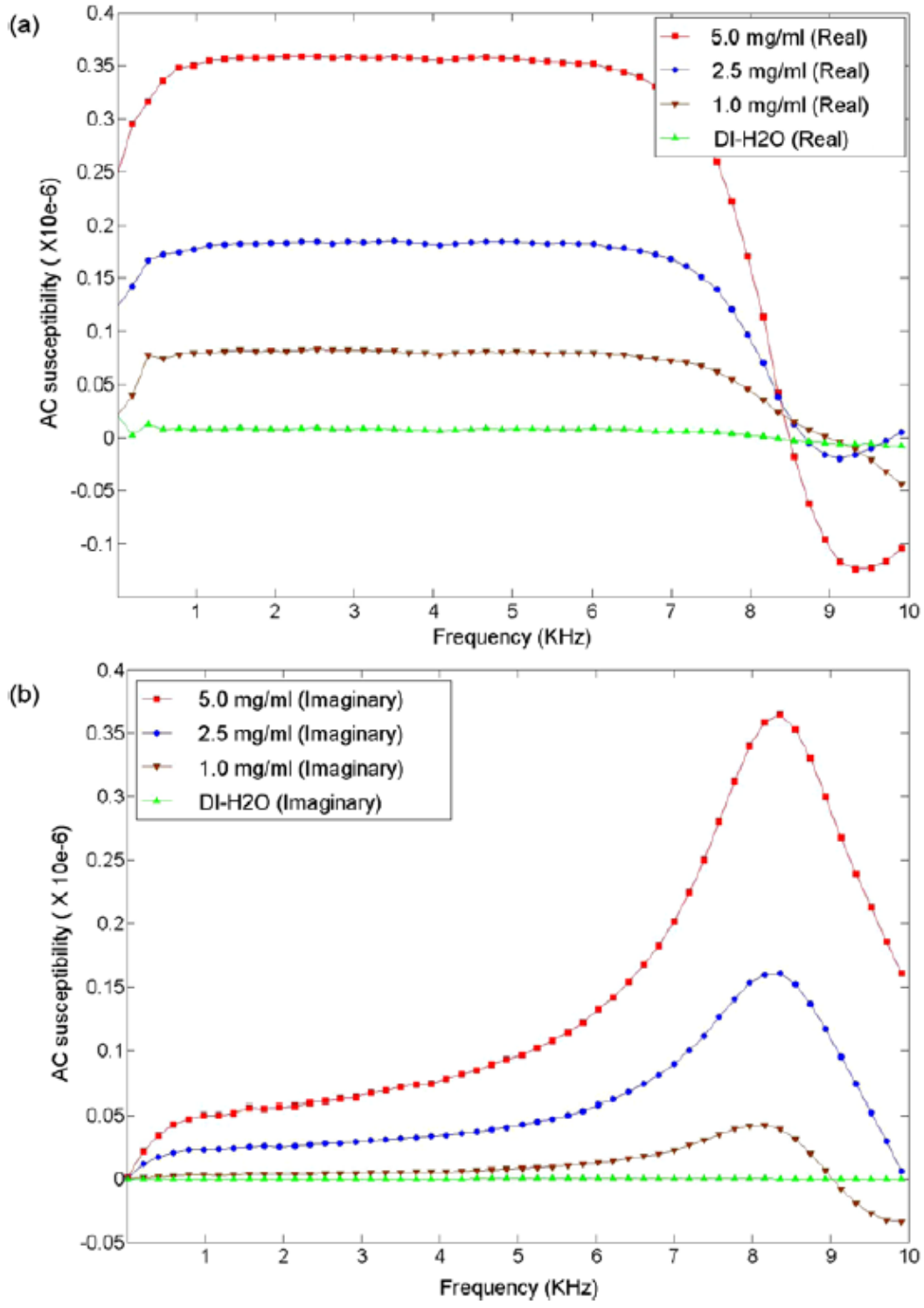

Figure 6.8. Measurement of (a) real component and (b) imaginary component of complex magnetic susceptibility for varying concentrations of dextran-coated MNPs (80 μl) with core size of 9 nm.

Applied magnetic field

We have observed the effect of applied magnetic field strength as shown Figure 6.9. Magnetite nanoparticles in H_2O with carboxylic acid functional group (Fe_3O_4–COOH) having 25 nm core sizes and 5 mg ml^{-1} concentration (supplied by Ocean Nanotech, USA) were used for this experiment. AC field strengths as low as 10 μT permit the repeatable identification of susceptibility peaks as 8544 Hz, suggesting that detection can be achieved with very small power requirements of the order of microwatts.

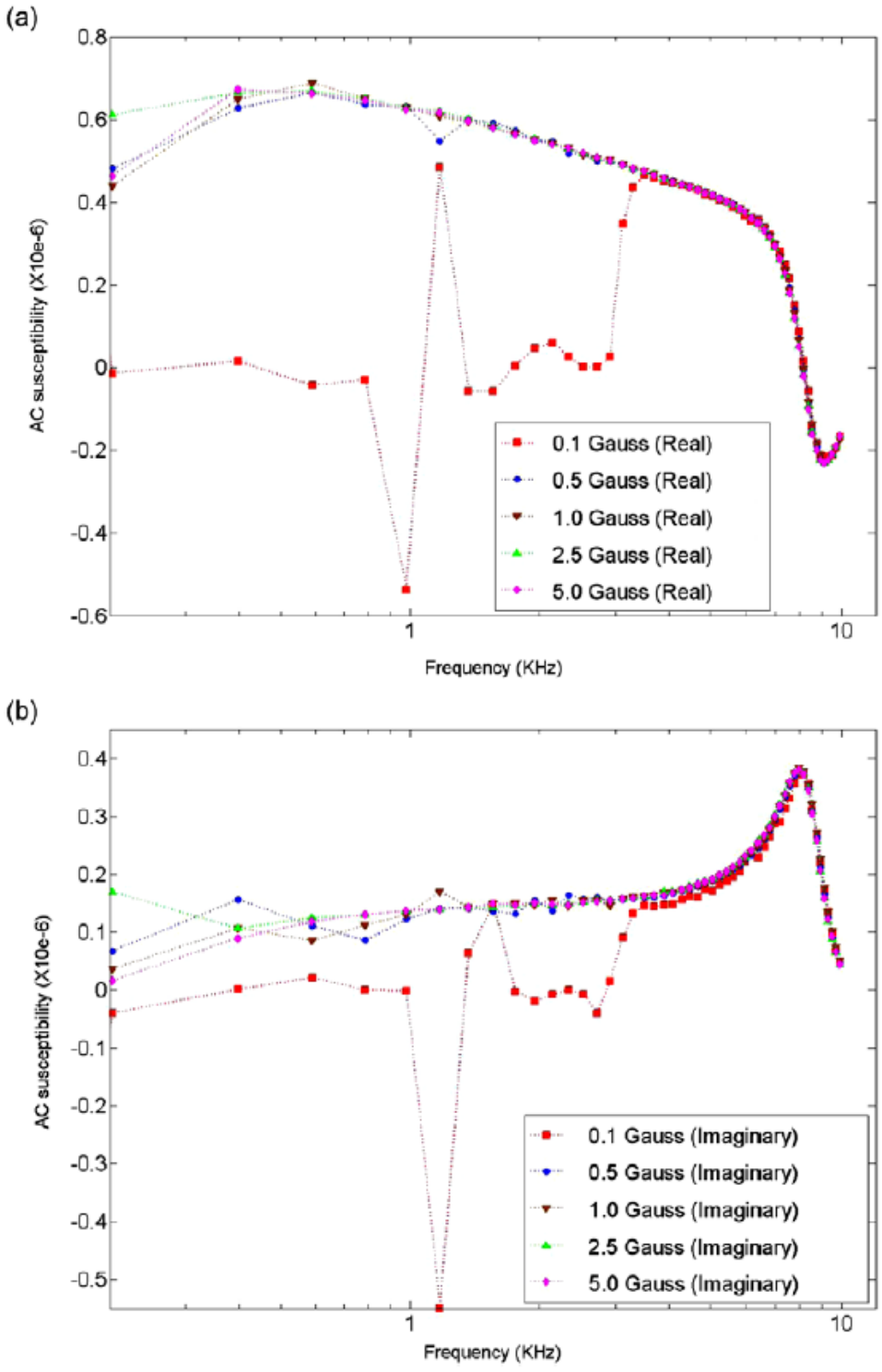

Figure 6.9 Measurement of the complex AC susceptibilities of 25 nm core MNPs in suspension under varying magnetic field applied by primary coil: (a) real component and (b) imaginary component.

6.4.2 Multiplexed detection scheme

The proposed sensing scheme based on measurement of change in the Brownian relaxation due to change in effective hydrodynamic size is very suitable for multiplexed detection of multiple biological targets tagged to MNPs. Since the imaginary component of the AC susceptibility of individual MNPs with different sizes has its own distinct frequency peak corresponding to the hydrodynamic radius of the MNPs, an AC susceptometer with remarkable sensitivity enables us to detect the multiple frequency peaks for a mixture of differently sized MNPs simultaneously. Moreover, if a selective bioconjugation such as the affinity of avidin–biotin can be applied to the mixture, which leads to an aggregation for only single MNPs, we will be able to measure the original Brownian relaxation time for non-aggregated MNPs.

To verify the potential of the proposed multiplexed detection scheme, we have measured AC susceptibility for a 1:1 mixture of iron oxide MNPs in solution (80 μl; functionalized with carboxylic acid group) with core diameters of 25 and 50 nm (5 mg ml^{-1}) (Ocean Nanotech, USA) as shown in Figure 6.10. The result shows that the imaginary component of AC susceptibility for the mixtures of two differently sized MNPs indicates the combination of frequency peaks corresponding to each MNP. If the hydrodynamic size difference between samples in the mixture is very slight, such as a few nanometers, higher AC susceptometer sensitivity as well as a precise size distribution of MNPs in solution will be required to detect adjacent frequency peaks.

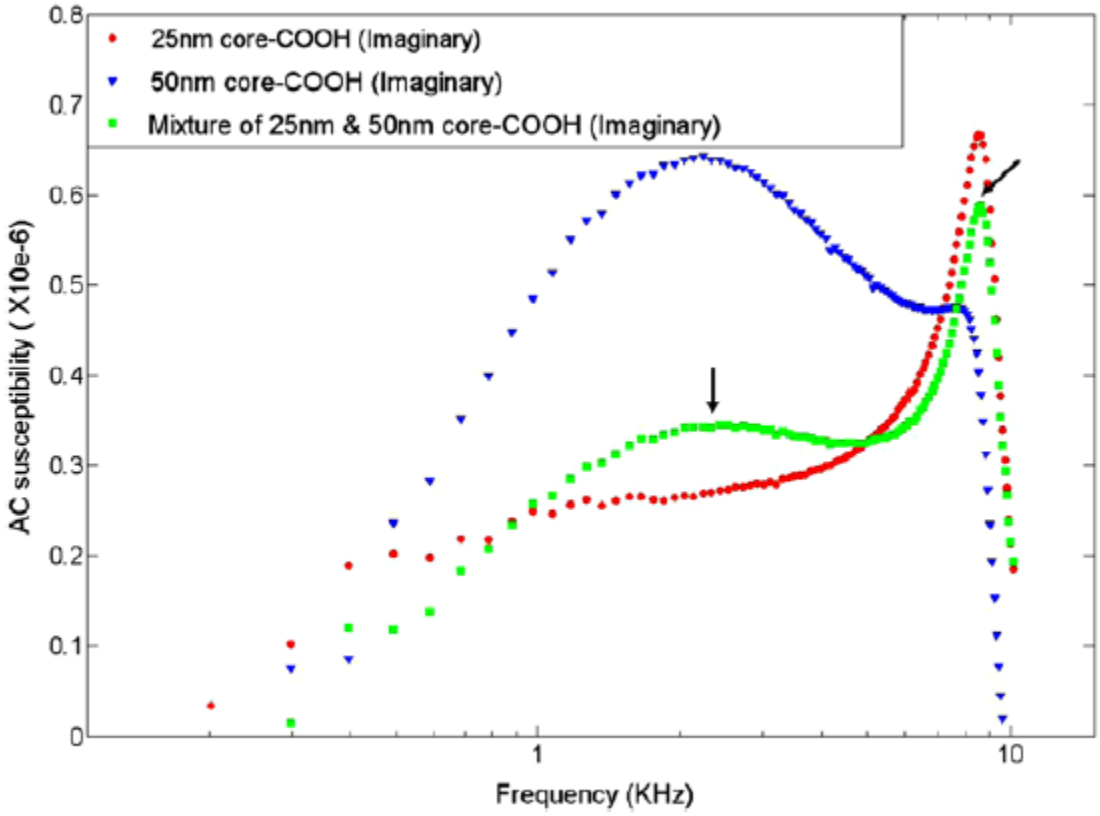

Figure 6.10 Multiplexed Brownian sensing for imaginary part of AC magnetic susceptibility for the mixture of two differently sized MNPs in H_2O (25 and 50 nm Fe_3O_4–COOH having 25 nm core sizes and 5 mg ml^{-1} concentration).

6.4.3 Detection of biomolecules tagged to magnetic nanoparticles using Brownian sensing

It is well established that the highly specific interaction of the protein avidin with biotin has exceptionally high stability [152]. This well-characterized biological binding event provides an ideal proof-of-concept demonstration to detect biomolecules tagged to MNPs by Brownian relaxation sensing [153, 154].

We used commercial biotinylated horseradish peroxidase (HRP) (supplied by Invitrogen, USA) and streptavidin-coated magnetite 25 nm (Fe_3O_4) nanoparticles (supplied by Ocean Nanotech, USA) in an 80 μl volume of 1 mg ml^{-1} concentrated aqueous solution. Transmission electron micrographs in Figures 6.9(a) and (b) show the original streptavidin-coated MNPs and cluster formation due to avidin–biotin binding interaction on addition of biotinylated HRP, respectively. The binding event causes variously sized clusters with increased hydrodynamic radius as shown Figure 6.11(b). This results in a shift of the frequency peak of the imaginary part of the AC susceptibility towards lower values. Figure 6.12 shows the expected shift in the frequency peak of the imaginary susceptibility to be the weighted sum of lower frequency peaks attributed to cluster formations of varying sizes. Figure 6.13 shows a 194 Hz downshift in the peak frequency of the imaginary susceptibility upon addition of biotinylated HRP to streptavidin-coated MNPs. In addition, measurements show that biotinylated HRP with high concentration (2 mg) leads to increased shift towards lower frequencies due to increased cluster formation resulting in more with larger hydrodynamic size. The inset shows the detail of each frequency peaks in log scale at 8836, 8642 and 8254 Hz with increasing concentration of biotinylated HRP. Although streptavidin possesses a high binding affinity for biotin, nonspecific binding of the HRP protein to streptavidin exists in this experiment, which also contributes to an increase in the hydrodynamic radius of individual particle to some extent [155, 156]. A previous study has reported the relative strength of non-specific and specific binding in the

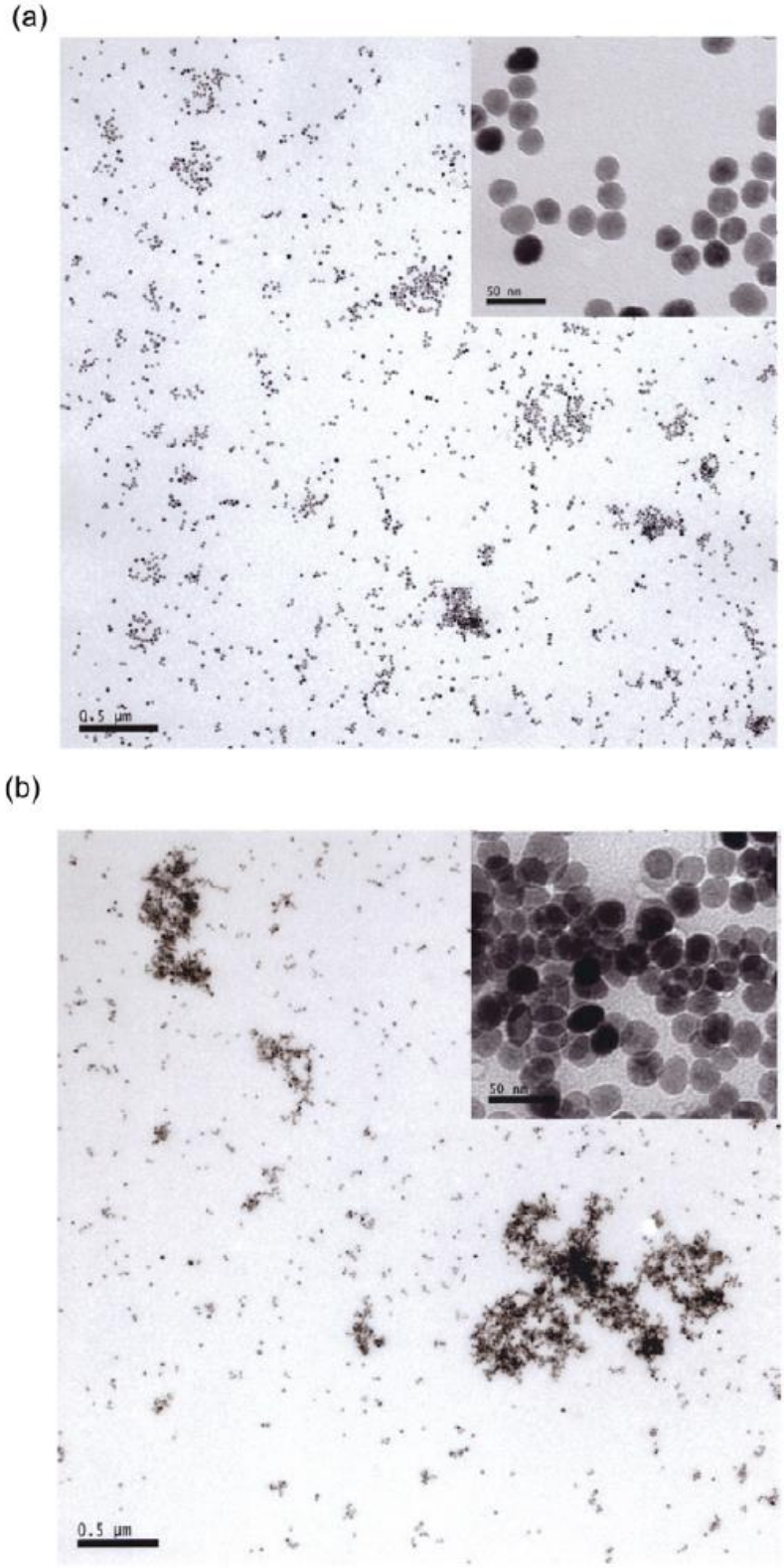

Figure 6.11 Transmission electron micrograph for avidin–biotin biological binding event (a) streptavidin-coated MNPs in solution and (b) streptavidin-coated MNPs binding to biotinylated horseradish peroxidase.

avidin–biotin detection system for various types of avidin including streptavidin [157]. The paper showed that the signal strength of specific binding, namely avidin–biotin binding, is much higher than that of non-specific binding, even though it is known that avidin can bind to some proteins non-specifically in the absence of a biotin tag. We had verified independently using a highly sensitive commercial magnetic susceptometer that, if the magnetic core is able to move 'freely' such as when there is a loose binding due to weak adsorption or other interaction of the biomolecule complex on the MNP, there will be no change in the peak frequency response of the imaginary susceptibility. Thus, the observed aggregation of nanoparticles can be attributed primarily to avidin–biotin affinity in our experiments, and not to any non-specific HRP–avidin binding. However, since it is obvious that nonspecific binding of HRP to streptavidin still exists and could contribute to the shift in frequency peaks, we conclude that a combination of specific and non-specific binding events affects the conjugation of streptavidin-coated MNPs and biotinylated HRP. To form the basis of biological sensing, we recognize two significant aspects in Figure 6.13, which are (1) frequency peak shift and (2) a change in the entire spectrum including a different shape and a magnitude change of the susceptibility at lower frequencies. The former, frequency peak change, would result from a combination of strong avidin–biotin binding and non-specific HRP–streptavidin binding and the latter, entire spectrum change, is mainly attributable to the high strength of avidin–biotin affinity to lead the aggregation and form large clusters of MNPs. Although it is

clear that specific binding for avidin and biotinylated HRP after the conjugation reaction happens, no remarkable peak at very low frequency implies that a considerable amount of both free streptavidin-coated MNPs and biotinylated HRP are still present in the solution. However, we are able to conjecture aggregation activity in the solution by observing the increase of imaginary susceptibility at very low frequencies at higher concentrations of biotinylated HRP.

In order to prove that an avidin–biotinylated HRP specific binding event has occurred in the previous experiment displayed in Figure 6.13, we have performed a control experiment with highly purified horseradish peroxidase (HRP) (supplied by Invitrogen, USA) and streptavidin-coated iron oxide 25 nm (Fe_3O_4) nanoparticles in an 80 μl volume of 1 mg ml^{-1} solution. The appearance of pure peroxidase is a reddish brown amorphous powder, lyophilized, and the molecular weight is approximately 40 kDa. Figure 6.14 shows there are no changes in the peak frequency of the imaginary susceptibility upon the addition of pure HRP with different concentrations to streptavidin-coated MNPs. The inset displays the detail of the same frequency peaks at 8836 Hz regardless of the increase in the concentration of pure HRP. We also observe the imaginary susceptibilities at low frequency are almost on the same level, which means there is no aggregation in the solution. Nevertheless, we should note that nonspecific binding between pure HRP protein and streptavidin coated MNPs still exists in the solution under hydrodynamic conditions and causes an insignificant small shift in the frequency spectrum.

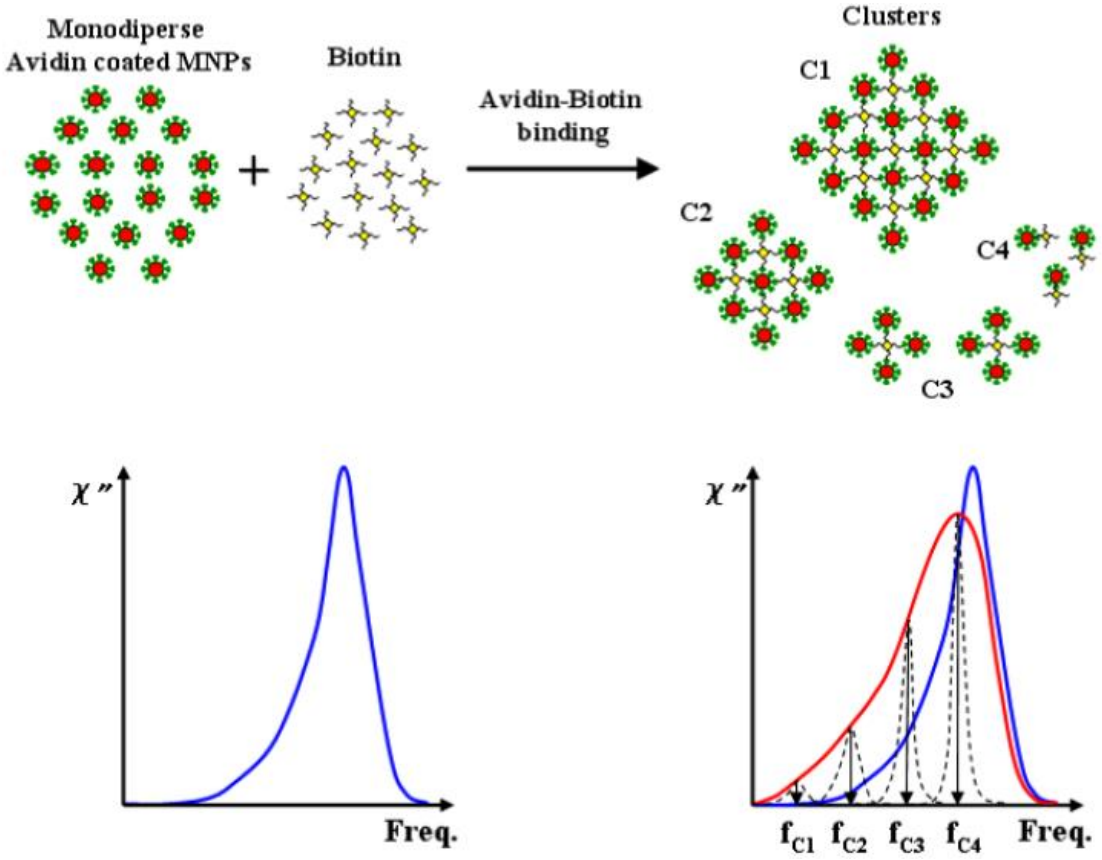

Figure 6.12 Schematic representation of imaginary part of AC magnetic susceptibility for magnetic nanoparticles upon avidin–biotin interaction.

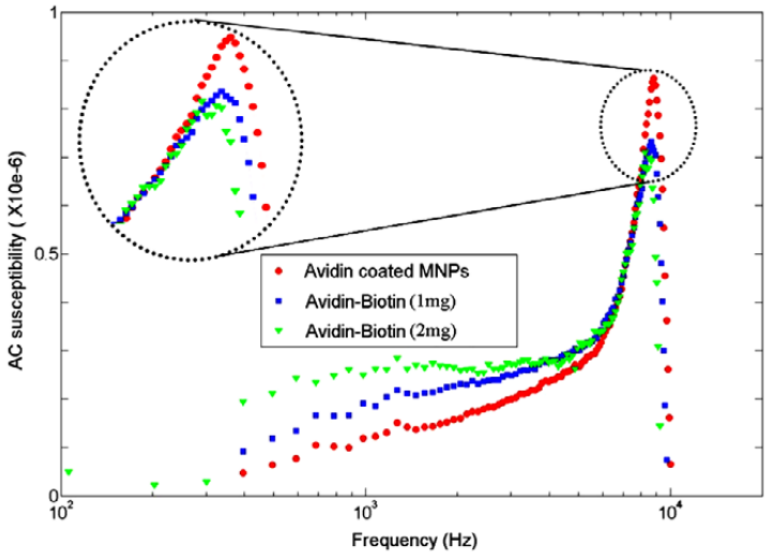

Figure 6.13 Imaginary part of the AC magnetic susceptibility of streptavidin-coated MNPs (red circles), after binding to biotinylated horseradish peroxidase in low concentration (blue squares, 1 mg) and after binding to biotinylated horseradish peroxidase in high concentration (green triangles, 2 mg).

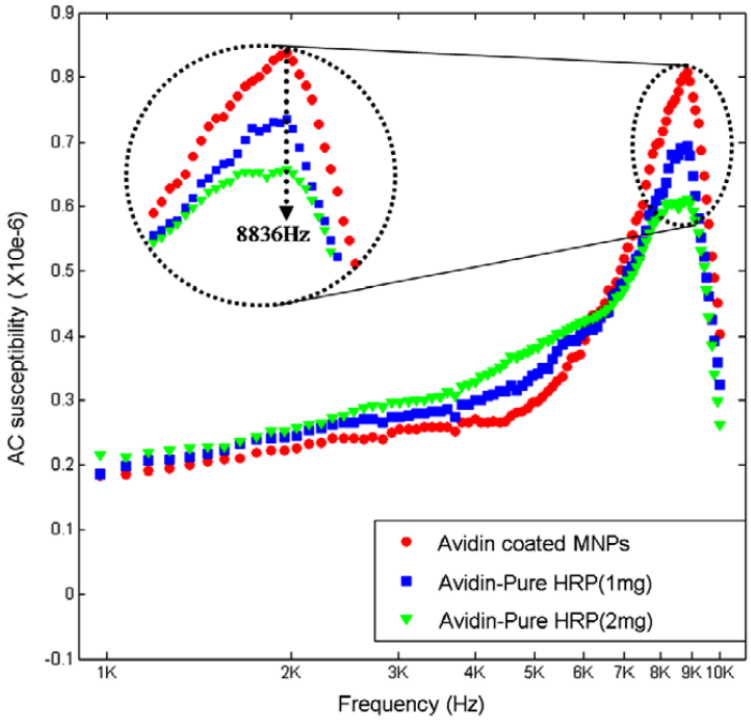

Figure 6.14 Imaginary part of the AC magnetic susceptibility of streptavidin-coated MNPs (red circles), after mixing with pure horseradish peroxidase in low concentration (blue squares, 1 mg) and after mixing with pure horseradish peroxidase in high concentration (green triangles, 2 mg).

6.5 Summary

In summary, a novel sensing paradigm based on the Brownian relaxation of magnetic nanoparticles in a liquid using a miniaturized AC susceptometer has been studied. Our compact AC susceptometer was used to experimentally conduct parameter analysis of complex AC magnetic susceptibility as a function of the effective hydrodynamic size, concentration, applied magnetic field and volume with MNPs in suspension. The measurements for iron oxide MNPs with different sizes have verified the sensing modality. We have also found that the compact AC susceptometer has a sensitivity of 1 mg ml^{-1} concentration under magnetic fields as low as 10 μT, and this metric can be readily improved with improved coil designs and smaller geometries. A novel multiplexed detection scheme for multiple biological targets tagged to functionalized MNPs using Brownian relaxation has been proposed and verified by experiments with mixtures of differently sized magnetic nanoparticles. Finally, we measured AC susceptibility of the binding of biotinylated HRP and streptavidin-coated MNPs to detect biomolecules tagged to MNPs based on size-dependent Brownian relaxation. For the proof against the avidin–biotin binding event, AC susceptibility measurement has been performed with pure HRP protein and streptavidin-coated MNPs in solution. The results have shown the feasibility of sensing for target biomolecules with affinity labeled MNPs using a compact, room temperature AC susceptometer. Since AC susceptometers are, nowadays, used for measuring magnetic samples

having a remarkable demagnetizing effects have to be measured in a large range of fields, future work will first focus on the development of programmable adjustment by detect the offset from balanced coils for sensitivity improvement and then a chip-level AC susceptometer with higher sensitivity for lab-on-chip applications.

Chapter 7

Conclusion

In this thesis, we have demonstrated how the continuous scaling of micro-fabrication technology can offer new capabilities in realization of Lab-on-a-Chip (LoC) platforms. More specifically, we showed how they offer the potential to perform spatial control and manipulation of biological targets such as cells, and utilizing embedded transducers to sense and process them. We showed how if such platforms when integrated transistors and readout circuitry offers the potential to offer truly miniaturized solution. Such Lab-on-a-Chip (LoC) platforms with ever growing miniaturization of other supporting functions such as microfluidics for sample delivery and extraction will meet the ever-growing need

of low-cost, compact analytical devices in healthcare and medicine. In this thesis we presented two platforms, one for biosensing using magnetic nanoparticles and other for manipulation of cells in CMOS process.

For electrical cell manipulation, we presented a novel dielectrophoretic Lab-on-Chip (LoC) platform for trapping, rotation and detection of cells and micro-organism in aqueous solution using standard CMOS technology. The proposed LoC platform showed the ability of single cell trapping, cell repositioning by simple on-off switching of applied signal into novel 3D electrode design. Moreover, impedance sensing based cell detection scheme using integrated readout circuit is presented. Live yeast cells suspended in PBS solution were used as model system for test and evaluation. Future efforts will target other specific cell types for clinical applications such as animal blood cell. Also, microarray design will be pursued on CMOS technology to support high throughput diagnostics for biomedical application.

For biosensing, a miniaturized magnetic susceptometer for multiplexed detection of biomolecules tagged to magnetic nanoparticles (MNPs) based on size-dependent Brownian relaxation was demonstrated. The AC magnetic susceptibility measurements of Brownian relaxation of MNPs verify the sensing modality that proves the resonant frequency of imaginary susceptibility is inversely proportional to effective hydrodynamic size of MNPs. The proposed

Brownian sensing scheme has the potential for multiplexed analysis of multiple biological binding events on functionalized MNPs. Numerical analysis of sensitivity for AC susceptometer with differential solenoid configuration was presented. We have verified that the ability of size based detection scheme through the measurements for iron oxide MNPs with different sizes. This compact AC susceptometer has a sensitivity of 1 mg/ml concentration under magnetic fields as low as 10 μT at room temperature. We also present a multiplexed detection scheme for multiple biological targets labeled to functionalized MNPs using Brownian relaxation. Using avidin-biotin affinity mechanism, we proved our device has the capability to detect AC susceptibility based on size dependent Brownian relaxation for the binding of biotinylated HRP and streptavidin-coated MNPs. The focus of future work will be on implementation of a chip-level AC susceptometer for lab-on-chip applications. The key of the future work will be how we make a high Q microcoil using microfabrication technology.

In summary, the present thesis demonstrated the feasibility of the electrical and magnetic techniques for biosensing and cell manipulation along with miniaturization in semiconductor process with several interesting possibilities for future investigations.

Appendix

AC Susceptibility calculations

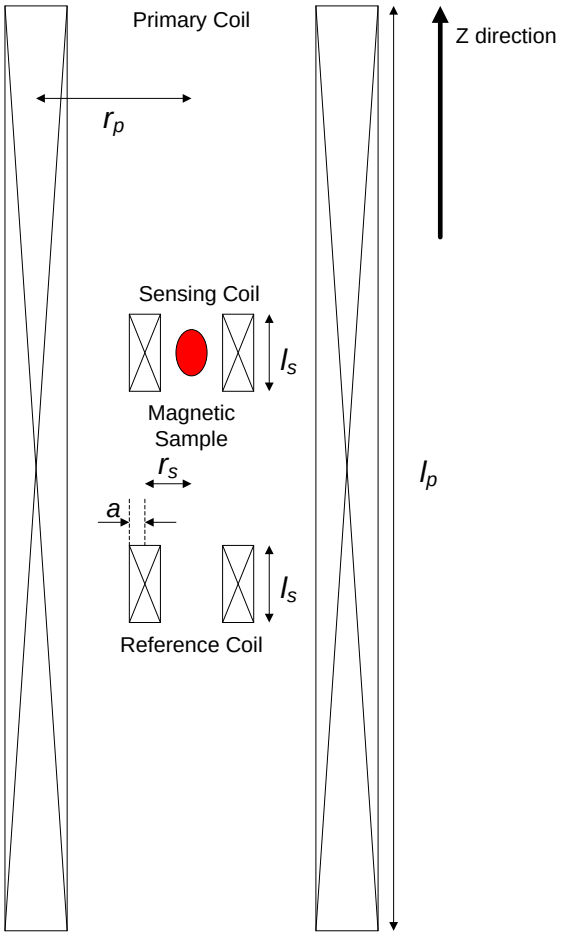

Figure A.1. Axial cross-sectional view of typical solenoid coils for AC susceptometer

Assumptions

1. Sensing coil and primary coil are identical and solenoid with air-core.

2. Two identical sensing coils are symmetrical in position inside a primary coil

3. There is no magnetization distortion.

4. Magnetic sample is located in the center of sensing coil.

Φ : Total Magnetic flux
B_p : Magnetic flux density generated by primary coil
B_s : Magnetic flux density at sensing coil with sample
B_e : Magnetic flux density at sensing coil without sample
B_r : Magnetic flux density at reference coil (= B_e)
V_r : Electromotive force at reference coil
V_s : Electromotive force at sensing coil with sample
V_e : Electromotive force at sensing coil without sample
N_s : Number of turns of sensing coil
N_r : Number of turns of reference coil (= N_s)
N_p : Number of turns of primary coil
l_s : Mean magnetic path length of sensing coil
l_p : Mean magnetic path length of primary coil
μ_s : Effective permeability of sensing coil with sample
μ_e : Effective permeability of sensing coil without sample
μ_0 : Relative permeability of air core
A : Cross sectional area in coil (m^2)

The voltage across the empty reference coil is

$$V_r = -N_r \cdot \frac{d\Phi_r}{dt} = -A_s \cdot N_s \cdot \frac{dB_e}{dt} \qquad \text{(A.1)}$$

The voltage induced into the sensing coil (part of secondary coil occupied by magnetic sample) due to the sample alone is

$$V_{s1} = -a_m \cdot (N_s \cdot \Delta l / l_s) \cdot \alpha \cdot \frac{dB_s}{dt} \qquad \text{(A.2)}$$

where α is the coupling coefficient between flux in the magnetic sample and sample coil. This value is the calibration constant determined by coil geometry. An estimate of this is $\alpha = (l_s/2)/\left[\sqrt{r_s^2 + (l_s/2)^2}\right]$ where l_s and r_s are the length and radius of a sensing coil, respectively. a_m is the magnetic sample cross-sectional area, Δl the sample length and $\Delta l / l_s$ the fraction of sensing coil length L occupied by the sample.

The voltage induced into the sensing-coil-less sample space is

$$V_{s2} = -(A_s - a_m \cdot \Delta l / l_s) \cdot N_s \cdot \alpha \cdot \frac{dB_e}{dt} \tag{A.3}$$

The output differential voltage required is

$$V_{out} = V_{s1} + V_{s2} - V_r \tag{A.4}$$

Then, the output differential voltage is

$$V_{out} = -a_m \cdot (N_s \cdot \Delta l / l_s) \cdot \alpha \cdot \left[\frac{dB_s}{dt} - \frac{dB_e}{dt}\right] \tag{A.5}$$

On the other hand, the external inductance of a circular loop of one turn is well approximated as [158]:

$$L_{Single,turn} \cong r \cdot \mu \cdot \left[\ln\left(\frac{8r}{a}\right) - 2\right] \tag{A.6}$$

where r is the radius of a circular loop, a is the radius of wire.

For a circular coil of N turns formed into a circular cross section, we may be able to modify the formula for a circular loop of one turn, equation (A.6), provided the cross section is small compared with the coil radius. Magnetic field must be computed on the basis of a current NI; in addition, to compute the total induced voltage about the coil, N integrations must be made about the loop. Equation (A.6) is thus modified by a factor N^2. The external inductance for N-turns solenoid coil is then:

$$L_{solenoid,n-turn} \cong N^2 \cdot r \cdot \mu \cdot \left[\ln\left(\frac{8r}{a}\right) - 2 \right] \tag{A.7}$$

For the other extreme, the inductance of a very long solenoid may be computed. If the solenoid is long enough, the magnetic on the inside is essentially constant, as for the infinite solenoid,

$$H_z = \frac{NI}{l} \tag{A.8}$$

where N is the total number of turns and l the length. The flux linkage for N turns is then $N\pi R^2 \mu H_z$, and the inductance is

$$L_{solenoid,long} = \frac{\pi\mu \cdot r^2 N^2}{l} \tag{A.9}$$

For coils of intermediate length-to-radius ratio, empirical or semi-empirical formulas frequently have to be used. The famous Nagaoka formula applies a correction factor *F* to the formula (d) for the long solenoid. A simple approximate form very close to this for *r/l* up to 2 or 3 is

$$L_{solenoid,\text{int}} = \frac{\pi\mu \cdot r^2 N^2}{l + 0.9r} \tag{A.10}$$

The main electrical parameters of interest are the transformer turns ratio *n* and the coefficient of magnetic coupling k_m. The current and voltage transformations between windings in an ideal transformer are related to the turn's ratio by the following equation:

$$n = \frac{V_s}{V_p} = \frac{I_p}{I_s} = \sqrt{\frac{L_s}{L_p}} \tag{A.11}$$

where V_p, V_s and I_p, I_s are the primary & secondary voltages and currents, and L_p, L_s are the self-inductances of the primary and secondary windings, respectively. The strength of the magnetic coupling between windings is indicated by the *k*-factor, as

$$k_m = \frac{M}{\sqrt{L_p L_s}} \tag{A.12}$$

where *M* is the mutual inductance between the primary and secondary windings. The self-inductance of a given winding is the inductance measured at the transformer terminals with all other windings open-circuited. If the magnetic coupling between windings is perfect (i.e., no leakage of the magnetic flux), k_m is

unity, while uncoupled coils have a *k*-factor of zero. A practical transformer will have a *k* -factor somewhere between these two extremes. Since the materials used in the fabrication of an IC chip have magnetic properties similar to air, there is poor confinement of the magnetic flux in a monolithic transformer and $M < \sqrt{L_p L_s}$. Thus, the *k*-factor is always substantially less than one for a monolithic transformer, however, coupling coefficients as high as 0.9 are realizable on-chip.

Letting the length of primary coil be long compared to radius of coil, we have an equation for self-inductance of primary coil by equation (A.9)

$$L_p = \frac{\pi \mu_0 \cdot r_p^{\,2} N_p^{\,2}}{l_p} \tag{A.13}$$

Similarly, an equation for self-inductance of sensing coil by equation (A.10) is

$$L_s = \frac{\pi \mu_0 \cdot r_s^{\,2} N_s^{\,2}}{l_s + 0.9 r_s} \tag{A.14}$$

Then, the transformer turns ratio is

$$n = \sqrt{\frac{L_s}{L_p}} = \left(\frac{r_s \cdot N_s}{r_p \cdot N_p} \right) \sqrt{\frac{l_p}{l_s + 0.9 r_s}} \tag{A.15}$$

The strength of the magnetic coupling between primary coil and sensing coil is

$$k_m = \frac{M}{\sqrt{L_p L_s}} = \frac{M\sqrt{l_p(l_s + 0.9r_s)}}{\pi\mu_0 \cdot r_s r_p N_s N_p} \tag{A.16}$$

The mutual inductance of two solenoid coils can be simply approximated as below,

$$M_{21} = N_1 N_2 P_{21} = N_1 N_2 \frac{\mu A}{l} \tag{A.17}$$

where P_{21} is the permeance of the space occupied by the flux.

Thus, we finally have the strength of the magnetic coupling between primary coil and sensing coil.

$$k_m = \frac{\mu_r A_s}{\pi \cdot r_s r_p}\sqrt{l_p\left(1+0.9\frac{r_s}{l_s}\right)} = \mu_r\left(\frac{r_s}{r_p}\right)\sqrt{l_p\left(1+0.9\frac{r_s}{l_s}\right)} \tag{A.18}$$

For $B = B_0 \sin\omega t = \frac{\mu N}{l} \cdot I_0 \cdot \sin\omega t$, an induced sinusoidal field at sensing coil and reference coil are

$$B_s = k_m \frac{\mu_s^{'} N_s}{l_s} \cdot I_s \cdot \sin\omega t = \mu_s\left(\frac{N_s}{l_s}\right)\left(\frac{r_s}{r_p}\right)\sqrt{l_p\left(1+0.9\frac{r_s}{l_s}\right)} \cdot I_s \cdot \sin\omega t \tag{A.19}$$

$$B_e = k_m \frac{\mu_e^{'} N_r}{l_r} \cdot I_r \cdot \sin\omega t = \mu_e\left(\frac{N_s}{l_s}\right)\left(\frac{r_s}{r_p}\right)\sqrt{l_p\left(1+0.9\frac{r_s}{l_s}\right)} \cdot I_s \cdot \sin\omega t \tag{A.20}$$

and sample volume $V_m = a_m \cdot \Delta l$,

$$V_{out} = -V_m \cdot \left(\frac{N_s}{l_s}\right)^2 \left(\frac{r_s}{r_p}\right) \sqrt{l_p\left(1+0.9\frac{r_s}{l_s}\right)} \cdot \alpha \cdot I_s \cdot \omega \cdot \left[\mu_s \cos(\omega t - \phi_s) - \mu_e \cos(\omega t - \phi_e)\right]$$

(A.21)

By equation $\alpha = (l_s/2)/\left[\sqrt{r_s^2 + (l_s/2)^2}\right]$,

$$V_{out} = -V_m \cdot \left(\frac{N_s}{l_s}\right)^2 \left(\frac{r_s}{r_p}\right) \sqrt{\frac{l_p\left(1+0.9\left(\frac{r_s}{l_s}\right)\right)}{1+4\left(\frac{r_s}{l_s}\right)^2}} \cdot I_s \cdot \omega \cdot \left[\mu_s \cos(\omega t - \phi_s) - \mu_e \cos(\omega t - \phi_e)\right]$$

(A.22)

By equation (A.11) and (A.15),

$$V_{out} = -V_m \cdot \left(\frac{N_p N_s}{l_s^{3/2}}\right) \frac{1+0.9\left(\frac{r_s}{l_s}\right)}{\sqrt{1+4\left(\frac{r_s}{l_s}\right)^2}} \cdot I_p \cdot \omega \cdot \left[\mu_s \cos(\omega t - \phi_s) - \mu_e \cos(\omega t - \phi_e)\right] \quad \text{(A.23)}$$

where $\mu_s, \mu_e, \phi_s, \phi_e$ are the effective permeability and phase shift of coil with sample and empty coil, respectively.

The sample and reference phase shifts can be taken into account by considering complex permeability. Letting $\mu_s e^{-j\phi_s} = \mu_s^{'} - j\mu_s^{''}$ and $\mu_e e^{-j\phi_e} = \mu_e^{'} - j\mu_e^{''}$,

$$\mu_s^{'} = \mu_s \cos\phi_s,\ \mu_s^{''} = \mu_s \sin\phi_s,\ \mu_e^{'} = \mu_e \cos\phi_e \text{ and } \mu_e^{''} = \mu_e \sin\phi_e \quad \text{(A.24)}$$

Expending the cosine terms gives

$$\mu_s \cos(\omega t - \phi_s) = \mu_s(\cos\omega t \cdot \cos\phi_s + \sin\omega t \cdot \sin\phi_s) = \mu_s^{'} \cos\omega t + \mu_s^{''} \sin\omega t \quad \text{(A.25)}$$

$$\mu_e \cos(\omega t - \phi_e) = \mu_e(\cos\omega t \cdot \cos\phi_e + \sin\omega t \cdot \sin\phi_e) = \mu_e^{'} \cos\omega t + \mu_e^{''} \sin\omega t \quad \text{(A.26)}$$

Hence, the output differential voltage becomes

$$V_{out} = V_{out}^{'} + jV_{out}^{''} \quad \text{(A.27)}$$

$$= -V_m \cdot \left(\frac{N_p N_s}{l_s^{3/2}} \right) \frac{1 + 0.9\left(\frac{r_s}{l_s}\right)}{\sqrt{1 + 4\left(\frac{r_s}{l_s}\right)^2}} \cdot I_p \cdot \omega \cdot \left[(\mu_s^{'} - \mu_e^{'}) \cos\omega t + (\mu_s^{''} - \mu_e^{''}) \sin\omega t \right]$$

(A.28)

$$= V_0 \cdot \left\{ (\mu_s^{'} - \mu_e^{'}) \cos\omega t + (\mu_s^{''} - \mu_e^{''}) \sin\omega t \right\} \quad \text{(A.29)}$$

where
$$V_0 = -V_m \cdot \left(\frac{N_p N_s}{l_s^{3/2}} \right) \frac{1 + 0.9\left(\frac{r_s}{l_s}\right)}{\sqrt{1 + 4\left(\frac{r_s}{l_s}\right)^2}} \cdot I_p \cdot \omega \ . \quad \text{(A.30)}$$

Then, in-phase and out of phase components of differential output voltage can be obtained as follows.

$$V_{out}^{'} = V_0 \cdot (\mu_s^{'} - \mu_e^{'}) \ , \ V_{out}^{''} = V_0 \cdot (\mu_s^{''} - \mu_e^{''}) \quad \text{(A.31)}$$

$$\frac{V_{out}^{'}}{V_0} = \mu_s^{'} - \mu_e^{'} \ , \ \frac{V_{out}^{''}}{V_0} = \mu_s^{''} - \mu_e^{''} \quad \text{(A.32)}$$

With no sample present, we take $\mu_e^{'} = 1$ and $\mu_e^{''} = 0$. Also, since $\mu_s = \mu_s^{'} + j\mu_s^{''}$ and $\mu_s = 1 + \chi = 1 + \chi^{'} + j\chi^{''}$ where χ is the measured magnetic susceptibility of the sample, we finally have;

$$\chi^{'} = \frac{V_{out}^{'}}{V_0} \quad , \quad \chi^{''} = \frac{V_{out}^{''}}{V_0} \tag{A.33}$$

Bibliography

[1] Liu F., Nordin AN, Li F, Voiculescu I. A lab-on-chip cell-based biosensor for label-free sensing of water toxicants, *Lab Chip*. 2014 Apr 7;14(7):1270-80.

[2] Jeong-Yeol Yoon, and Bumsang Kim, Lab-on-a-Chip Pathogen Sensors for Food Safety, *Sensors (Basel)*. 2012; 12(8): 10713–10741.

[3] Zhao Y, Chen D, Yue H, French JB, Rufo J, Benkovic SJ, Huang TJ., Lab-on-a-chip technologies for single-molecule studies, *Lab Chip*. 2013 Jun 21; 13(12):2183-98.

[4] Pavel Neužil, Stefan Giselbrecht, Kerstin Länge, Tony Jun Huang & Andreas Manz, Revisiting lab-on-a-chip technology for drug discovery, *Nature Reviews Drug Discovery* 11, 620-632 Aug. 2012.

[5] Foudeh AM1, Fatanat Didar T, Veres T, Tabrizian M, Microfluidic designs and techniques using lab-on-a-chip devices for pathogen detection for point-of-care diagnostics, *Lab Chip*. 2012 Sep 21;12(18):3249-66.

[6] Shah P, Zhu X, Chen C, Hu Y, Li CZ, Lab-on-chip device for single cell trapping and analysis, *Biomedical Microdevices*. 2014 Feb;16(1):35-41.

[7] Xuanhong Cheng, Yi-shao Liu, Daniel Irimia, Utkan Demirci, Liju Yang, Lee Zamir, William R. Rodrıguez, Mehmet Toner and Rashid Bashir, Cell detection and counting through cell lysate impedance spectroscopy in microfluidic devices, *Lab Chip*, 2007, 7, 746–755.

[8] Curtis D. Chin, Vincent Linder and Samuel K. Sia, Commercialization of microfluidic point-of-care diagnostic devices, *Lab Chip*, 2012,12, 2118-2134.

[9] H. Lee, D.Ham, and R.M.Westervelt, Eds., *CMOS Biotechnology*, 1st ed. Springer, Jun. 2007.

[10] A. Hierlemann, *Integrated Chemical Microsensor Systems in CMOS Technology*, 1st ed. 2005 ed. Springer, Dec. 2010.

[11] A. W. Martinez, S. T. Phillips and G. M. Whitesides, Three-dimensional microfluidic devices fabricated in layered paper and tape, *Proc. Natl. Acad. Sci. U. S. A.*, 2008, 105, 19606–19611.

[12] O. Geschke, H. Klank, and P. Telleman, Eds., *Microsystem Engineering of Lab-on-a-chip Devices*, 1st ed. Wiley-VCH, Mar. 2004.

[13] Vikram Mukundan and Beth L. Pruitt, MEMS Electrostatic Actuation in Conducting Biological Media, *J Microelectromechic Syst.* 2009 Apr 1; 18(2): 405–413.

[14] G. T. A. Kovacs, *Micromachined Transducers*. New York: McGraw-Hill, 1998.

[15] E. Ghafar-Zadeh, M. Sawan, and D. Therriault, A 0.18-um CMOS capacitive sensor Lab-on-Chip, *Sensors and Actuators A: Physical*, vol. 141, no. 2, pp. 454–462, Feb. 2008.

[16] F. Heer,W. Franks, A. Blau, S. Taschini, C. Ziegler, A. Hierlemann, andH. Baltes, CMOS microelectrode array for the monitoring of electrogenic cells, *Biosensors and Bioelectronics*, vol. 20, no. 2, pp. 358–366, Sep. 2004.

[17] K. Seidl, S. Herwik, T. Torfs, H. P. Neves, O. Paul, and P. Ruther, CMOS-Based High-Density silicon microprobe arrays for electronic depth control in intracortical neural recording, *Journal of Microelectromechanical Systems*, vol. 20, no. 6, pp. 1439–1448, Dec. 2011.

[18] B. Jang and A. Hassibi, Biosensor systems in standard CMOS processes: Fact or fiction?, *IEEE International Symposium on Industrial Electronics*, Jul. 2008, pp. 2045–2050.

[19] A. H. D. Graham, J. Robbins, C. R. Bowen, and J. Taylor, Commercialisation of CMOS integrated circuit technology in Multi-Electrode arrays for neuroscience and Cell-Based biosensors, *Sensors*, vol. 11, no. 5, pp. 4943–4971, May 2011.

[20] H. Baltes, O. Brand, G. K. Fedder, C.Hierold, J. G. Korvink, and O. Tabata, Eds., *Enabling Technologies for MEMS and Nanodevices*, 1st ed. Wiley-VCH, Sep. 2004.

[21] G. Fedder, R. Howe, T. K. Liu, and E. Quevy, Technologies for cofabricating MEMS and electronics, *Proceedings of the IEEE*, vol. 96, no. 2, pp. 306 –322, Feb. 2008.

[22] C. Guiducci, Y. Temiz, Y. Leblebici, E. Accastelli, A. Ferretti, G. Cappi, and E. Bianchi, Integrating bio-sensing functions on CMOS chips, *Asia Pacific Conference on Circuits and Systems (APCCAS)*, Dec. 2010, pp. 548 –551.

[23] J. Wang, *Analytical Electrochemistry*, 2nd ed. New York: Wiley, 2000.

[24] S. Parikh, G. Gulak, and P. Chow, A CMOS image sensor for DNA microarrays, *Proc. IEEE CICC*, Sep. 2007, pp. 821–824.

[25] J. D. Plummer, M. D. Deal, and P. B. Griffin, Silicon, *VLSI Technology: Fundamentals, Practice, and Modeling*. Englewood Cliffs, NJ: Prentice-Hall, 2000.

[26] H. Eltoukhy, K. Salama, and A. El Gamal, A 0.18 μm CMOS 106 lux bioluminescence detection system-on-chip, *IEEE J. Solid State Circuits*, vol. 41, no. 3, pp. 651–662, Mar. 2006.

[27] R. Lacowicz, *Principles of Fluorescence Spectroscopy*, 2nd Ed. New York: Plenum, 1999.

[28] B. Jang, P. Cao, A. Chevalier, A. Ellington, and A. Hassibi, A CMOS fluorescent-based biosensor microarray, *ISSCC Dig. Tech. Papers*, Feb. 2009, pp. 436–437.

[29] Stefan Geissbuehler, Azat Sharipov, Aurélien Godinat, Noelia L. Bocchio, Patrick A. Sandoz, Anja Huss, Nickels A. Jensen, Stefan Jakobs, Jörg Enderlein, F. Gisou van der Goot, Elena A. Dubikovskaya, Theo Lasser & Marcel Leutenegger, Live-cell multiplane three-dimensional super-resolution optical fluctuation imaging, *Nature Communications*, Article number: 5830, 2014.

[30] Hess, S, Girirajan, T. & Mason, M., Ultra-high resolution imaging by fluorescence photoactivation localization microscopy, *Biophys. J.* 91, 4258–4272, 2006

[31] Heilemann, M. et al., Subdiffraction-resolution fluorescence imaging with conventional fluorescent probes, *Angew. Chem*. Intl Ed. 47, 6172–6176, 2008

[32] A. P. M. Kentgens, J. Bart, P. J. M. van Bentum, A. Brinkmann, E. R. H. van Eck, J. G. E. Gardeniers, J. W. G. Janssen, P. Knijn, S. Vasa and M. H. W. Verkuijlen, High-resolution liquid- and solid-state nuclear magnetic resonance of nanoliter sample volumes using microcoil detectors, *J. Chem. Phys.* 128, 052202, 2008

[33] Huilin Shao, Changwook Min, David Issadore, Monty Liong, Tae-Jong Yoon, Ralph Weissleder, and Hakho Lee, Magnetic Nanoparticles and microNMR for Diagnostic Applications, *Theranostics*. 2012; 2(1): 55–65.

[34] Paul Liu, Karl Skucha, Mischa Megens, and Bernhard Boser, A CMOS Hall-Effect Sensor for the Characterization and Detection of Magnetic Nanoparticles for Biomedical Applications, *IEEE TRANSACTIONS ON MAGNETICS*, VOL. 47, NO. 10, OCTOBER 2011.

[35] M. Pertijis, K. Makinwa, and J. Huijsing, A CMOS temperature sensor with a 3σ inaccuracy of ±0.1 °C from -55 °C to 125 °C, *Proc. ISSCC Dig. Tech. Papers*, Feb. 2005, pp. 238.239.

[36] K. Ramanathan and B. Danielsson, Principles and applications of thermal biosensors, *Biosens. Bioelectron*., vol. 16, no. 6, pp. 417–423, Aug. 2001.

[37] George M. Whitesides, The origins and the future of microfluidics, *Nature* 442, 368-373, 27 July, 2006

[38] Loken M, Parks D and Herzenberg L, Two-color immunofluorescence using a fluorescence-activated cell sorter, *J. Histochem. Cytochem*. 25 899.907, 1977

[39] Parks D, Hardy R and Herzenberg L, Three color immunofluorescence analysis of mouse B lymphocyte subpopulations, *Cytometry* 159–68, 1984

[40] A. Ashkin, Acceleration and trapping of particles by radiation pressure, *Phys. Rev. Lett*. 24 156–9, 1970

[41] Ashkin A and Dziedzic J, Optical trapping and manipulation of viruses and bacteria, *Science* 235 1517, 1987

[42] Moldavan A, Photo-electric technique for the counting of microscopical cells, *Science* 80 188–9, 1934

[43] Crosland-Taylor P, A device for counting small particles suspended in a fluid through a tube, *Nature* 171 37–8, 1953

[44] Herzenberg L and Sweet R, Fluorescence-activated cell sorting, *Sci. Am*. 234 108–17, 1976

[45] Pohl H A, The motion and precipitation of suspensoids in divergent electric fields, *J. Appl. Phys*. 22 869–71, 1951

[46] Pethig R. and Markx G. H., Applications of dielectrophoresis in biotechnology, *Trends Biotechnol*. 15 426–32, 1997

[47] Gascoyne P. R. C. and Vykoukal J., Particle separation by dielectrophoresis, *Electrophoresis* 23 1973, 2002

[48] Morgan H., Hughes M. P. and Green N. G., Separation of submicron bioparticles by dielectrophoresis, *Biophys. J.* 77 516, 1999

[49] Hoyoung Yun, Kisoo Kim and Won Gu Lee, Cell manipulation in microfluidics, *Biofabrication* 5 022001, 2013

[50] Ashkin A., Dziedzic J. and Yamane T., Optical trapping and manipulation of single cells using infrared laser beams, *Nature* 330 769–71, 1987

[51] Kim S. B., Yoon S. Y., Sung H. J. and Kim S. S., Cross-type optical particle separation in a microchannel, *Anal. Chem*. 80 2628–30, 2008

[52] MacDonald M., Spalding G. and Dholakia K., Microfluidic sorting in an optical lattice, *Nature* 426 421–4, 2003

[53] Peterman E. J. G., Gittes F. and Schmidt C. F., Laser induced heating in optical traps, *Biophys. J.* 84 1308–16, 2003

[54] Neuman K. C. and Block S. M., Optical trapping, *Rev. Sci. Instrum*. 75 2787–809, 2004

[55] Chu S., Laser manipulation of atoms and particles, *Science* 253 861–6, 1991

[56] Maria Dienerowitz, Michael Mazilu, and Kishan Dholakia, Optical manipulation of nanoparticles: a review, *Journal of Nanophotonics*, Vol. 2, 021875 Sep. 2008.

[57] A. Ashkin, Forces of a single-beam gradient laser trap on a dielectric sphere in the ray optics regime. *Biophys*. J. **61**, 569, 1992

[58] A. Ashkin, J.M. Dziedzic, J.E. Bjorkholm, S. Chu, Observation of a single beam gradient force optical trap for dielectric particles. *Opt. Lett*. **11**, 288, 1986

[59] W.H. Wright, G.J. Sonek, M.W. Berns, Parametric study of the forces on microspheres held by optical tweezers. *Appl. Opt*. **33**, 1735, 1994

[60] Eric R. Dufresne and David G. Grier, Optical tweezer arrays and optical substrates created with diffractive optics, *Review of Scientific Instruments*, Vol.69, No. 5, May, 1998

[61] Melville D, Paul F and Roath S., Direct magnetic separation of red cells from whole blood, *Nature* **255** 706, 1975

[62] Laura L. Vatta, Ron D. Sanderson, and Klaus R. Koch, Magnetic nanoparticles: Properties and potential applications, *Pure Appl. Chem*, Vol.78, No.9, pp 1793-1801, 2006

[63] Abolfazl Akbarzadeh, Mohamad Samiei and Soodabeh Davaran, Magnetic nanoparticles: preparation, physical properties, and applications in biomedicine, *Nanoscale Research Letters*, Vol.7, No.1, 2012

[64] M.A.M. Gijs, Magnetic bead handling on-chip: new opportunities for analytical applications, *Microfluidics and Nanofluidics*, vol. 1, num. 1, p. 22-40, 2004

[65] N. Pamme, Magnetism and microfluidics, *Lab Chip*.; 6(1):24-38, Jan. 2006

[66] Nan Sun, Yong Liu, Hakho Lee, Ralph Weissleder, Donhee Ham, CMOS RF Biosensor Utilizing Nuclear Magnetic Resonance, *IEEE JOURNAL OF SOLID-STATE CIRCUITS*, Vol. 44, No. 5, May 2009

[67] Martin A. M. Gijs, Frédéric Lacharme and Ulrike Lehmann, Microfluidic applications of magnetic particles for biological analysis and catalysis, *Chem. Rev*., 2010, 110 (3), pp 1518–1563

[68] C. Gosse, V. Croquette, Magnetic tweezers: micromanipulation and force measurement at the molecular level, *Biophys. J*. 82 3314, 2002

[69] Miltenyi S, Muller W, Weichel W and Radbruch A, High gradient magnetic cell separation with MACS, *Cytometry*, 11 231–8, 1990

[70] Kang J H, Krause S, Tobin H, Mammoto A, Kanapathipillai M and Ingber D E, A combined micromagnetic-microfluidic device for rapid capture and culture of rare circulating tumor cells, *Lab Chip*, **12** 2175–81, 2012

[71] Hoshino K, Huang Y Y, Lane N, Huebschman M, Uhr J W, Frenkel E P and Zhang X, Microchip-based immunomagnetic detection of circulating tumor cells, *Lab Chip*, **11** 3449–57, 2011

[72] L. J. Yu, S. F. Y. Li, Electrophoretic Behavior Study of Bacteria of Pseudomonas aeruginosa, Edwardsiella tarda and Enteropathogenic Escherichia coli by Capillary Electrophoresis with UV and Fluorescence Detection, *Chromatographia*, Vol. 62, Issue 7-8, pp 401-407, October 2005

[73] Meera J. Desai and Daniel W. Armstrong, Separation, Identification, and Characterization of Microorganisms by Capillary Electrophoresis, *Microbiol Mol Biol Rev*. 67(1): 38–51, Mar 2003

[74] Jesper Østergaard, Lene Jorgensen, Anne Engelbrecht Thomsen, Susan Weng Larsen, Claus Larsen, Henrik Jensen, Drug–liposome distribution phenomena studied by capillary electrophoresis-frontal analysis, *Electrophoresis* Vol. 29, Issue 16, Jul 2008

[75] Vratislav Kostal, Bryan R. Fonslow, Edgar A. Arriaga, and Michael T. Bowser, Fast Determination of Mitochondria Electrophoretic Mobility Using Micro-Free Flow Electrophoresis, *Anal Chem*. 81(22): 9267–9273, Nov 2009

[76] Anna Wilk, Katarzyna Urbańska, David E. Woolley, Włodzimierz Korohoda, Cell separation with horizontal cell electrophoresis under near-isopycnic conditions on a density cushion, *Cellular & Molecular Biology Letters*, Vol. 13, Issue 3, pp 366-374, Sep 2008

[77] Adam Rosenthal and Joel Voldman, Dielectrophoretic Traps for Single-Particle Patterning, *Biophys J.* 88(3): 2193–2205, Mar 2005

[78] Sonnenberg A, Marciniak JY, Skowronski EA, Manouchehri S, Rassenti L, Ghia EM, Widhopf GF, Kipps TJ, Heller MJ., Dielectrophoretic isolation and detection of cancer-related circulating cell-free DNA biomarkers from blood and plasma, *Electrophoresis.* 35(12-13):1828-36, Jul 2014

[79] Mohammed Alshareef, Nicholas Metrakos, Eva Juarez Perez, Fadi Azer, Fang Yang, Xiaoming Yang and Guiren Wang, Separation of tumor cells with dielectrophoresis-based microfluidic chip, *Biomicrofluidics*, 011803, Jul. 2013

[80] Ting-Chen Shih, Kuang-Han Chu, and Cheng-Hsien Liu, A Programmable Biochip for the Applications of Trapping and Adaptive Multisorting Using Dielectrophoresis Array, *JOURNAL OF MICROELECTROMECHANICAL SYSTEMS,* vol. 16, no. 4, Aug 2007

[81] J. Nilsson, M. Evander, B. Hammarstrom, T. Laurell, Review of cell and particle trapping in microfluidic systems, *Analytica Chimica Acta* 649 141–157, 2009

[82] Kang Y, Li D, Kalams S A and Eid J E, DC-dielectrophoretic separation of biological cells by size, *Biomed. Microdevices* 10 243–9 2008

[83] Doh I and Cho Y H., A continuous cell separation chip using hydrodynamic dielectrophoresis (DEP) process, *Sensors Actuators* A 121 59–65 2005

[84] X.B. Wang, Y. Huang, J.P.H. Burt, G.H. Markx, R. Pethig, Selective dielectrophoretic confinement of bioparticles in potential energy wells, *J. Phys. D: Appl. Phys*, 26 1278, 1993

[85] T. B. Jones, Basic Theory of Dielectrophoresis and Electrorotation, *IEEE Engineering in Medicine and Biology Magazine*, Nov. 2003

[86] E.B. Cummings, A.K. Singh, Dielectrophoresis in microchips containing arrays of insulating posts: theoretical and experimental results, *Anal. Chem*. 75 4724, 2003

[87] J.A. Stratton, *Electromagnetic Theory*. New York: McGraw-Hill, 1941, section 3.9

[88] P. Lorrain and D.R. Corson, *Electromagnetic Fields and Waves,* 2nd ed. San Francisco, CA: W.H. Freeman, 1970, section 3.12.

[89] H.A. Pohl, *Dielectrophoresis*. Cambridge, UK: Cambridge University Press, 1978.

[90] T.B. Jones, *Electromechanics of Particles*. New York: Cambridge University Press, 1995.

[91] Hossein Nili and Nicolas G. Green, Higher-order dielectrophoresis of nonspherical particles, *PHYSICAL REVIEW* E 89, 063302, 2014

[92] A. Blake. *Handbook of Mechanics, Materials, and Structures.* Wiley, New York, 1985.

[93] Huang, Y.; Wang, X.-B.; Tame, J.; Pethig R, Electrokinetic behaviour of colloidal particles in travelling electric fields: Studies using yeast cells, *J. Phys. D*, *26*, 1528, 1993

[94] Gascoyne P R, Wang X B, Huang Y, Becker F F., Dielectrophoretic Separation of Cancer Cells from Blood, *IEEE Trans Ind Appl*. 33(3) 670-678, 1997

[95] L. Cui and H. Morgan, J., Design and fabrication of travelling wave dielectrophoresis structures, *Micromech. Microengineering*, 72, 2000

[96] R. Pethig, M. S. Talary and R. S. Lee, Enhancing traveling-wave dielectrophoresis with signal superposition, *IEEE Engineering in Medicine and Biology Magazine*, 22, 43, 2003

[97] P. Skladal, Advances in electrochemical immunosensors**,** *Electroanalysis*, 9, 737, 1997

[98] R. Karlsson, P. S. Katsamba, H. Nordin, E. Pol, D. G. Myszka, Analyzing a kinetic titration series using affinity biosensors, *Anal. Biochem*. 349, 136, 2006

[99] T. Schnelle, R. Hagedorn, G. Fuhr, S. Fiedler, and T. Muller, Three-dimensional electric field traps for manipulation of cells—calculation and experimental verification, *Biochim. Biophys. Acta*, 1157 127-40, 1993

[100] T. Schnelle, T. Muller and G. Fuhr., Trapping in AC octode field cages, *J. Electrostat.*, 50:17, 2000

[101] J. Suehiro, R. Hamada, D. Noutomi, M. Shutou, and M. Hara., Selective detection of viable bacteria using dielectrophoretic impedance measurement method, *J. Electrostat.*, 57:157, 2003

[102] M.P. Hughes and H. Morgan, Dielectrophoretic trapping of single sub-micrometre scale bioparticles, *J. Phys. D-Appl. Phys.*, 31:2205, 1998

[103] Erik M. Freer, Oleg Grachev, Xiangfeng Duan, Samuel Martin and David P. Stumbo, High-yield self-limiting single-nanowire assembly with dielectrophoresis, *Nature Nanotechnology*, vol.5, pp. 525-530, 2010

[104] Sarbajit Banerjee, Brian E. White, Limin Huang, Blake J. Rego, Stephen O'Brien, and Irving P. Herman, Precise positioning of single-walled carbon nanotubes by ac dielectrophoresis, *J. Vac. Sci. Technol. B* 24(6), Nov/Dec 2006

[105] Samuel MacNaughton, Srikanth Ammu, Sanjeev K. Manohar, Sameer Sonkusale, High-Throughput Heterogeneous Integration of Diverse Nanomaterials on a Single Chip for Sensing Applications, *PLOS ONE* October, 2014

[106] Chia-Ling Chen, Chih-Feng Yang, T. H. Kim, Vinay Agarwal, Sameer Sonkusale, Ahmed Busnaina, Michelle Chen and Mehmet R. Dokmeci, DNA-Decorated Carbon Nanotubes based Chemical Sensors Integrated onto Complementary Metal Oxide Semiconductor Circuitry, *IOP Nanotechnology*, vol. 21, pp. 095504, 2010

[107] Chia-Ling Chen, Chih-Feng Yang, Vinay Agarwal, Sameer Sonkusale, Michelle Chen, Mehmet Dokmeci, SS-DNA Decorated SWNT Gas Sensors Integrated on CMOS Circuitry, *IEEE Sensors Conference (SENSORS)* 2010

[108] Alexander D Wissner-Gross, Dielectrophoretic reconfiguration of nanowire interconnects, *Nanotechnology* 17 4986–4990, 2006

[109] S. Kabiri Ameri, P. K. Singh and S. Sonkusale, Utilization of graphene electrode in transparent microwell arrays for high throughput cell trapping and lysis, *Biosensors and Bioelectronics*, accepted, 2014.

[110] S. MacNaughton, S. Sonkusale, Single chip micro GC with integrated heterogeneous nanomaterial sensor array for multiparameter gas sensing, *Solid State Sensors, Actuators and Microsystems Workshop*, June 2014

[111] Saurin Patel, Daniel Showers, Pallavi Vedantam, Tzuen-Rong Tzeng, Shizhi Qian, and Xiangchun Xuan, Microfluidic separation of live and dead yeast cells using reservoir-based dielectrophoresis, *BIOMICROFLUIDICS* 6, 034102, 2012

[112] Pankhurst QA, Thanh NKT, Jones SK, Dobson J, Progress in application of magnetic nanoparticles in biomedicine, *J. Phys D* 42:224,001, 2009

[113] Roca AG, Costo R, Rebolledo AF, Veintemillas-Verdaguer S, Tartaj P, Gonzalez-Carreno T, Morales MP, Serna CJ, Progress in the preparation of magnetic nanoparticles for applications in biomedicine, *J Phys D* 42:224,002, 2009

[114] Berry CC, Progress in functionalization of magnetic nanoparticles for applications in biomedicine, *J Phys D* 42: 224,003, 2009

[115] Megens M, Prins M, Magnetic biochips: a new option for sensitive diagnostics, *J. Magn. Magn. Mater*. 293:702–708, 2005

[116] Rheinl¨ander T, K¨otitz R, Weitschies W and Semmler W, Magnetic fractionation of magnetic fluids, *J. Magn. Magn. Mater.* **219** 219–28, 2000

[117] P F de Châtel, I Nándori, J Hakl, S Mészáros and K Vad, Magnetic particle hyperthermia: Néel relaxation in magnetic nanoparticles under circularly polarized field, *J. Phys.: Condens. Matter* **21** 124202 2009

[118] Manuel Arruebo, Rodrigo Fernández-Pacheco, M. Ricardo Ibarra, Jesús Santamaría, Magnetic nanoparticles for drug delivery, *Nanotoday*, Vol. 2, no.3, pp. 22-32, Jun 2007

[119] K Ding, L Jing, C Liu, Y Hou, M Gao, Magnetically engineered Cd-free quantum dots as dual-modality probes for fluorescence/magnetic resonance imaging of tumors, *Biomaterials* Vol. 35, Issue 5, pp. 1608–1617, February 2014

[120] Peng XG, Schlamp MC, Kadavanich AV, Alivisatos AP, Epitaxial growth of highly luminescent CdSe/CdS core/shell nanocrystals with photostability and electronic accessibility, *J. Am. Chem. Soc.* 119(30):7019-7029, 1997

[121] Rockenberger J, Scher EC, Alivisatos AP, A new nonhydrolytic singleprecursor approach to surfactantcapped nanocrystals of transition metal oxides, *J. Am. Chem. Soc.* 121(49):11595-11596, 1999

[122] J. Connolly and T. G. St. Pierre, Proposed biosensors based on time-dependent properties of magnetic fluids, *J. Magn. Magn. Mater.* 225, 156, 2001

[123] John P Ridgway, Cardiovascular magnetic resonance physics for clinicians, *Journal of Cardiovascular Magnetic Resonance* 12:71, 2010

[124] Josephson, L.; Perez, J.M.; Weissleder, R., Magnetic nanosensors for the detection of oligonucleotide sequences, *Angew. Chem. Int. Ed.* 40, 3204–3208, 2001

[125] Lee. H., Sun, E., Ham, D., and Weissleder, R., Chip-NMR biosensor for detection and molecular analysis of cells, *Nat. Med.* 14, 869–874 2008

[126] Grossman H.L., Myers W.R., Vreeland V.J., Bruehl R., Alper M.D., Bertozzi, C.R., Clarke J., Detection of bacteria in suspension by using a superconducting quantum interference device, *Proc. Natl. Acad. Sci. USA 101*, 129–134, 2004

[127] S. H. Chung, A. Hoffmann, and S. D. Bader, C. Liu, B. Kay, L. Makowski, and L. Chen, Biological sensors based on Brownian relaxation of magnetic nanoparticles, *APPLIED PHYSICS LETTERS* vol. 85, no. 14 2004

[128] Shan X. Wang and Guanxiong Li, Advances in Giant Magnetoresistance Biosensors With Magnetic Nanoparticle Tags: Review and Outlook, *IEEE TRANSACTIONS ON MAGNETICS,* vol. 44, vo. 7, July 2008

[129] Osterfeld, S.J., Yu, H.; Gaster, R.S., Caramuta, S., Xu, L., Han, S.J., Hall, D.A., Wilson, R.J., Sun, S., White, R.L., Davis, R.W., Pourmand, N., Wang, S.X., Multiplex protein assays based on real-time magnetic nanotag sensing, *Proc. Natl. Acad. Sci.* USA 105, 20637–20640, 2008

[130] Graham, D.L.; Ferreira, H.A.; Freitas, P.P., Magnetoresistive-based biosensors and biochips, *Trends Biotechnol.* 22, 455–462, 2004

[131] Fu, A., Hu, W., Xu, L., Wilson, R.J., Yu, H., Osterfeld, S.J., Gambhir, S.S., Wang, S.X., Protein-functionalized synthetic antiferromagnetic nanoparticles for biomolecule detection and magnetic manipulation, *Angew. Chem. Int. Ed.* 48, 1620–1624, 2009

[132] Srinivasan, B., Li, Y., Jing, Y., Xu, Y., Yao, X., Xing, C., Wang, J.P., A detection system based on giant magnetoresistive sensors and high-moment magnetic nanoparticles demonstrates zeptomole sensitivity: potential for personalized medicine, *Angew. Chem. Int.* Ed. 48, 2764–2767, 2009

[133] De Palma R., Reekmans G., Liu C., Wirix-Speetjens R., Laureyn W., Nilsson O., Lagae L., Magnetic bead sensing platform for the detection of proteins, *Anal. Chem*. 79, 8669–8677, 2007

[134] Lu A. H., Salabas E. L. and Schuth F., Magnetic nanoparticles: synthesis, protection, functionalization, and application, *Angew. Chem. Int*. Ed. 46 1222–44, 2007

[135] Bader S. D., Colloquium: opportunities in nanomagnetism, *Rev. Mod. Phys.* 78 1–15, 2006

[136] Pankhurst Q. A., Connolly J, Jones S. K. and Dobson J., Applications of magnetic nanoparticle in biomedicine, *J. Phys. D: Appl. Phys.* 36 R167–81, 2003

[137] Lee H., Sun E., Ham D. and Weissleder R., Chip–NMR biosensor for detection and molecular analysis of cells, *Nat. Med*. 14 869–74 2008

[138] Baselt D. R., Lee G. U., Natesan M., Metzger S. W., Sheehan P. E. and Colton R. J. A biosensor based on magnetoresistance technology, *Biosens. Bioelectron*. 13 731–9, 1998

[139] Mihajlovic G., Xiong P., von Molnar S., Ohtani K., Ohno H., Field M. and Sullivan G. J., Detection of single magnetic bead for biological applications using an InAs quantum-well micro-Hall sensor, *Appl. Phys. Lett.* 87 112502, 2005

[140] Narasimhan L. R., Pate C. K. N. and Ketchen M. B., SQUID microsusceptometry in applied magnetic fields, *IEEE Trans. Appl. Supercond.* 9 3503–6, 1999

[141] Chung S.H., Hoffmann A., Guslienko K., Bader S. D., Liu C., Kay B., Makowski L. and Chen L., Biological sensing with magnetic nanoparticles using Brownian relaxation, *J. Appl. Phys*. 97 10R101, 2005

[142] Chung S. H., Hoffmann A., Bader S. D., Liu C., Kay B., Makowski L. and Chen L., Biological sensors based on Brownian relaxation of magnetic nanoparticles, *Appl. Phys. Lett*. 85 2971–3 2004

[143] Makiranta J. J. and Lekkala J. O., Modeling and simulation of magnetic nanoparticle sensor, *IEEE EMBC: 27th Int. Ann. Conf*. pp 1256–9, 2005

[144] Connolly J. and St Pierre T. G., Proposed biosensors based on time-dependent properties of magnetic fluids, *J. Magn. Mater.* 225 156–60, 2001

[145] Payet B., Siblini A., Blanc-Mignon M. F. and Noyel G., Comparison between a magneto-optical method and Fannin's technique for the measurement of Brown's relaxation frequency of ferrofluids, *IEEE Trans. Magn.* 35 2018–23, 1999

[146] Chung S.H., Grimsditch M., Hoffmann A., Bader S. D., Xie J., Peng S. and Sun S., Magneto-optic measurement of Brownian relaxation of magnetic nanoparticles, *J. Magn. Magn. Mater.* 320 91–5, 2008

[147] Heim E., Harling S., Pohlig K., Ludwig F., Menzel H. and Schilling M., Fluxgate magnetorelaxometry of superparamagnetic nanoparticles for hydrogel characterization, *J. Magn. Magn. Mater.* 311 150–4, 2007

[148] Ludwig F., Heim E., Mauselein S., Eberbeck D. and Schilling M., Magnetorelaxometry of magnetic nanoparticles with fluxgate magnetometers for the analysis of biological targets, *J. Magn. Magn. Mater.* 293 690–5, 2005

[149] Fannin P. C. and Scaife B. K. P., The measurement of the frequency dependent susceptibility of the magnetic colloids, *J. Magn. Magn. Mater.* 72 95–108, 1998

[150] Tim Harrah's Thesis, *Magnetically tagged tail fiber proteins for use as rodlike Brownian molecular sensors*, Chapter 5, 2009

[151] D-X Chen, High-field ac susceptometer using Helmholtz coils as a magnetizer, *Meas. Sci. Technol.* 15 1195–1202, 2004

[152] Laitinen O. H., Nordlund H. R., Hytonen V. P. and Kulomaa M. S., Brave new (strept) avidins in biotechnology, *Trends Biotechnol.* 25 269–77, 2007

[153] Astalan A. P., Ahrentorp F., Johansson C., Larsson K. and Krozer A., Biomolecular reactions studied using changes in Brownian rotation dynamics of magnetic particles, *Biosens. Bioelectron.* 19 945–51, 2004

[154] Eberbeck D., Astalan A. P., Petersson K., Wiekhorst F., Bergemann C., Johansson C., Steinhoff U., Richter H., Krozer A. and Trahms L., AC susceptometry and magnetorelaxometry for magnetic nanoparticle based biomolecule detection, *IFMBE Proc.* 22 2317–21, 2009

[155] Duhamel R. C. and Whitehead J. S., Prevention of nonspecific binding of avidin, *Methods Enzymol.* 184 201–7, 1990

[156] Kim S. H. *et al,* The enhanced reactivity of endogenous biotin-like molecules by antigen retrieval procedures and signal amplification with tyramine, *Histochem. J.* 34 97–103, 2002

[157] Masuoka J., Guthrie L. N. and Hazen K. C., Complications in cell–surface labelling by biotinylation of *Candida albicans* due to avidin conjugate binding to cell–wall proteins, *Microbiology* 148 1073–9, 2002

[158] Simon Ramo, John R. Whinnery and Theodore Van Duzer, *Fields and Waves in Communication Electronics*, 3rd edition, 1993

[159] Harivardhan Reddy L., Arias J. L., Nicolas J., Couvreur P., Magnetic Nanoparticles: Design and Characterization, Toxicity and Biocompatibility, Pharmaceutical and Biomedical Applications, *Chem. Rev.* 112, 5818, 2012

[160] Ye Zhang and Bing Xu, Multifunctional Magnetic Nanoparticles as Bionanomaterials, *American Institute of Biological Sciences,* 2011

[161] Tong Qing Yang, Masaya Abe, Kenji Horiguchi, Keiji Enpuku, Detection of magnetic nanoparticles with ac susceptibility measurement, *Physica C* 412–414 1496–1500, 2004